Optical Coherence Tomography for the Evaluation of Energy Seals and the
Subsequent Evaluation of the Thulium Laser as a Hemostatic Instrument

By

Andrew J. Marques

BEng in Biomedical Engineering, Ryerson University, 2016

A thesis presented to Ryerson University

in partial fulfillments of the requirements for the degree

of Master of Applied Science in the

program of

Biomedical Engineering

Ryerson University, Toronto, Ontario, Canada, 2020

Abstract

Optical Coherence Tomography for the Evaluation of Energy Seals and the Subsequent
Evaluation of the Thulium Laser as a Hemostatic Instrument

Master of Applied Science, 2020

Andrew J. Marques

Department of Biomedical Engineering

Ryerson University

Toronto, ON, Canada

This thesis presents the development of a system which integrates both an Optical Coherence
Tomography system and a high-powered Thulium fiber laser. The system was developed in order
to study the interaction between Thulium laser and tissue via Optical Coherence Tomography
feedback. This was done given the Thulium laser's theoretical potential to serve as a multipurpose
surgical instrument. The core work of the thesis is divided into two sections:

1. **The development of an energy seal evaluation methodology using Optical Coherence
   Tomography.** One-hundred and four avian embryonic vessels were subjected to Thulium
   laser irradiation at 1942 nm and subsequently imaged. Using both structural and Doppler
   feedback, several biomarkers were identified and used to classify irradiation outcomes as
   sealed or not sealed. The methodology developed here was compared to visual
   methodologies. It was found that the reported seal rate was dependent on the classification
   methodology ($p = 0.01$) where visual evaluation reported 18% more seals across the entire
   data set. The specificity of visual evaluation was dependent on the type of non-seal
   classification ($p < 0.0001$). Given that the developed methodology relied on the
   identification of biomarkers rather than user opinion, an objective evaluation methodology
   was achieved. Hemostatic systems evaluated visually should be re-evaluated.

2. **Evaluating the Thulium laser as a hemostatic instrument**. Average power, exposure
   time, and spot size were varied to maximize the seal rate. At sub 2 s exposure times the
   overall seal rate across all vessels was 29%. The highest seal rate achieved for a single
   condition was 60%. The rupture rate showed some correlation to average power.

Biological factors were found to have a significant effect on the seal rate where the mean vessel diameter for non-seal outcomes was greater than that for seal outcomes ($p < 0.001$). Tissue dehydration was a factor in this study. The average heat affected zone was 2.2 ± 1.1 mm, typical of a hydrolytic laser. This finding affirmed that hydrolytic lasers can induce seals despite the dimensions of the optical zone. As irradiance increased so did the heat affected zone, the opposite was true for exposure time. Using a dose until seal approach the seal rate was 95% across 18 vessels. The average therapeutic time was 9 ± 3 s for single vessel. Based on the overall lack of predictability observed in interactions between Thulium laser and vascular tissue, as well as the relatively poor seal rates, the Thulium laser was not recommended to be used in hemostatic applications.

Acknowledgements

Firstly, I would like to thank my supervisor Dr. Victor Yang in allowing me the opportunity to work with such incredible devices and furthermore for providing me with the experience of working in a state-of-the-art research environment surrounded by great minds. I have truly had an opportunity that most student biomedical engineers only dream of. Secondly, I would like to thank my co-supervisor Dr. Gu for all of his wisdom in working with optical systems.

Throughout my undergrad I struggled to excel for various reasons including poor work ethic and a lack of motivation. I would like to thank Dr. M. Kassam for sitting me down and berating me for the whole of 15 minutes turning my academic career around. That short time span in the third year of my undergrad may have been the most influential 15 minutes of my life to date.

Several outstanding professors truly shaped my career as an engineer I would like to give thanks for their various words of advice and moments of discussion. I would like to thank Dr. E. Harley for his incredible work ethic and dedication to teaching as well as our many squash games. I would like to thank Dr. K. Umapathy for challenging me in biomedical engineering and forcing me to innovate to find solutions to the problems at hand. I would like to thank Dr. S. Beheshti for motivating me to be at my very best and finally, I would like to thank Dr. M. Mehrvar for a plethora of sound advice and our weekly meetings on Tuesday night.

To my lab mates I wish to say thank you for the many laughs we shared. I would like to especially thank Joel Ramjist and Chaoliang Chen. Joel, thank you for your undying dedication to the lab, without you the ship would have sunken long ago. Chao, thank you for humoring my absolute lapse in knowledge in optical engineering over the years, this would not have been possible without you.

To C. Calabro, as you said I would move on to do great things with my life. Thanks for showing me what it truly means to be a leader and thank you for the abundance of lessons I learned in my time with you and most of all for teaching me to "let no one step on me".

And lastly, to my greatest of friends and my peer in biomedical engineering Robnier Reyes Perez, thank you for indulging me in my brief moments of insanity and accompanying me in my various escapades. Without you this thesis would surely have been a great deal more arduous.

To my parents, Avôs, and Avós

Table of Contents

List of Abbreviations and Symbols

<u>Abbreviations</u>

BPA: Burst Pressure Analysis

BPS: Beam Path Shift

CAM: Chorioallantoic Membrane

CC: Core-Cladding.

CMS: Cladding Mode Stripper

CR1: The favourable Cross Relaxation Process.

CR2: The unfavourable Cross Relaxation process.

D: Doppler classification.

DCM: Dichroic Mirror

DOCT: Doppler Optical Coherence Tomography

DS-Eval: Doppler Structural Evaluation

FBG: Fiber Bragg Grating.

FP: False positive

FN: False Negative

FWHM: Full width half maximum.

HAZ: Heat Affected Zone

Hb: Hemoglobin.

HRFBG: High reflectivity fiber Bragg grating.

IR: Infrared

KTP: Potassium Titanyl Phosphate.

LASER: Light Amplification by Stimulated Emission of Radiation.

LDH2: Line Scan Camera of the OCT system.

MIR: Mid-Infrared.

NA: Numerical Aperture.

Nd:YAG: Neodymium Yttrium Aluminum Garnet

NIR: Near Infrared

OCFBG: Output coupler fiber Bragg grating.

OCT: Optical Coherence Tomography.

OPL: Optical Path Length

OZ: Optical Zone.

RBC: Red Blood Cell, erythrocyte.

ROI: Region of Interest

SC: Supercontinuum

SC1: Laser Shutter Controller

SDOCT: Spectral Domain Optical Coherence Tomography

SH1: Laser Shutter

SMC: Smooth Muscle Cell.

SNR: Signal to Nosie Ratio

TC: Tropocollagen.

TN: True Negative

TP: True Positive

TREE: Trivalent Rare Earth Element.

UTS: Ultimate Tensile Strength.

V: Visual Classification.

<u>Symbols</u>

α: thermal diffusivity of tissue.

β: Coefficient for change in absorption coefficient with temperature.

δ: Optical penetration depth.

$\Delta\lambda$: Spectral bandwidth at full width half maximum.

$\Delta\phi$: Phase Shift.

$\Delta\varphi$: Minimum detectable phase shift.

θ: Angle of incidence.

θ_c: Confinement Angle.

λ: Wavelength.

μ_a: Absorption Coefficient (general).

μ_{Hb}: Absorption coefficient of Hemoglobin.

μ_{H2O}: Absorption coefficient of water.

μ_P: Absorption coefficient of protein.

μ_s: Scattering coefficient.

τ_d: Characteristic thermal diffusion time.

ρ: Density.

ϕ: Fluence.

ω_o: Beam waste radius, usually taken to be the radius of the beam at the tissue surface; spot size.

ω_c: Radius of the collimated beam at the focal lens.

ω: Angular frequency.

[X]: Concentration of X.

a: Fiber core radius.

c_P: Specific heat capacity.

d: Characteristic dimension of the optical zone.

E: Energy.

I: Irradiance.

I_o: Incident irradiance.

k: Function of evenly spaced K-Space query points for interpolation

k0: Wavenumber in terms of pixel number

L: Mirror to mirror round trip distance of a photon.

La: Function representing wavelength in terms of pixel number.

m: Mode number.

n_1: Core refractive index | refractive index of incident material.

n_2: Cladding refractive index | refractive index of secondary material.

n_x: Refractive index of a material specified by x.

NA: Numerical Aperture.

Q: Energy per unit volume.

R: Reflectance

t_E: Exposure time.

t_{lens}: Characteristic time for the formation of a thermal lens.

T: Temperature.

V: The V-number.

r: Radial position, distance form center of a circle in the plane of the circle.

R: Reflectance.

z: Depth.

List of Tables

List of Figures

Chapter 1: Introduction

Hemostasis is the process by which extraluminal blood flow is mitigated and ultimately stalled either through natural biological factors or through surgical intervention. Maintaining hemostasis is paramount across all surgical procedures and thus it has been a focus of medical technology development for some time. Electrosurgical instruments have dominated as tools for achieving hemostasis in surgical applications since William T. Bovie created the first electrosurgical instrument in the mid 1920's [1]. Bovie's electrosurgical cutting loop found its first application in 1926 where Harvey Cushing, the so-called father of modern surgery, used the device for intracranial surgeries where conventional hemostatic methods (such as suturing and clamping), could not be applied due to the delicate nature of brain tissue. With apprehension, Cushing continued to use the device finding its benefits indispensable as it made otherwise serious operations relatively simple because of its abilities in mitigating bleeding [2]. Today, electrosurgical instruments are used in every operating room and appear in a variety of forms. Their ability to dynamically modulate cutting and coagulative effects makes them a useful tool for practical surgical applications. A pure cutting mode can be achieved with higher current density waveforms whereas purely coagulative modes can be achieved with lower current density waveforms [3,4] allowing surgeons to modify surgical performance dynamically to meet the needs of a given procedure. Additionally, by varying current density temporally, both cutting and coagulation can be realized simultaneously [4]. Troubles associated with electrosurgery are largely due to the nature of electricity; electric current will seek the path of least resistance. Thus, usage of electrosurgical instruments involves risks of unintended burn and fire if the integrity of the circuit is compromised [5–7]. Examples of this are: high resistance collector electrodes, shorts (secondary paths to ground), and insulation failure. Burns tend to occur when collector electrodes of monopolar instruments offer high resistance due to bad placement (in the proximity of abundant adipose tissue or bony projections), or when electrode gels wear down [8]. In modernized electrosurgical systems, many of these problems have been overcome using isolated solid-state generators to avoid any ground faults, and also through the implementation of contact quality systems which continuously monitor the resistance of collector electrodes [8]. Despite this, the problem of insulation failure still exists, especially in laparoscopic hemostatic systems. In a 2009 study [6] both reusable and disposable laparoscopic electrosurgical instruments were tested for insulation failure. It was found that overall 15% of instruments suffered from insulation failure,

where reusable instruments had a greater failure rate than disposable. Of the reusable group, it was found that failure rates reached as high as 33% in hospitals where regular failure checks were not conducted and 19% in hospitals where failure checks were regularly conducted [9].

1.1 Potential Benefits of Laser-Based Hemostasis

Laser-based systems can offer the same benefits as electrosurgical instruments while theoretically eliminating many of the aforementioned risks. Since light is not readily conducted by tissue, the risk of unintended energy deposition to secondary biological structures is low. Laser-based systems also offer increased tunability given that a greater number of parameters contribute to the ultimate tissue effect (Figure 1.1). Conversely, this greater number of parameters also creates problems in achieving repeatable and predictable outcomes in laser tissue interactions, meaning that in many cases, large data sets are required to prove efficacy. Also, given the small scale on which these interactions take place, it can be challenging to accurately acquire data. As a result, laser-based systems remain a largely unexplored alternative to electrosurgical instruments as hemostatic devices. Most surgical laser systems in development today are intended for the purposes of ablation, less so coagulation. In fact, in many laser tissue interaction studies, coagulation as a by-product of ablation is considered a hinderance to the overall performance of the laser where ablation efficiency is inversely proportional to collateral thermal damage [10–13].
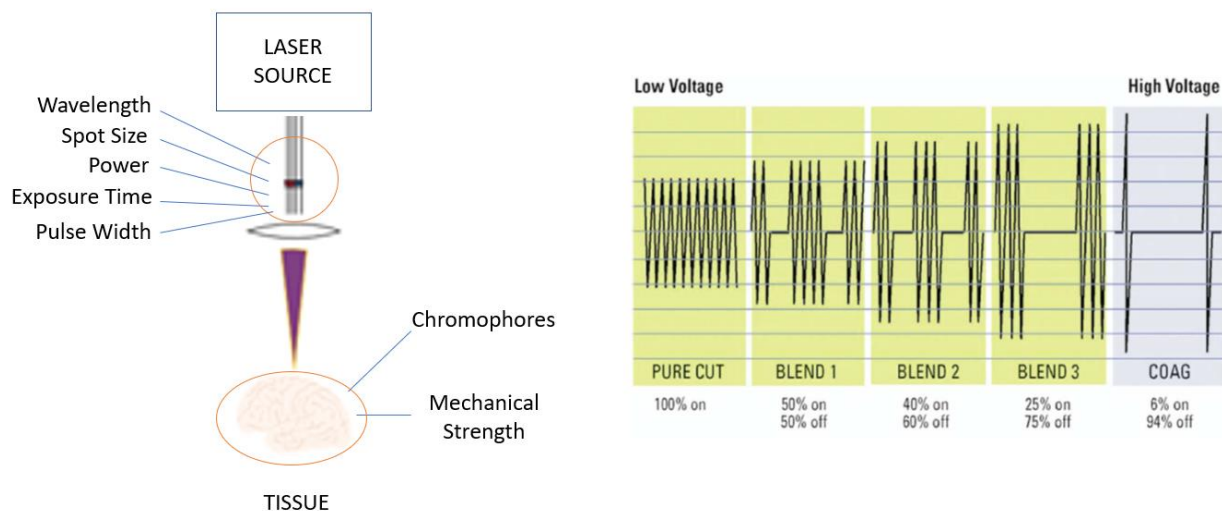
Figure 1.1 A comparison of laser parameters (left) and electrosurgical parameters (right). Several parameters determine the ultimate effect in interaction of laser and tissue while only voltage and current determine the effect in tissue with electrosurgical devices. Right image acquired from [4].

Commonly used hemostatic devices today, such as the advanced bipolar, tend to produce 4 mm (in diameter) or greater zone of collateral thermal damage which in many surgical scenarios is a desired effect: simultaneous ablation and coagulation [3,14–16]. The importance lies in regulating the degree of collateral thermal damage with respect to the nature of the procedure. For example, the collateral thermal damage produced by the advanced bipolar forceps is more significant in neurosurgical procedures than in dermatological procedures. In the case of hydrolytic lasers (lasers whose wavelengths coincide with a local absorption maxima of water) collateral thermal damage tends to be at most 3 mm, well below what is typically produced by advanced bipolar forceps [12,17–21].

LASER is a unique form of energy given that it remains coherent even after propagating through free space. This, in conjunction with a high degree of tuneability, gives the laser a distinct advantage over other energy based hemostatic systems; selective energy deposition can be achieved at a distance. Thus, lasers can eliminate all contact-induced negative effects associated with electricity-based hemostatic systems such as carbonization and tissue adhesion. Briefly, tissue adhesion occurs when contact based hemostasis results in the development of coagulum on an instruments' end effector. The result being that the coagulum adheres to the instrument potentially leading to injury when the instrument is retracted.

Tissue adherence, collateral thermal damage, and precision tunability may not initially seem to be major factors in many surgical cases. If iatrogenic injury is induced it is usually possible to re-seal any bleeding vessel and repair the injury. A decrease in collateral thermal damage from the 4 mm produced by advanced bipolar forceps to < 3mm produced by hydrolytic lasers may seem inconsequential. A slight increase in performance through improved targeting or modified energy deposition is certainly not a top priority for many surgeons. In a true surgical scenario, the objective is simply to maintain hemostasis; if 4 mm of collateral thermal damage is induced in the process that is usually a worthy tradeoff. However, when all of these factors are considered in the context of neurosurgery, they become extremely important given the precious nature of brain tissue. The greatest possible benefits that can be experienced by implementing lasers as hemostatic instruments would be in neurosurgery where every millimeter counts and reinjuring tissue can have major consequences.

1.2 Lasers in Neurosurgery

The use of lasers in surgery began only a couple years after the advent of the laser in 1959 where initial experiments by M. Zaret et al. demonstrated promising results in ophthalmological procedures [22]. The same cannot be said for use in neurosurgical procedures as the first application of ruby laser to murine cranium by Earle et al. [23] and Fine et al. [24] in 1965 resulted in instant death due to brain stem compression. Generally, use of the ruby laser in neurological procedures was not promising at the time given the poor absorption of the laser by non-pigmented tissues and uncontrollable biomechanical effects [25]. Following this, a prominent researcher by the name of Stellar first used the CO_2 laser (which has very high absorbance in tissue at 10.6 µm) in the resection of a glioblastoma. The bulky nature of the laser made it incredibly difficult to maneuver and the lack of a visible guidance laser made targeting tissue with the invisible CO_2 laser nearly impossible. Stellar personally advised prominent neurosurgeons against the use of lasers at that time, stalling progress in the field for some years [26]. The application of the laser in neurosurgery did not truly resume until 1980 where Beck, inspired by a modification made to the CO_2 laser four years earlier [27], conducted a study comparing the effects of the CO_2 laser and the Neodymium Yttrium Aluminum Garnet (Nd:YAG) laser [28]. Of importance here was the finding that the Nd:YAG laser allowed for nearly bloodless resection of highly vascularized intracranial tumours due to its high absorbance in hemoglobin causing it to be especially effective at ceasing diffuse blood flow from bony plates. This is the first known case where a laser was utilized as a hemostatic instrument in a contactless fashion. Until 1996 the CO_2, Nd:YAG, and, to a lesser extent, the Argon ion laser, were the focus of neurosurgical studies. The CO_2 laser was praised for its resective capabilities and high-power operation, although use of the laser remained labourious (as Stellar claimed) since the use of bulky free-space optic systems could not be avoided. Also, it was not suitable for highly vascularized tumours since it lacked hemostatic capability. The Nd:YAG laser was simpler to implement and could be used in endoscopic procedures as it was transmittable by quartz fiber. The deep penetration of the Nd:YAG light (1060 nm or 1320 nm) however causes excessive collateral tissue damage in procedures and therefore is not suitable for direct application to the cerebral cortex and other vital neurological structures. The Argon laser exhibited similar issues to the Nd:YAG laser with the addition that its output power was limited to sub 20 W operation making the resection of large tumours challenging. The development of new laser media over the past two decades has created variety of attainable

tissue effects thus increasing interest in laser neurosurgical devices. Despite this, and due to difficulties in establishing repeatable effects in laser-tissue interactions, the use of lasers in neurosurgery has yet to be widely adopted. The most common application being Laser Interstitial Thermal Therapy which involves the insertion of a deep brain probe to directly irradiate brain tumours in a minimally invasive fashion. Generally, the focus for the better part of the past few decades has been in employing lasers as ablative devices for the purposes of tissue resection. Further, there is generally a slow rate of adoption with surgical technologies amongst surgeons as often time familiarity supersedes the possibility of increased performance. This is why, in addition to historical tribulations, laser-based systems as hemostatic instruments have yet to be widely adopted by neurosurgeons.

1.3 Motivation and Objective

If a hydrolytic laser, such as the Thulium laser, can be tuned for the purposes of hemostasis, then both ablation and hemostasis can be achieved across most tissue types with a single instrument. This will eliminate the need for the use of photoangiolytic lasers and disposable instruments, potentially reducing the economic impact of surgical hemostasis. Further, this can be achieved in a contactless fashion eliminating tissue adherence entirely while greatly reducing the degree of collateral thermal damage. The Thulium fiber laser is compact, high-powered, tuneable, and lases at a strongly hydrolytic wavelength. Thus, many of the historical issues surrounding the use of lasers in neurosurgical applications can be overcome. This thesis presents the development of a Thulium laser system, and a study of its effects on vascular tissue, with the intention of achieving hemostasis through vessel sealing.

Given the general shift in surgical paradigm towards less invasive approaches, the use of lasers in surgery is increasing [29], and therefore it is important that the hemostatic potential of these laser systems can be evaluated reliably. As of the writing of this thesis, there does not exist an objective, standardized, widely adopted methodology for the evaluation of laser-induced energy seals in small vessels. The most commonly used method being visual examination, which is highly subjective (see Chapter 4). As a result, this work will present a new application of Optical Coherence Tomography (OCT) where it is used for the purposes of energy seal evaluation. The intention being to create an objective evaluation methodology that can be used to gauge the hemostatic potential of laser energy sealing systems.

This work begins with an in-depth background of fiber lasers, vascular tissue optical properties and ultrastructure, laser-tissue interaction, and OCT for structural and Doppler data acquisition (Chapter 2). In Chapter 3, a comprehensive system description is outlined detailing each component and its contribution to overall system functionality. Chapter 4 describes the development of an objective methodology for the evaluation of energy seals using Optical Coherence Tomography. In Chapter 5, the methodology developed in Chapter 4 is then used to evaluate the hemostatic potential of the Thulium laser.

Chapter 2: Background

Contactless vessel sealing by laser irradiation is an optical-thermal-mechanical process that involves a multitude of factors relating to the production and delivery of laser energy, as well as the thermomechanical behaviour of vascular tissue. Coherent light is produced by a laser cavity and allowed to irradiate tissue at which point it is the molecular constituents of the tissue that behave as chromophores which primarily govern the conversion of optical energy into thermal energy. The distribution of thermal energy in tissue directly determines the localized stresses developed, while the tissue's response to these stresses is dependent on its ultrastructural components. Therefore, a background of laser operation (specifically fiber laser operation) and the optical properties of vascular tissue is warranted. The ultrastructure of blood vessels in relation to vessel biomechanics will also be reviewed. Following this, a general discussion of the mechanisms behind laser-tissue interaction encompassing both the properties of laser irradiation and the properties of tissue will be afforded. All of this is required such that a general understanding of the processes resulting in the energy sealing of vessels can be developed. Finally, a practical description of OCT will also be presented given that it will be used for the evaluation of vessel seals in this work.

2.1 The Thulium Fiber Laser and General Fiber Laser Operation

The concept of the fiber laser was first proposed in 1961 by Snitzer where laser activity was demonstrated in Barium crown glass doped with Neodymium [30,31]. At the time, however, advancement in fiber laser technology was limited due to a lack of quality pumping sources and inefficient methods of optical fiber production. True development in fiber laser technology did not begin until the early 1980's where diode laser technology became widely available providing broad access to quality pumping devices. This, along with advances in fiber production and coupling techniques, allowed researchers to develop several types of fiber lasers with varying characteristics and a wide degree of applications in multiple technological sectors. The fiber laser is especially promising for surgical applications given its potentially small footprint and the relative ease with which it can be incorporated into catheter-based and laparoscopic instruments. The following sections will discuss the working principles of fiber lasers with special attention paid to the Thulium (Tm^{3+}) fiber laser.

2.1.1 Laser Glass Energetics

Laser activity within fibers is generated by trivalent rare earth elements (TREE's) which are embedded into a glass host medium during chemical vapor deposition manufacturing, a process called doping. TREE's doped into a glass medium form so-called optical centers. Both the properties of the TREE's and the composition of the glass host medium contribute to the lasing effects generated by the fiber. Light is ultimately produced by the relaxation of excited optical centers. Including Neodymium (Nd^{3+}), other common TREE's used for glass doping are Er^{3+}, Yb^{3+}, and Tm^{3+}. TREE's are ideal for the production of light because they feature a high degree of phononic shielding, meaning that energy losses in relaxation processes will have a greater tendency to produce light than to be absorbed into the host matrix via phonon production (vibratory dissipation). The wavelength of laser light produced is determined by energetic transitions specific to each TREE. Favourable transitions can be promoted by controlling the composition of the glass host as well as by using specific wavelengths of light to excite the optical centers. For example, EK-2236 silicate (60% Bi_2O_3, 30% CdO, 10% SiO_2, and 1% Nd_2O_3 by weight) has 20% greater absorption of the 808 nm wavelength than K-824 silicate (56.79% Ta_2O_5, 17.26% SiO_2, 15.07% BaO, 9.6% MgO, and 1.27% Nd_2O_3 by weight) allowing for greater efficiency in the production of the ~1050 nm output laser light in Nd^{3+} fiber lasers [32]. Excitation light sources, known as pumps or seed lasers, are typically selected to take advantage of high absorption peaks associated with TREE's as well as based on quality and availability. As an example, the characteristics of Nd^{3+} embedded in phosphate glass (by far the most common combination for fiber laser production in literature) are provided in Figure 2.1. Nd^{3+} doped phosphate glass is used here for pedagogical purposes. Referring to Figure 2.1 it can be seen that Nd^{3+} doped phosphate glass features strong absorption at 880 nm, 808 nm, 740 nm, and 580 nm. An interesting observation is that increased levels of doping result in increased absorption, a phenomenon common across all fiber lasers. However, increased absorption levels achieved via doping does not always result in greater emission of the desired light due to quenching. Briefly, quenching is the process where atoms at favourable excited states lose energy through undesirable processes such as multi-phonon emission and energy transfer between laser active ions. It is caused mostly by the clustering of laser active ions due to over-doping. Quenching becomes a serious issue in Nd^{3+} phosphate glasses when doping exceeds 5% thus, for efficient emission, doping levels are limited to 3%. Absorption in the 808 nm band results in the stimulated emission of 1500 nm, 1330 nm, 1050 nm, and 900 nm

8

light with the most likely emission being 1050 nm as can be seen in the emission spectrum of Figure 2.1. Stimulated emission is a key process for the production of LASER (Light Amplification by Stimulated Emission of Radiation) as it allows for the production of *coherent* photons. When radiative relaxation from an excited state does not occur spontaneously, but rather is triggered by an incoming photon with equivalent energy to the band gap between excited and lower states, stimulated emission occurs where the newly emitted photon is of the same energy and in phase with the trigger photon and thus is considered to be coherent. The importance of coherence is elaborated further in the next section.
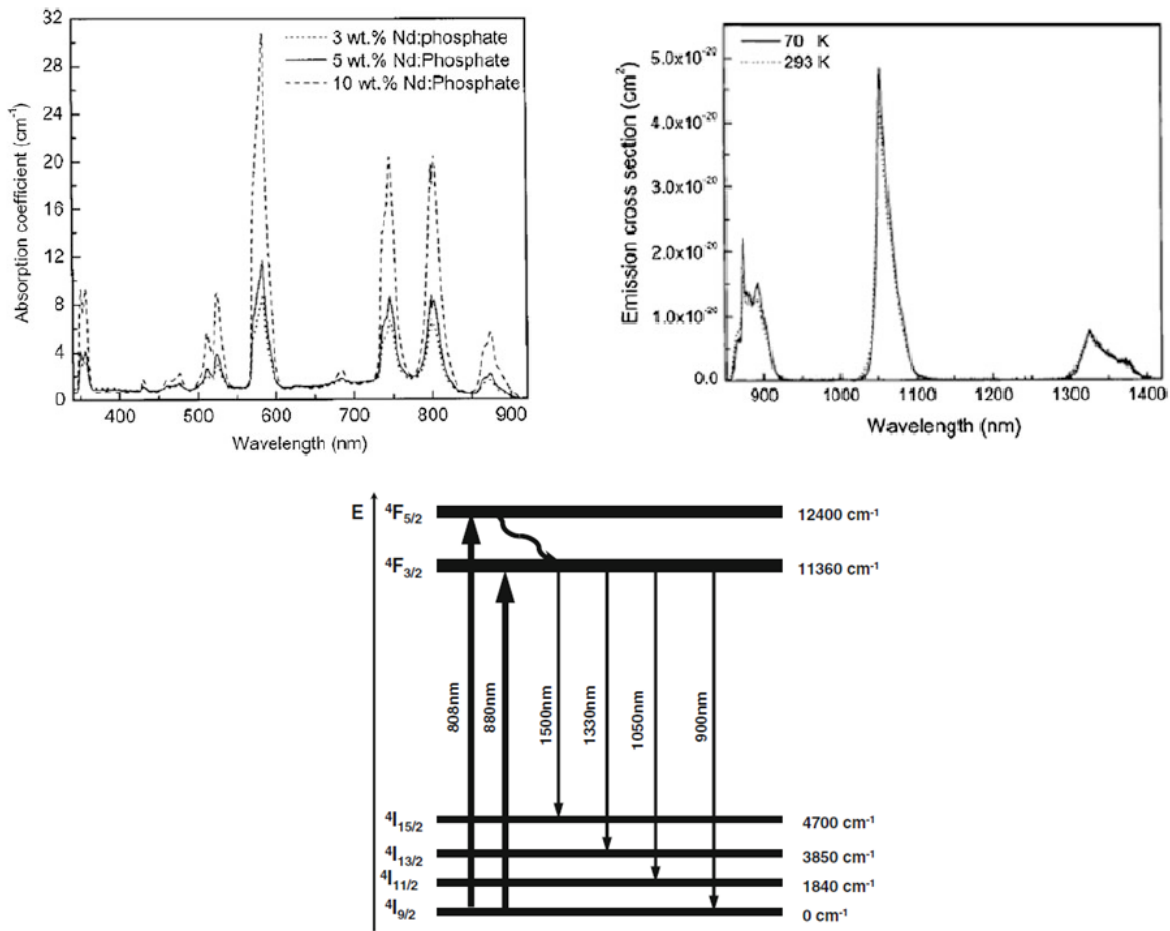
Figure 2.1 Characteristics of Nd^{3+} and Nd^{3+} doped phosphate glass. Top left: Absorption spectrum of Nd^{3+} doped phosphate glass at 3, 5, and 10% by weight doping levels [33]. Top right: emission cross section of the same Nd^{3+} doped phosphate glass at 3% doping by weight [33]. Below: Nd^{3+} energy level diagram including all important transitions associated with laser activity. Upwards arrows represent absorption, downwards arrows represent radiative emission (photon production), curvy arrows represent non-radiative emission (phonon production). Horizontal bars represent energy levels denoted in the following form $^{z}X_{y}$, where X is the electron shell level, z is the shell's multiplicity and y is the angular momentum [34].

While stimulated emission is crucial for the production of coherent photons, for efficient and continuous production of laser light, population inversion must be achieved. Population inversion occurs when more than 50% of optical centers are in a desirable excited state than in a lower neighbouring state. This typically requires that sufficient pump energy reaches the doped laser core, encouraging enough optical centers to become excited. Referring again to Figure 2.1, the emission of 1050 nm light is accomplished by pumping using either 808 nm or 880 nm light. Pumping via 808 nm light (which is more common given the availability of diode lasers with bandwidths 805-810 nm) results in a rapid phononic transition from the $^4F_{5/2}$ state down to the relatively long-lived $^4F_{3/2}$ state from which radiative emission is achieved by further relaxation down to the $^4I_{11/2}$ state. The ground state is then reached again by another rapid phononic transition (not depicted in figure 2.1). Therefore, in this 4-level laser scheme, population inversion is realized so long as there are more atoms in the $^4F_{3/2}$ state than the $^4I_{11/2}$ state. The former state is more long-lived than the latter, where, the former decays through radiative transmission with lifetimes ranging from nanoseconds to milliseconds, and the latter decays through non-radiative transmission with lifetimes from sub-nanoseconds to picoseconds. Thus, achieving population inversion in 4-level schemes is quite robust. This is in comparison to 3-level laser schemes where radiative emission results in direct relaxation to the ground-state. Since the ground-state is always populated, achieving population inversion in 3-level schemes is more problematic since it requires that more than half of the optical centers in a laser medium are excited. Thus, for the efficient production of laser light, 4-level schemes are most often employed.

Thulium ions embedded in silica-based fibers offer a relatively broad emission range from 1950-2200 nm. This spectral band coincides with the first over-tone of water resulting in high absorption in tissue. Thus, emission from the Tm^{3+} laser is considered to be "eye-safe" in the sense that any incident irradiation on the eye would be absorbed at the surface and would not make it down to critical structures in the retina. High absorption in tissue also means that this wavelength has many potential applications in the medical field given that reactions in tissue can be induced with less energy in comparison to other fiber lasers [35,36]. The Tm^{3+} ion has electron configuration $[Xe]4F^{13}6S^2$ and thus offers great phononic shielding since the filled 6S orbital discourages non-radiative electron transitions in the 4F shell [37]. Tm^{3+} is also much smaller than other TREE's due to lanthanide contraction, a characteristic specific to lanthanide metals where increasing atomic numbers result in smaller ions. The small size of the Tm^{3+} ion makes it much

more susceptible to clustering and subsequently quenching [37]. Despite this, the Thulium fiber laser is the most efficient fiber laser both quantumly and with respect to launched pump power (slope efficiency). This is due to cross-relaxation which occurs when the relaxation of one Tm^{3+} ion to an intermediate energy level immediately results in the excitation of another Tm^{3+} ion to that intermediate energy level.   When the ion pair relaxes, two photons are produced simultaneously resulting in a quantum efficiency of 200% as a single pump photon results in the production of two laser photons. Figure 2.2 gives the energy level diagram depicting the cross-relaxation process and pertinent energy levels. Cross-relaxation occurs within a quasi-3-level energetic scheme.
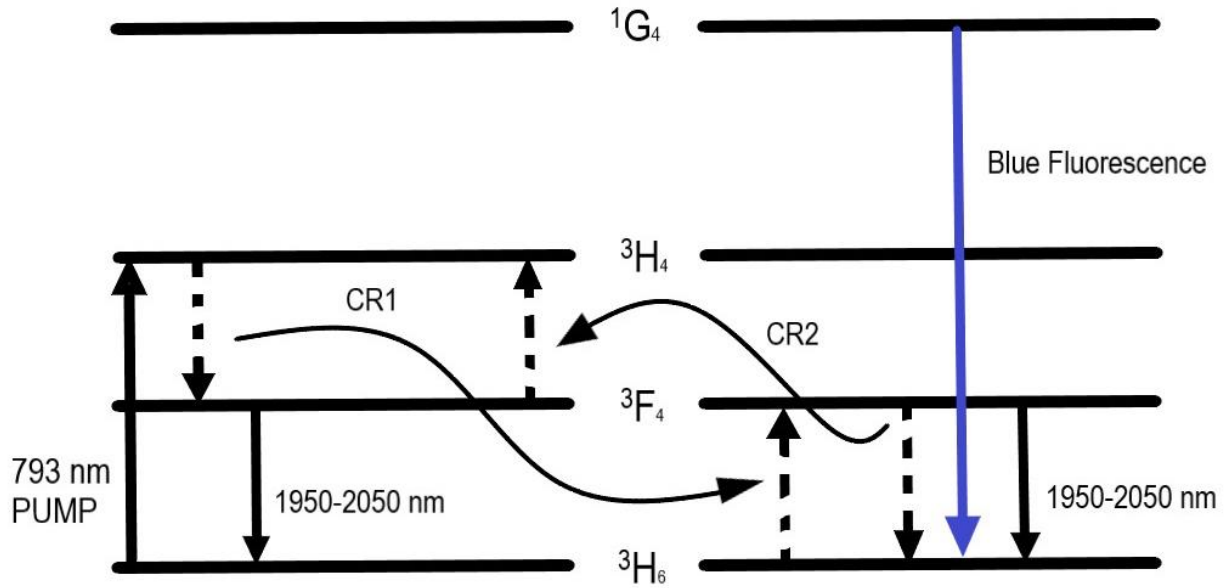
Figure 2.2 The quasi 3-level energy scheme depicting the cross-relaxation processes CR1 and CR2. Dashed arrows represent phononic emissions while solid arrows represent photonic transitions.   An additional transition not mentioned in the text is included here: the emission of blue light. The $^1G_4$ energy level is achieved through excitation processes not depicted in this energy level diagram. The emission of blue light is characteristic of Thulium laser operation which is why it is included here.

It is known as a quasi-3-level scheme because there is an extremely short-lived intermediate level between the excited $^3F_4$ state and the $^3H_6$ ground state, which is not shown in Figure 2.2, making this energetic scheme a hybrid between 3-level and 4-level schemas. Here, achieving population inversion is also robust given that the $^3F_4$ energy level is long lived at ~540 µs and the contributions of cross-relaxation [38]. The favourable cross-relaxation process (CR1) is initiated by 793 nm pumping which can be seen in Figure 2.2. Relaxation from the $^3H_4$ down to the $^3F_4$ level results in

the emission of a phonon which immediately excites the secondary Tm^{3+} ion from the ground state to the $^3F_4$ level. The transitions $^3H_4 \rightarrow {}^3F_4$ and $^3F_4 \rightarrow {}^3H_6$ are considered to be resonant processes and thus CR1 is highly likely to occur [39]. A secondary cross-relaxation process (CR2) is also seen in Figure 2.2. This is an unfavourable process since the relaxation of the secondary Tm^{3+} ion does not result in radiative emission but rather results in the emission of a phonon which causes the primary ion to re-excite to the $^3H_4$ level. Fortunately, of the two cross-relaxation reactions occurring in Tm:silica, CR1 typically occurs 92% of the time [40]. While the Tm^{3+} fiber laser efficiency does increase with increased doping, so too does the tendency for quenching by CR2 as optical center clustering increases. Hence, to reduce quenching induced by clustering, Tm^{3+} fibers are co-doped with Al_2O_3 which allows for greater doping concentrations of Tm while mitigating the CR2 process. By optimizing Tm:silica composition a maximum slope efficiency of 74% was achieved by S. Jackson in 2004 where the optimal Al:Tm^{3+} ratio was found to be 5:1 [39]. This is the most efficient Tm^{3+} fiber laser to date.

2.1.2 The Laser Cavity

The fundamental component of any laser is the optical resonator. The basic optical resonator consists of two parallel perfectly reflecting mirrors which allow for the superposition of light waves oscillating between the mirrors. If an active fiber (some glass matrix doped with TREE's) is inserted between the mirrors, and if the reflectance of one mirror is made to be wavelength dependent, such that excitation light can be pumped into the resonator, the optical resonator becomes an optical amplifier. LASER is produced by optical amplifiers that take advantage of stimulated emission to constructively interfere coherent photons. Non-coherent photons will typically destructively interfere. Thus, the optical amplifier (also known as a laser cavity) functions as both an amplifier and filter. Fiber-based laser cavities operate under the same fundamental principles of the basic laser cavity however, given the geometry of the fiber and the various optical paths that light can take through a fiber, light interference in the fiber is predominantly characterized by the reflections from the core-cladding (CC) interface, determining the transverse field patterns, while the fiber-based dielectric mirrors (known as Fiber Bragg Gratings or FBG's) at the cavity extremes serve to contain light in the core. As an illustration, consider the optical fiber of Figure 2.3 which depicts a longitudinal cross-section of a fiber in the plane of this page passing through the fiber's longitudinal axis. A photon originating at point A

will propagate through the core in a zigzag fashion where multiple reflections will occur along the fiber axis at the CC boundary. Since both reflection and refraction can occur at the CC boundary, a photon will only be contained, that is experience total internal reflection, if its angle of incidence is greater than the confinement angle (θ_c) which can be derived from Snell's law:

$$\theta_c = sin^{-1}\left(\frac{n_2}{n_1}\right) \tag{1}$$
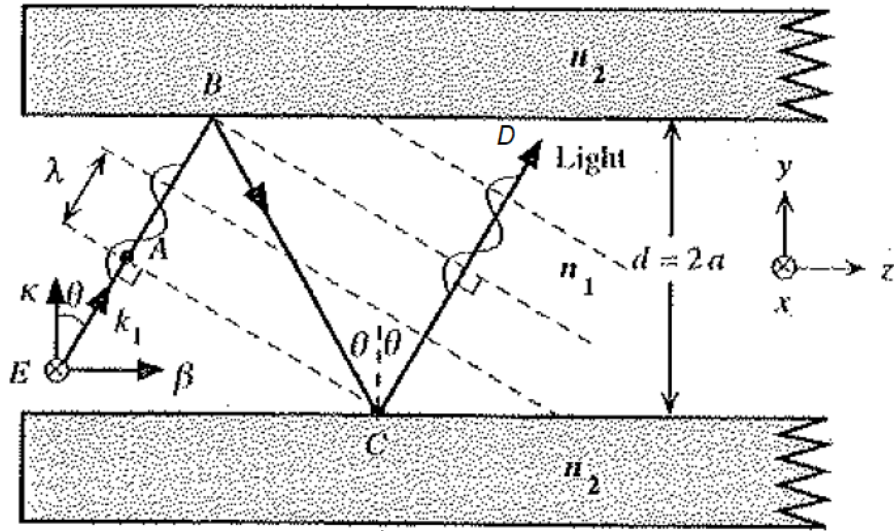
Figure 2.3 Longitudinal cross-section of an optic fiber illustrating the interference of light waves. $2a$ is the diameter of the core while n_1 and n_2 are the refractive indices of the core and cladding respectively. Ray AB is the incident ray while BC and CD are reflections. Dashed lines perpendicular to the rays represent wavefronts. Note that the wavefronts of AB are in phase with the wavefronts of CD meaning that the total phase shift between the two rays is a multiple of 2π. For total internal reflection the incidence angle θ must be greater than the critical angle defined by Snell's Law. Image from [41].

where n_1 and n_2 are the indices of refraction of the core and cladding respectively. A useful value incorporating both n_1 and n_2 is the Numerical Aperture (NA):

$$NA = \sqrt{n_1^2 - n_2^2} \tag{2}$$

which defines the solid angle in which light can be coupled into a fiber from open air and thus directly relating it to light confinement in fibers. Optical fibers implemented in fiber lasers are typically weakly guiding meaning that n_1 is nearly equal to n_2 and the NA is small. This limits the possible *modes* of propagation along the fiber core since all photons with angles of incidence below θ_c will be attenuated at the CC interface. The modes of an optic fiber are defined as the consistent

13

transverse electro-magnetic fields along the length of a fiber; they represent the optical paths taken by photons as they propagate through the fiber. The modes of an optic fiber can be found by solving the wave equation for a given fiber geometry and wavelength of light. With fiber lasers, the fundamental mode LP_{01} is most commonly employed and most desired thus, this discussion will be limited to it. The fundamental mode is desirable because it offers the highest beam quality and limits pulse broadening due to intermodal dispersion. Weakly guiding fibers are desirable since they promote the fundamental mode LP_{01} given that higher modes are easily rejected because they rebound more often and have lower angles of incidence.

In addition to the refractive indices, the core diameter of the fiber (denoted as $2a$ in Figure 2.3) also determines the allowable modes. Consider again Figure 2.3, by observing the incident optical ray AB and the optical ray CD, it is evident that wavefronts of ray AB will interfere with wavefronts of ray CD. Whether this process is constructive or destructive depends on whether the interfering photons are in phase. The phase shift ($\Delta\phi$) of the photon from ray AB to ray CD is dependent on the optical pathlength (and thus $2a$) as well as any additional phase shifts introduced from reflections (ϕ_r) at the CC boundary since CD is a second reflection of AB. For photon AB to be in phase with photon CD, the total phase shift between ray AB and CD must be a multiple of 2π. This is termed the *self-consistency condition* and is only satisfied for angles of incidence which satisfy the following equation:

$$\sin\theta = m\frac{\lambda}{4a}, m = 1, 2, \ldots \tag{3}$$

for the given fiber geometry of Figure 2.3 and where m is the mode number [41]. A subsequent result of the self-consistency condition is that the net optical path length within a cavity (L, mirror to mirror round trip distance of a photon) must be a multiple of the wavelength such that nL = λ, thus the total cavity length also contributes to the allowable modes of propagation. Given the mode limitations imposed by the NA of the fiber (considering the effect of the refractive indices on the critical angle) and mode limitations imposed by the core diameter and cavity length (according to the self-consistency condition) a useful fiber characteristic is the V-number. The V-number incorporates both the refractive indices of the core and cladding as well as the diameter of the core:

$$V = \frac{2\pi a}{\lambda} NA \qquad (4)$$

where λ is the wavelength of core light. For a given combination of a, NA, and λ, if the V-number is below 2.405 then the only allowable mode in the optical fiber is the fundamental mode LP_{01}. It is now evident that the optical resonator behaves as an optical filter both spectrally and modally based on the properties of fiber optic waveguides.

From the previous section the reader is already aware that stimulated emission results in the production of coherent photons. Since an incoming trigger photon can elicit an atom in an excited state to emit a coherent photon in the same direction, we say that the light has been amplified. It is now necessary to examine the occurrence of this phenomenon in an optical cavity more closely. An optical cavity is pumped via a seed laser where seed light reaches the core and pumps the optical centers into an excited state. An original core photon of the lasing wavelength is produced via spontaneous emission whereby an optical center spontaneously relaxes. This original photon then elicits the production of coherent photons as it propagates through the core and stimulates additional optical centers to relax. Wavelength selective mirrors at the extremes of the cavities allow the same original photon to make several round trips through the core eliciting further production of coherent light. Thus, for the efficient production of laser light the spectroscopic mirrors at the ends of the cavity must be properly tuned to ensure emission of laser light while still containing enough coherent light to continue the process of stimulated emission. FBG's are ideal spectral mirrors for fiber-based cavities since they can be etched into fiber cores via UV radiation allowing for relatively simple microfabrication. They consist of a grating of materials with varying refractive indices. By controlling the thickness of each grating, the grating period, and their respective refractive indices, wavelength selective reflection can be achieved.

In fiber laser cavities an impasse is reached. The fundamental mode is desired (LP_{01}) meaning that a low core diameter and NA is required (from Eq. (4)) however, this makes pumping the core difficult as only light rays within a small solid angle defined by NA will be coupled into the core. High power seed lasers with single mode output could theoretically be used to pump such a cavity. However, these are extremely costly and, thus, may not be practical to implement. To combat this issue, cladding pumped technology was developed where active fibers forming the laser media of optical cavities were given an additional cladding of high NA to increase the acceptance angle of

light. Thus, the active fiber now consists of a core, a first cladding for launching pump light as well as containing core light, and a second cladding for containing launched pump light. In this way pump light can be launched into the first cladding and subsequently excite optical centers in the core by zigzagging across it. The higher NA of the first cladding makes it multi-modal meaning that higher modes other than the fundamental mode can propagate within it. This is advantageous as the number of excited optical centers is directly proportional to the number of interactions between the pump light and the fiber core. Given that higher modes rebound more frequently from the cladding-cladding interface (of the first and second cladding in a double clad fiber), more pump light will propagate across the active core increasing the number of excited optical centers, thus making higher modes desirable. Further, it was discovered by Snitzer that by making the cladding-cladding boundary octagonal, reflections from this boundary could be increased making the fiber laser even more efficient. Higher modes used to excite the core can be problematic. Since not all the incident pump light is absorbed by the core it is possible to have residual, undesirable, cladding modes at the output of the fiber laser. Thus, in many fiber lasers, a cladding mode stripper is used at the output to maintain beam quality. This consists of a small, buffer-less section of passive fiber (after the output-coupling FBG) that is affixed to a heat-sink using a cladding index matched epoxy adhesive. Residual pump light that remains in the outer cladding is ejected directly into the heat-sink via the epoxy-cladding interface, allowing for downstream components to remain unaffected.

2.2 Vascular Tissue Optical properties and Ultrastructure

The energy sealing of blood vessels involves dosing vessels with laser light until blood flow has ceased; a process which is directly facilitated by the biomechanical response of tissue elicited by increased thermal activity via laser light interaction with tissue. In order to understand this response, we must first develop a knowledge base of both the molecules which are responsible for light absorption and the molecules which contribute to the structural integrity of vascular tissue. Most medical lasers use tight focusing to maximize efficiency and to maintain high degrees of precision, meaning that spot sizes are typically below 1 mm in diameter. By the same reasoning, wavelengths selected for use in medical applications are typically selected for high absorbance in tissue which directly results in relatively shallow optical penetration depths. Thus, the volume in which optical-tissue interaction takes place is typically quite small as it is governed by the spot size of laser light at the tissue surface as well as the optical penetration depth. This means that

initially, a sub cubic millimeter tissue volume is involved in light interaction. Thus, in determining the mechanical response of tissue to laser irradiation, we are primarily concerned with the behaviour of the microscopic structural components (the ultrastructure) of tissue rather than the mechanical behaviour of the tissue bulk. This section will concisely discuss the contribution of various chromophores present in blood to the overall absorbance of whole blood and will also outline the ultrastructural components of blood vessels.

2.2.1 Spectroscopic Properties of Blood

Blood is the primary chromophore in vascular tissue and is considered a connective tissue which consists of a liquid base containing cells and cell fragments. The liquid portion of blood, termed plasma, consists of 91% water and 9% other substances including proteins. The proteins found in plasma can be classified into albumins (58%), globulins (38%), or fibrinogen (4%) [42]. These proteins have a significant contribution to the optical absorption spectra of blood (Figure 2.4).
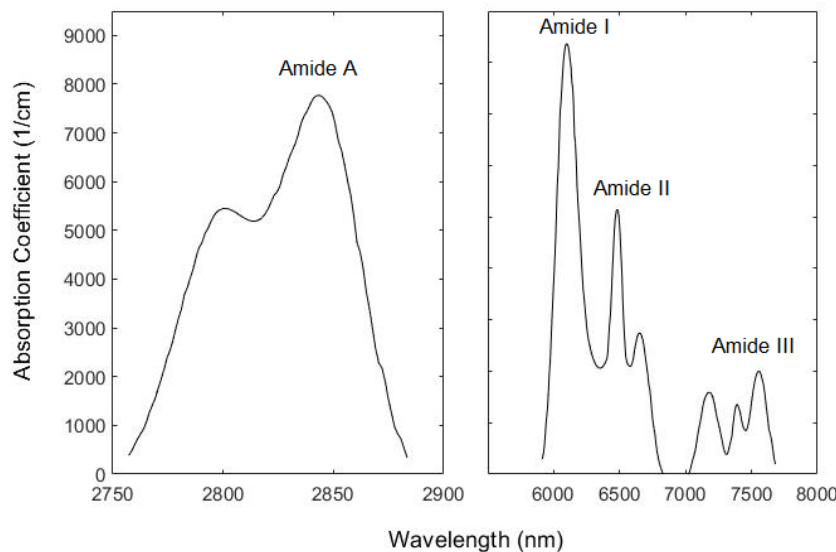

Figure 2.4 The absorption bands of proteins are determined by molecular vibrations within Amide groups. The horizonal axis represents wavelength in periods per centimeter. The strongest absorption peaks are in the Amide I and Amide A bands. Amide A band corresponds to wavelengths centered at ~3000 nm (3500 cm^{-1}) while the Amide I band corresponds to wavelengths centered at ~6000 nm (1650 cm^{-1}). Both these spectral peaks are highly significant in laser-tissue interaction as they coincide with absorption maxima of water. Data adapted from [43] and corroborated with data from [44–46].

The cells form the solid portion of blood of which 95% are erythrocytes, commonly known as red blood cells (RBC's). RBC's are biconcave cells which are responsible for carrying oxygen to tissues. The oxygen carrying molecular constituent of each RBC is hemoglobin which makes up

about 33% of the total RBC volume and is responsible for its red pigment. Each hemoglobin molecule consists of four polypeptide chains (which also contribute to the amide absorption bands of Figure 2.4), each of which contains a red-pigmented molecule called heme which ultimately bonds to oxygen using an iron atom. Hemoglobin exists in two primary states: oxygenated and deoxygenated, where, oxyhemoglobin is bright red and deoxyhemoglobin is a darker red. The colour change between molecular oxygenation states directly translates to different responses to light, meaning that the absorption spectra of each molecule differ (Figure 2.5). This difference in absorption partially explains why Kimel et al. found a significant difference in the vascular tissue response in [47] to the KTP laser which emits green light (520-560 nm). The remaining 5% of cells in blood are white blood cells and cell fragments called platelets whose contribution to light absorption comes from their protein content.
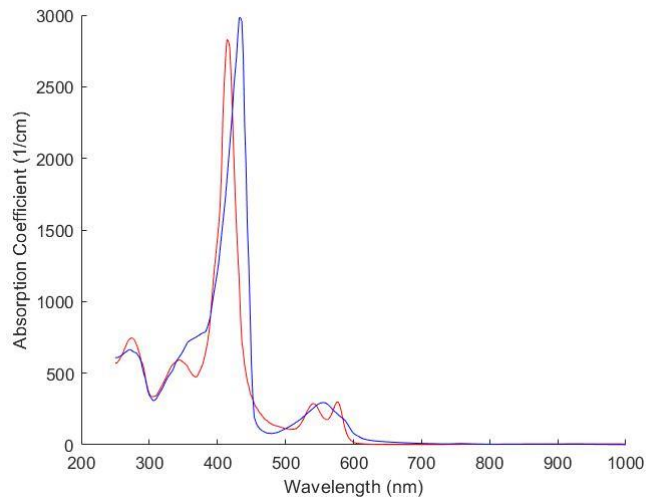

Figure 2.5 The absorption spectrum of oxy and deoxyhemoglobin. Note the difference in the absorption peaks in the 400-500 nm band (green light). Data originally compiled by Scott Prahl, Oregon Institute of Technology [48].

Whole blood, both cellular and liquid portions combined, is 80% water thus the primary chromophores in blood are proteins, heme molecules, and water. Water is by far the dominant chromophore at any hydrolytic wavelength, such as the 2 µm wavelength from a Thulium laser (Figure 2.6) [49]. Thus, the overall absorption spectrum of blood is a composition of each of the absorption spectra of Figures 2.4-2.6 where each of the primary chromophores form their own absorption bands. Assuming whole blood is Lambertian in nature (expanded on in a later section) and that the distribution of chromophores within it is homogenous, its absorption spectrum can be derived from the following equation:

18

$$\mu_a(\lambda) = [Hb]\mu_{Hb}(\lambda) + [H_2O]\mu_{H_2O}(\lambda) + [P]\mu_P(\lambda) \qquad (5)$$

where μ_a is the overall absorption coefficient, μ_x represents the absorption coefficient of the chromophore specified by x, and square brackets represent the concentration of the chromophore in whole blood. The absorption coefficient pertaining to Hb must be selected appropriately depending on the oxygenation state of the blood.
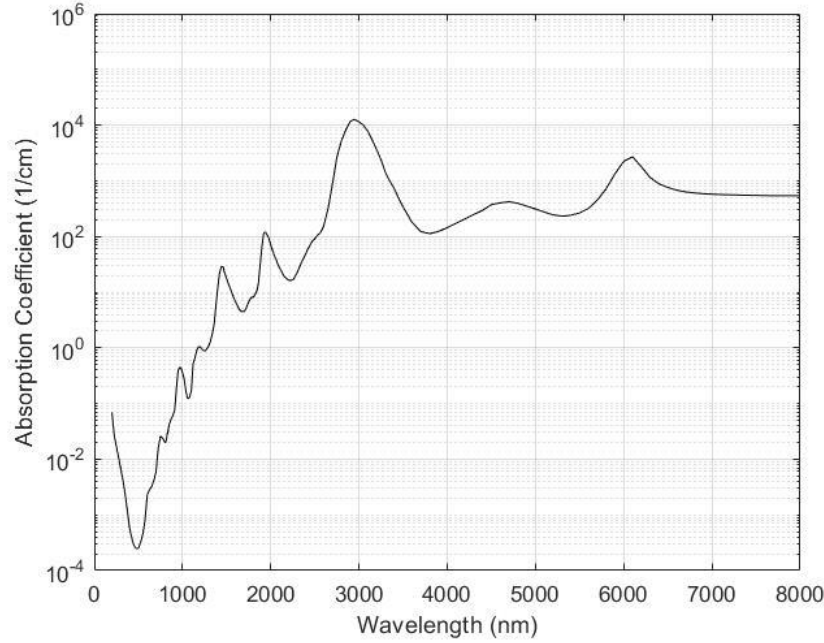

Figure 2.6 The absorption spectrum of water. Whole blood is 80% water and thus water is the dominant chromophore in blood. Note the absorption peaks at 2 µm, 3 µm, and 6 µm. These absorption peaks are often used in surgical laser technology as they allow for the efficient deposition of energy into tissue. Both the 3 µm and the 6 µm peak overlap with the absorption peaks of the Amide I and Amide A bands [50].

If we assume oxygenated blood, then the overall absorption spectrum of blood up to 8000 nm is given by Figure 2.7. It is clear that wavelengths in the 2500-8000 nm band offer far greater absorption than in the 2000 nm band, however, as mentioned in the previous section, wavelengths greater than 2000 nm are not ideal for medical applications as they cannot be guided by silica-based fibers. Green light also features a higher absorption coefficient than 2000 nm light, however, as mentioned previously, green light elicits different tissue responses in oxygenated and deoxygenated blood which can be problematic in the development of a hemostatic instrument. Additionally, green light in only strongly absorbed by blood, meaning that visible light would be largely ineffective when used in other tissues. Thus, the 2000 nm wavelength offers the greatest

absorption in whole blood while still having the potential to be easily integrated into medical instruments and has the potential to be effective across multiple tissue types.
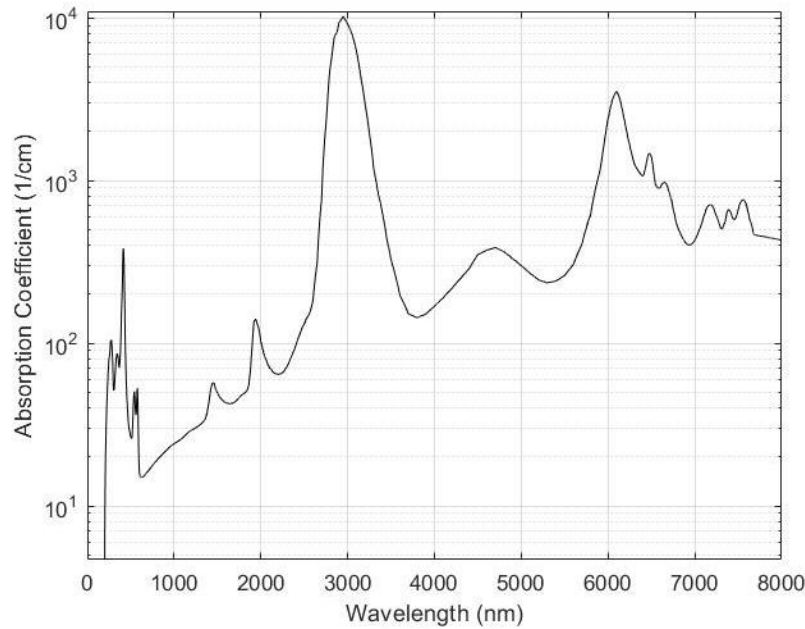

Figure 2.7 The absorption spectrum of whole blood. Absorption in the visible spectrum is dominated by hemoglobin while the prominent peaks at 1500 nm and 2000 nm are fully attributed to water. The maxima of the spectrum is a result of the combination of water and Amide A absorption at 3000 nm. The peak at 6000 nm is also an overlap between water absorption and the Amide I band.

2.2.2 The Ultrastructure of Blood Vessels

Vessels are highly dynamic tubules that are capable of adapting to varying physiological conditions. Arteries must deform under the undulations of systole and diastole while maintaining structural integrity. They are also capable of constricting in response to injury or hypotension. Veins function as channel-based passages of blood where the flow of blood is regulated by valve like structures formed by folds in the luminal lining. The cumulative volume of veins in the body serve to contain a reservoir of blood which can be accessed when physiologically nesessary. Thus, veins can modify their volumes to control the total volume of blood being circulated by increasing or decreasing the volume of the vascular reservoir. The vessel wall of both arteries and veins consists of three primary layers: the *tunica intima*, *tunica media*, and *tunica adventitia*, where, the intima lines the lumen and the adventitia forms the outermost wall. The intima consists of a delicate endothelium anchored in a basement membrane which is surrounded by an elastic lamina, the lamina propria [42]. Given its delicate nature, the intima has very little contribution to the structural integrity of the vessel [51]. The media is the thickest layer of the vessel wall in arteries.

It consists of a mixture of smooth muscle cells and connective tissue primarily composed of elastin and collagen. Amongst arteries the composition in parts of smooth muscle, collagen, and elastin vary with proximity to the heart. Larger arteries proximal to the heart are considered elastic, having a low collagen to elastin ratio and a relatively small amount of smooth muscle. The Aorta, for example, is highly elastic as it must adapt immediately to the pumping phases of the heart. Moving distally from the heart the diameter of arteries decreases linearly while the collagen to elastin ratio increases as does the relative amount of smooth muscle [51,52]. Smaller arteries, the focus of this work, are considered to be muscular arteries where smooth muscle is the primary contributor to their mechanical behaviour. Veins have a thin Media in comparison to arteries, however, the few smooth muscle cells which reside there are still capable of regulating vessel diameter given the low pressure of blood within veins. The thickest layer in veins is the Adventitia which primarily serves as a connective medium between vessels and the tissue. The Adventitia of arteries is thinner but also contributes to their mechanical behaviour given the presence of collagen and elastin. The Adventitia plays an important role in vascular biomechanics as this layer determines the degree of tethering to the tissue bulk.

In vessel walls, collagen and elastin are corrugated and intertwined, allowing for a blend of strength and elasticity (Figure 2.8 A). Elastin is a long macromolecule and, as its name suggests, is extremely elastic, capable of stretching to 2.5 times its original length. This means that it has a relatively low elastic modulus of 0.5 MPa. Elastin tends to form rubber-like masses within tissue and typically does not exist in any sort of hierarchal organization unlike collagen [52]. Collagen is the main load carrying component of tissue and, in fibril forming collagens (types I, II, III, V, XI), is typically in the form of a triple helical structure known as a tropocollagen (TC). TC has a diameter of ~1.5 nm and length of 280 nm [52]. Intermolecular binding between adjacent TCs leads to the formation of fibrils with diameter ~50 nm which in turn undergo a binding process mediated by proteoglycans to form fibers with a diameter of ~1 μm [44,53]. In load bearing tissues, such as ligament and tendon, collagen fibers are arranged parallel to the direction of the applied force to maximize strength. In other tissues where multidirectional forces are common, such as skin and the female vaginal tract, the organization of collagen fibrils is much more complex and is often specialized to accommodate the intended function of the tissue without damage. For instance, in blood vessels, collagen fibers are arranged obliquely to the longitudinal axis allowing for the accommodation of physiological stresses in both circumferential and longitudinal

directions. Collagen fibers in the Adventitia are more longitudinally aligned than collagen fibers in the Media (Figure 2.8 C-D) [54].
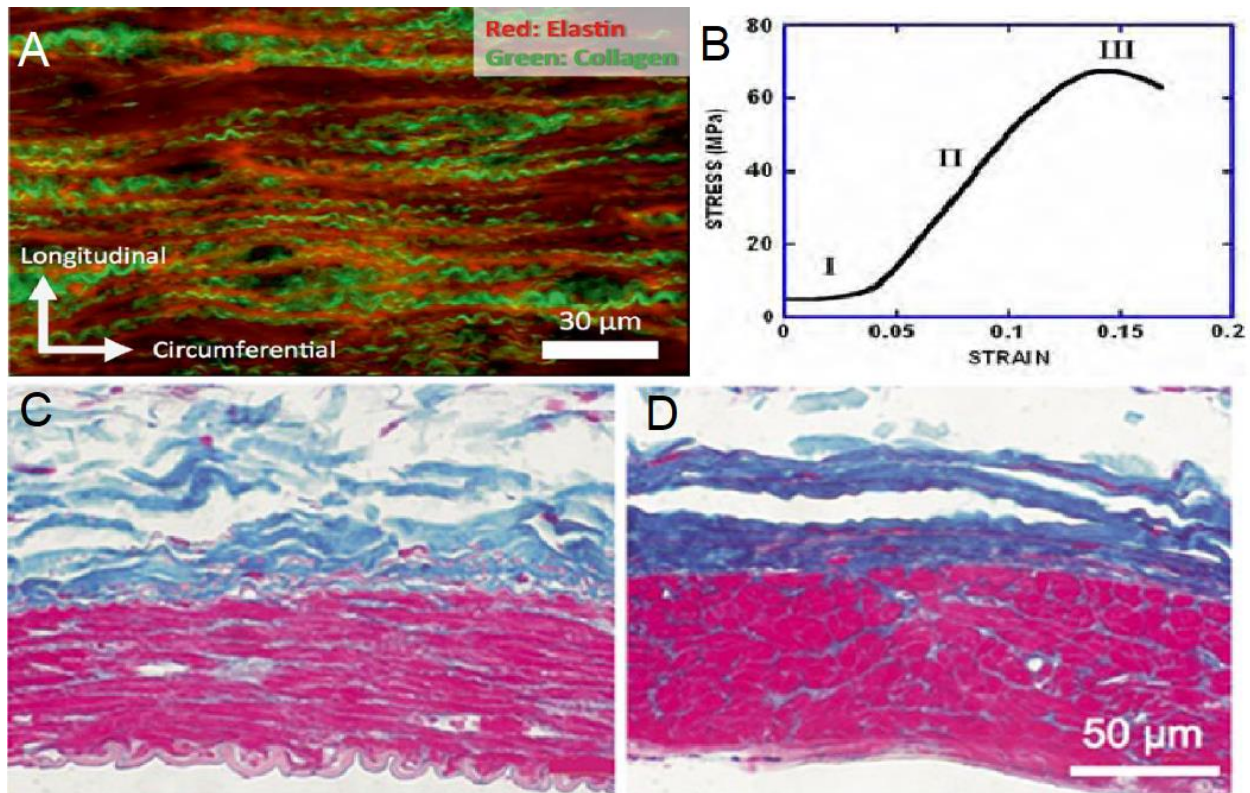

Figure 2.8 The corrugation of elastin and collagen in vessel walls (A) [51]. Notice the bundled collagen fibers (the wave-like green structures). The three-phase stress-strain response of collagen (B) [53]. A histological cross section of a muscular artery (C). A histological longitudinal section of a muscular artery (D). For C and D collagen is stained blue, smooth muscle is stained pink, while elastin has no staining and can be seen as white spaces between blue collagen strands as well as sporadically between smooth muscle cells [51]. Collagen fibers in the Media (largely pink section) are nearly circumferentially aligned whereas collagen fibers in the Adventitia (largely blue area) are more so longitudinally aligned. Note the circumferential orientation of the smooth muscle cells.

Collagen has a three-phase response to mechanical stress: the toe (I), linear (II), and failure (III) phases (Figure 2.8 B). During the toe small amounts of stress result in insignificant strain as bundled collagen fibers are simply straightened out. Once the fibers are completely straightened, they begin to experience strain linearly with stress until failure. Type I collagen is the primary molecular constituent of blood vessel walls. In the liner phase, it has an elastic modulus of ~740 MPa and an ultimate tensile strength (UTS) of 70 MPa [55]. Soft tissues whose primary structural component is collagen will have a stress strain relationship which closely matches that of collagen. Of course, the ultrastructural arrangement of collagen in those tissues must also be taken into consideration. In tendons, for example, the majority of collagen fibers are linearly aligned with

the longitudinal axis. Thus, the stress strain relationship of a tendon longitudinally nearly matches that of collagen [51]. Given that collagen fibers are found both in the adventitia and the media, and that their orientations in each of these layers are different, the contribution of collagen to the mechanical response of vascular tissue at the microscopic level will be anisotropic. The contribution in the longitudinal direction by collagen will be greater given that most collagen is found in the adventitia and collagen fibers in the adventitia are aligned more so with the longitudinal axis [54].

Smooth muscle cells (SMCs) are rhomboidal in shape where their major axes are aligned circumferentially (Figure 2.8 C & D). Unlike collagen, their stress-strain response is highly viscoelastic, meaning that stresses experienced in response to strain are time dependent. The viscoelastic nature of SMCs is believed to be a result of inherent fluid flow resistance, however, there is evidence that SMC viscosity is a result of a reorganization of intracellular components during loading and unloading [56]. The primary cellular constituents contributing to SMC mechanics are actin-myosin stress fibers which are oriented along their major axes. As a result, SMCs feature an anisotropic response to stress where their major axes have a much higher stiffness than their minor axes with elastic moduli of 14.3 and 2.8 kPa respectively [57]. The break force of these actin-myosin fibers has been found to be 377 nN corresponding to an UTS of approximately 3 MPa assuming a cross-sectional radius of 100 nm [58]. The mechanical behaviour of SMCs is further complicated by their response to physiological stimuli. The contraction of SMCs induced by nor-epinephrine has been shown to alter their mechanical properties significantly. In the contracted state they lose their rhomboidal shape and become more uniform while actin-myosin fibers rearrange causing the SMCs to become less anisotropic and stiffer. The elastic modulus of contracted SMCs in the major and minor axes has been measured to be 88.1 and 59.0 kPa respectively [57]. Therefore, as a whole, the contribution of SMCs to the microscopic mechanical response of vascular tissue is both directionally dependent and dependent on the physiological state of the SMCs.

2.3 Laser Tissue Interaction Pertinent to The Energy Sealing of Vessels

As was previously mentioned, the energy sealing of vessels is an optical-thermal-mechanical process. The reader is already familiar with those constituents of tissue which contribute to the overall process from the previous section. The reader is also familiar with LASER energy and its

production. In order to unify both of these concepts and to develop an understanding of the energy sealing process, it is necessary to discuss how LASER energy interacts with tissue. With lasers, the parameters of concern are wavelength, spot size, irradiance, and exposure time, while with tissue the concern is the presence of chromophores and ultrastructural geometry. Each parameter contributes to the overall laser-tissue interaction process resulting in a quite complex phenomenon. There are several regimes of laser-tissue interaction including photochemical, photodisruption, and photothermal [59]. All concepts discussed in this section will be concerning photothermal processes where the effects observed in tissue will be attributed to thermal energy deposition as a result of optical energy absorbance. This section will be written under the assumption that the energy sealing of vessels is driven by tissue coagulation (sometimes referred to as blanching in literature) and thus it is also important at times to consider tissue ablation, the volumetric ejection of tissue due to thermal energy deposition, as pure coagulation occurs at sub-ablation energies and the achievement of ablation is undesirable. Therefore, concepts such as the ablation threshold, widely discussed in laser-tissue interaction literature, are useful here as they define the upper limits of desirable energy driven effects.

2.3.1 Optical to Thermal Energy Conversion in Tissue

A focused beam incident on a tissue surface experiences a small amount of reflectance (R) both specular and diffuse in nature. That portion of the beam which is transmitted into the tissue (where transmittance is equal to 1-R) can then experience one of two fates: absorption or scattering. In the interaction of mid-infrared (MIR) light and tissue, scattering is negligible given the high absorbance of water in that band and therefore $\mu_a \gg \mu_s$ where μ_s is the scattering coefficient. Absorption is the process where optical energy is converted into molecular kinetic energy which manifests itself at a macroscopic level in the form of heat. It is quantized using several different units of measure the foremost of which being absorbance, preferred by chemists, and the absorption coefficient, preferred by physicists and engineers. Specifically, the absorption coefficient is a measure of the fraction of light absorbed per unit path length and thus it represents the rate of optical to thermal energy conversion. Materials whose absorption coefficient is linearly proportional to the concentration of chromophores obey Beer-Lambert's law [60]. This is the case with most materials. The Beer-Lambert law fails to represent absorption when a property of the

absorbing medium causes the absorption characteristics of molecules to change. The absorption of Lambertian materials is given by:

$$E(z) = E_o(1 - R)e^{-\mu_a z} \tag{6}$$

where the remaining energy in Joules of the incident beam at some depth z, E(z), is proportional to the fraction of the incident energy transmitted into the tissue, E_o(1-R), and the absorption coefficient. Therefore, for laser-tissue pairings where $\mu_a \gg \mu_s$ (such as with 2 μm light and vascular tissue), the total absorbed optical energy by an element of tissue with thickness z is given by E_o - E(z). The optical penetration depth is defined as the point along the axis of irradiation at which the energy of the beam is reduced to 37% or 1/e and is given by:

$$\delta = \frac{1}{\mu_a} \tag{7}$$

for a tissue and incident irradiation where $\mu_a \gg \mu_s$ [61]. For 1942 nm light incident on vascular tissue $\mu_a = 140$ cm^{-1} and $\delta = 71.4$ μm from Figure 2.7. When discussing any concept pertaining to laser-tissue interaction, it is important to define the optical zone (OZ) which is that portion of tissue in immediate contact with the incident irradiation. The OZ is the approximated cylindrical volume primarily defined by the beam spot size at the tissue surface (usually taken to be the beam waste $2\omega_o$) and the optical penetration depth. The characteristic dimension of the OZ is the measure used in thermal energy diffusion calculations. In the case of narrow-beam irradiation, where $2\omega_o < \delta$, the characteristic dimension of the OZ is $2\omega_o$ [62]. In the case of broad-beam irradiation, where $2\omega_o > \delta$, the characteristic dimension of the OZ is δ [62]. Given that $2\omega_o$ is 206 μm the characteristic dimension of the OZ in this work is δ.

Wavelength notwithstanding, the ultimate determinant of thermal laser-tissue interaction is the spatial and temporal energy density which, in continuous wave operation, is characterized by spot-size at the tissue surface and average power respectively. For instance, the ablation threshold is defined by an irradiance, that is an energy per unit time per unit area, and formally is the minimum irradiance required to initialize the volumetric ejection of tissue. In order to achieve contactless energy sealing, the spot size and power of the incident beam must be regulated such that the irradiance is kept below the ablation threshold and only coagulation is induced. Exposure time is the total time span of a single dose of irradiation (not to be confused with total therapeutic

25

time which is the total time span of all doses required to achieve some therapeutic effect). Exposure time is an incredibly important aspect in laser-tissue interaction as it determines the degree of dynamic tissue effects (discussed in the next section) contributing to the coagulation process and determines if the deposited energy will be thermally confined, that is, if the deposited energy will be mostly confined to the OZ. For laser-tissue pairings where $\mu_a \gg \mu_s$ thermal confinement is achieved when the exposure time is shorter than the characteristic thermal diffusion time of some geometry of tissue (the amount of time required for heat to diffuse over the characteristic dimension of the OZ). Thus, the condition for thermal confinement is given by:

$$t_e < \tau_d = \frac{d^2}{4\alpha} \tag{8}$$

Where t_e is the exposure time, τ_d is the characteristic thermal diffusion time, d is the characteristic dimension of the OZ as defined previously, and α is the thermal diffusivity of the tissue [61,63]. For an incident irradiation of 1942 nm on human Aorta tissue (thermal diffusivity = 1.306E-7 m^2/s, [64]) and a penetration depth of 71.4 µm, a pulse will be thermally confined if it is less than 9.8 ms according to Eq. 9. Note that the characteristic thermal diffusion time is heavily dependent on the tissue geometry in question thus variations in Eq. 4 can be seen throughout the literature depending on how the OZ is characterized [61]. Nonetheless, thermal confinement is an extremely important concept in the energy sealing of vessels as, depending on the optical penetration depth, it may or may not be desired. In the context of this work, the optical penetration depth is small in comparison to the diameter of vessels, and, since uniform heating is desired in the energy sealing of vessels, thermal confinement is not desirable. In fact, given the size of the OZ in this work, most tissue within a cross section of a vessel will be heated via thermal diffusion.

Given a thermally confined exposure time, t_e, for some combination of laser and tissue parameters, the temperature rise of some element at depth z within the OZ is given by:

$$T(z, t = t_e) = \frac{Q}{\rho c_p} = \frac{\mu_a \Phi_o e^{-\mu_a z}}{\rho c_P} \tag{10}$$

Where $Q = E/V$ and is the energy deposited per unit volume of tissue in J/m^3, ρ is the tissue density in g/cm^3, c_P is the specific heat constant in J/kgK, and Φ_o is the incident fluence in J/m^2 [65]. The term $\Phi_o e^{-\mu_a z}$ represents the remaining photons per cross-section at some depth z. For example, the temperature rise associated with one 1 ms pulse of a 1942 nm Tm^{3+} fiber laser irradiating

vascular tissue ($2\omega_o$ = 206 µm, δ = 71.6 µm, Power = 7 W, ρ = 1102 kg/m³, c = 3306 J/kgK) is 114.8˚K, assuming a cylindrical OZ. It should be noted that E (in Q = E/V) is the total energy deposited into the tissue and thus is only the portion of incident energy that is *transmitted* into the tissue. Thus, for a more accurate calculation of temperature rise, the reflectance (R) at the air tissue interface must be considered. Temperature rise becomes:

$$T(z, t = t_E) = \frac{Q}{\rho c} = \frac{(1 - R)\mu_a \Phi_o e^{-\mu_a z}}{\rho c_P} \tag{11}$$

Eq.'s 10 and 11 describe the temperature rise in an element of tissue due solely to optical energy deposition which would be sufficient if $t_e < \tau_d$. However, this work deals with the energy sealing of small vessels where vessel diameters range from 200 µm to 2 mm meaning that thermal confinement would result in a high thermal energy concentration in a very superficial portion of the vessel. This would induce a high thermal gradient, resulting in extreme localized forces which would make vessel rupture more likely. Ergo, in the energy sealing of vessels, exposure times exceeding τ_d are desirable such that thermal energy is allowed to diffuse within the tissue and the thermal gradient is decreased. Therefore, in order to represent the total temperature change in time of a tissue element, a model is required which considers the conduction of heat energy in tissue as well as the deposition of heat energy due to optical energy absorption. For this purpose, the thermal conductivity equation for cubic geometries will be adapted from [66]:

$$\frac{\partial T}{\partial t} = \alpha \left(\frac{\partial^2 T}{\partial x^2} + \frac{\partial^2 T}{\partial y^2} + \frac{\partial^2 T}{\partial z^2} \right) + \frac{q'''}{\rho c_p} \tag{12}$$

On the right side of Eq. 13 the first three terms represent the temperature change due to heat flux in the x, y and z directions respectively, while the fourth term represents temperature change as a result of heat generated internally by the tissue element. The heat generation of an element of tissue is due to metabolic processes. If it is assumed that the amount of heat energy produced due to metabolic processes is insignificant in comparison to the thermal energy deposition by optical energy absorbance, then this term can be replaced by Eq. 11. While Eq. 11 does describe the temperature increase due to optical energy deposition, it only suffices for the depth dimension. To bring this equation into three-dimensional space the optical energy distribution in the radial direction (from beam center to beam edge) must also be considered. In collimated beams the optical energy is evenly distributed radially however in focused beams, used in this work, optical

intensity follows a Gaussian distribution where the intensity of the beam is greatest at the center and nearly zero at the edges. Thus, temperature increase due to optical energy deposition for some tissue element at depth z and radial position r (where $r^2 = x^2 + y^2$) can be expressed by the following equation:

$$T(z,r) = \frac{\mu_a}{\rho c_P}(1-R)\Phi_o e^{\left(-\frac{2r^2}{w_o^2} - \mu_a z\right)} \tag{13}$$

where $e^{-\frac{2r^2}{w_o^2}}$ is the added term in the numerator which describes the Gaussian intensity distribution in the radial direction. By replacing the final term in Eq. 12 by Eq. 13, a formulation for the change in temperature of a cubic tissue element with time due to both heat conduction and energy deposition is achieved.

2.3.2 Shifts in Tissue Optical Properties in Response to Thermal energy

As tissue is subjected to irradiation, energy is either stored in the form of chemical changes ("non-reversible changes" e.g. thermal denaturation) or in temperature elevations ("reversible changes"), both of which lead to shifts in the fundamental optical properties of tissue such as refractive indices and absorption coefficients. Changes in these parameters ultimately result in a change of energy deposition behaviour which in turn leads to changes in the coagulative process. At a microscopic level, the thermal denaturation of molecules triggers shifts in their structure. It is those structural changes which are ultimately responsible for the mechanical forces induced in tissue post laser exposure. If the induced forces exceed the UTS of the tissue microstructure then tissue will rupture.

A useful measure for approximating the extent of non-reversible damage post or during irradiation is the Arrhenius Damage Integral. This concept was developed by the Swedish scholar Svant Arrhenius in 1889, who interestingly, was good friends with William T. Bovie during his time at John Hopkins University. The extent of thermally denatured tissue, in an irradiated volume of tissue, is dependent on both the intensity of the energy delivered as well as the duration of irradiation [44,67]. For a given volume, that fraction of surviving tissue after time t (i.e. tissue that has not been thermally denatured) is given by:

$$\frac{c_x(t)}{c_x(0)} = e^{-\Omega} \tag{14}$$

where, $c_x(t)$ represents the remaining number of units in the original state at time t, and Ω is a unitless parameter usually termed the thermal damage factor [68]. When $\Omega = 1$ sixty-three percent of the targeted tissue has been denatured or damaged and is the point chosen by Henriques in [67] to indicate complete necrosis of pig basal epidermis. The thermal damage factor can be calculated from the Arrhenius integral:

$$\Omega = A \int_0^t e^{-\left(\frac{E_A}{RT(t)}\right)} dt \tag{15}$$

Where A is the pre-exponential constant in s^{-1} which is dependent on both position and temperature as it represents the rate of molecular collisions, E_A is the activation energy in cal/mol, and R is the universal gas constant in cal mol/K [69].

Schomaker et al. in [70] found that etch depths created in collagen gels using a tuneable Co:MgF$_2$ laser (1.8-2.2 µm) varied significantly from expected results. Etch depths generated at wavelengths shorter than 1942 nm were found to be less than expected while etch depths generated at wavelengths longer than 1942 nm were found to be more than expected. This result suggested a dynamic behaviour in the absorption coefficient of water with changes in temperature. The absorption peak associated with the 1942 nm wavelength, seemed to shift to shorter wavelengths, a result associated with the weakening of the hydrogen bonds between adjacent water molecules resulting in a change in length and strength of the OH bond [44]. Efforts to model this phenomenon were carried out by both Jansen et al. in [65] and Lange et al. in [71] who created similar linear models to map the change in μ_a with varying temperatures. According to Jansen the absorption coefficient at some temperature T is given by:

$$\mu_a(T) = \mu_{a,o} + \beta \Delta T \tag{16}$$

Where $\mu_{a,o}$ is the absorption coefficient at 22°C and β is a coefficient determined experimentally. Values of β for wavelengths 2.12, 2.09, and 2.01 µm can be found in [65]. Considering the hypothetical temperature increase of 114.8 K calculated previously, and, using an interpolated value of β at 1942 nm (-0.04745 mm^{-1}/°C) μ_a changes from 140 cm^{-1} at 295°K to 80 cm^{-1} at 410°K, this after only a single exposure of 9.8 ms.

At temperatures exceeding 60°C, thermal denaturation of tissue begins, a non-reversible process where collagen molecules become disordered and tightly packed [72]. This, in essence, is

coagulation. The compacting of collagen molecules in vessel walls is one of the primary contributors to the energy sealing process [73]. Tissue dehydration occurs concurrently with collagen compaction and is a result of rapid heating. The combined effect of these two phenomena have different ramifications depending on the wavelength in use. The packing of collagen molecules tends to increase the absorption coefficient simply because there are more molecules per unit path length, while the effect of dehydration will either increase or decrease the absorption coefficient depending on the wavelength's proximity to a local absorption maxima of water. At visible wavelengths and shorter near infra-red (NIR) wavelengths, the denaturation of tissue leads to an increased absorption coefficient [74,75]. As wavelength increases into the NIR spectrum and absorption begins to rely increasingly so on the presence of water, the effects of dehydration and collagen compacting tend to cancel and the absorption coefficient remains relatively unchanged [72]. It can be postulated then, that as the 1942 nm absorption peak is approached at the onset of the MIR spectrum, the effect of dehydration will supersede collagen compaction and the result will be an overall decrease in absorbance of tissue. This is in agreeance with the change in the absorption coefficient calculated from Eq. 16. The continued heating of coagulated tissue (beyond 217°C) will result in the formation of a carbonized layer termed char. Char formation is different from coagulation in the sense that it is the result of a complete chemical change, not simply a change in molecular geometry, and as a result, the contribution of a new chromophore must be considered in the overall absorption of tissue. Unfortunately, the absorption spectrum of char is only available in the literature between 300 and 1100 nm and further conclusions of its affects in the 2 µm regime cannot be made.

According to Welch in [76] and Wilson in [77], only 3% of light undergoes specular reflection at the air tissue interface while it has been demonstrated that diffuse reflectance can reach 20% in many in-vivo scenarios. Changes in tissue temperature can result in significant changes in reflectance and, as with the absorption coefficient, these changes can be both reversible and non-reversible. Non-reversible effects are the result of tissue denaturation, once tissue has been coagulated its refractive index changes greatly and thus so too does reflectance. Non-reversible changes in reflectance can be attributed to many factors such as: thermal lensing (further discussed later), thermal expansion, change in scattering behaviour due to temporary change in size of scatterers, and the dependence of the refractive index of water on temperature, the most significant of which being the last [78]. Nishioka et al. in [79] studied the dynamic behaviour of tissue

reflectance during exposure to a Ho:YSGG laser at 2.1 µm. His findings concerning both reversible and non-reversible effects are neatly summarized in Figure 2.9.
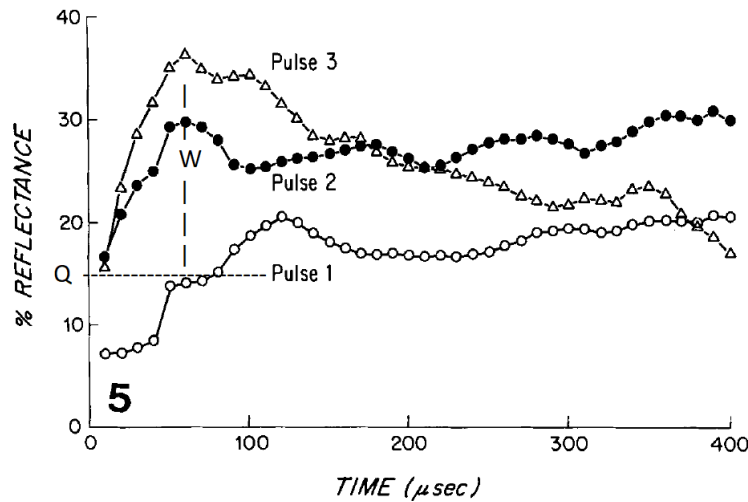

Figure 2.9 Reflectance Vs. time curves for sequential laser pulses with a laser radiant exposure of 90 J/cm^2. Modified from [79].

No significant change in reflectance is observed in Pulse 1 until approximately 50 µsec where a sharp increase is observed. This sharp increase is a result of tissue denaturation and occurs only after sufficient energy has been delivered to the tissue to cause coagulation. This change in reflectance is non-reversible (marked as Q in Fig. 1), an effect which is evident at the onset of each of the subsequent Pulses 2 and 3. The additional increase in reflectance observed in Pulses 2 and 3, labeled W, can be attributed to reversible effects due to local temperature increases. Note that at the onset of Pulses 2 and 3, reflectance has reverted to point Q meaning that reflectance change W subsided between pulses. These findings are further bolstered by [78] who also found both reversible and non-reversible changes in reflectance with a maximum change in the reflectance of human skin of 58±7% and in human aorta of 7±2%. The significance of dynamic changes in the reflectance of tissue are, therefore, dependent on exposure time and irradiance as demonstrated in Nishioka's findings as well as tissue type as demonstrated in Lin's findings. Reflectance can also vary with the hydration state of tissue however these changes are less significant than temperature induced changes and generally result in a decrease in reflectance [80].

Due to the gaussian nature of focused laser beams, there exists an increasing energy gradient from the outer edge of the beam to the center which results in a temperature gradient at the surface of the tissue. Since the refractive indices of materials are dependent on temperature, the resulting

31

temperature gradient results in a refractive index gradient at the tissue surface and thus a "lens". This concept known as thermal lensing has certain implications for both imaging techniques which employ lasers (e.g. OCT) and soft tissue coagulation [81]. The lens created at the surface of the tissue can alter the beam profile in the tissue resulting in several artifacts that can interfere with crucial parameters in soft tissue ablation modeling such as penetration depth and scattering properties. The characteristic time for the formation of a thermal lens is given by:

$$t_{lens} = \frac{\omega_o{}^2}{4k/\rho c_p} \tag{17}$$

where k is the thermal conductivity, ω_o is the beam waste radius, ρ is the density, and c_p is the specific heat capacity [81]. For a gaussian beam with $w_o = 103$ µm irradiating vascular tissue ($\rho = 1102$ kg/m^3, c = 3306 J/kgK, K = 0.476 W/m K) the characteristic time for thermal lensing is 20 ms. In imaging applications such as OCT, the beam dwell time is usually far less than t_c and thus thermal lensing does not tend to be significant [81]. In the energy sealing of vessels, the beam dwell time tends to exceed t_{lens} however, given the extremely shallow penetration depth, the lens would result in a refocusing of light no deeper than a few hundred microns and at a very insignificant power level.

2.4 Optical Coherence Tomography

Optical Coherence Tomography (OCT) is an imaging modality which employs a Michelson interferometer to generate depth resolved images. The basic Michelson interferometer consists of a source, a beam splitter, a reference arm, and a sample arm. If the reference and sample arm lengths are matched to within the coherence length of the light source, then interference is generated. The coherence length is simply a derivative of the temporal coherence of the source given that the speed of light is fixed for some medium. In time-domain OCT systems interference patterns are obtained at varying depths by shifting the position of the reference mirror. In spectral domain OCT (SDOCT) systems, depth resolved information can be obtained at a single reference mirror position using a spectrometer. In this work SDOCT is used and thus time domain OCT will not be discussed further. The spectrometer consists of a diffraction grating and line scan camera and thus acquires the spectral density of the interfered beam. Figure 2.10 shows a system diagram for an SDOCT system.
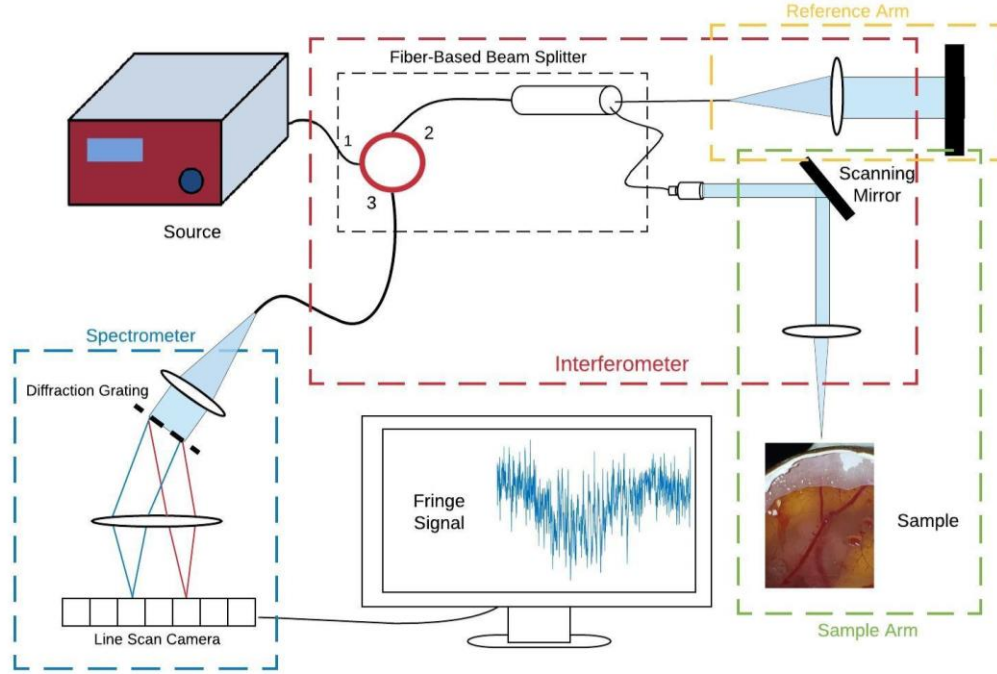
Figure 2.10 SDOCT system diagram. The fiber-based Michelson interferometer is given in the dashed red box. The dashed blue box represents the spectrometer. An example fringe signal can be seen in the monitor. The scanning mirror is used to sweep the beam across the sample and generate B-Scans.

The acquired signal at the camera, termed a fringe signal, can be represented by the following equation:

$$I(\omega) = K\,S(\omega) + K\,Re\{S(\omega)H(\omega)\} \tag{18}$$

where S(ω) is the spectrum of the light source, H(ω) is the spectral response of the sample, and K is a coefficient accounting for the splitting ratio of the beam splitter [82]. On the right side of Eq. 18 the first term represents the DC component of the interference signal. In OCT systems the DC component can be observed by blocking one of the arms and observing the fringe signal. Thus, the DC component does not contribute any useful information to the overall fringe signal. It is often removed in software by subtracting the mean intensity from the overall fringe pattern. Depth resolved information is then obtained by performing a fast Fourier transform on the resulting fringe signal:

$$i(t) = FFT(K\,Re\{S(\omega)H(\omega)\}) \tag{19}$$

where i(t) is termed an A-line [82]. For gaussian sources, the axial resolution of an A-line is equal to the coherence length of the source. Therefore, the axial resolution of an OCT system is given by:

$$l_c = \frac{0.44 * \lambda_o^2}{n * \Delta\lambda} \tag{20}$$

where n is the refractive index of the material, λ_o is the central wavelength of the source, $\Delta\lambda$ is the spectral bandwidth of the source at full-width half-maximum (FWHM) [83]. The lateral resolution of an A-line is equal to the minimum spot size at the sample and is often approximated by the following equation:

$$2\omega_o = \frac{4\lambda_o f}{2\pi\omega_c} \tag{21}$$

where $2w_0$ is the diameter of the spot at the sample (lateral resolution), f is the focal length, and ω_c is the radius of the collimated beam at the focal lens [84]. By sweeping the sample arm beam over the sample multiple adjacent A-lines can be acquired. Then, by vertically concatenating multiple A-lines a two-dimensional image can be formed termed a B-Scan.

The discussion so far has outlined the acquisition of structural images however it is also possible to acquire velocity related information by observing phase shift between successive A-lines. This phase-based OCT modality is termed Doppler Optical Coherence Tomography (DOCT). Phase related information is encoded into the complex portion of the interference pattern thus equation 2.19 must be amended to include the entirety of the interference signal:

$$i(t) = FFT\big(K\,S(\omega)H(\omega)\big) \tag{22}$$

Given an A-line acquired at lateral position x and an adjacent A-line acquired at lateral position x+1, the phase shift can be obtained with the following equation:

$$\Delta\phi = \arctan\left(\frac{\text{Im}\{i(t)_x(i(t)_{x+1})^*\}}{\text{Re}\{i(t)_x(i(t)_{x+1})^*\}}\right) \tag{23}$$

In this work the primary concern is the presence or absence of flow thus the velocity magnitude is not of concern. The velocity resolution of an OCT system is dependent upon the minimum detectable phase shift. The minimum detectable phase shift is determined by the phase noise floor which can be measured by acquiring a Doppler image of a static sample. Once the minimum detectable phase shift is measured the velocity resolution can be obtained from:

$$V = \frac{\lambda_o\Delta\varphi}{4\pi\Delta t\cos\theta} \tag{24}$$

where V is the velocity resolution, $\Delta\varphi$ is the minimum detectable phase shift, Δt is the A-line interval, θ is the doppler angle (taken to be 180° for velocity resolution), and λ_0 is the central wavelength of the OCT system.

Chapter 3: An Integrated Thulium Fiber Laser and Optical Coherence Tomography System

This chapter will outline the various hardware and software components that together form the final system used for the sealing of vessels and their evaluation. At a high level the system is composed of a Thulium fiber laser and an OCT system and as such has been nicknamed Thuli. Thuli, in essence, was engineered to observe the effects of the Thulium laser in tissue. Therefore, it was designed such that laser parameters, such as exposure time, spot size, and average power, could be controlled while simultaneously acquiring micron resolution images. In this work, it was used to observe the effects of Thulium laser irradiation on blood vessels. By integrating both devices into a single system, the overall process of studying tissue response to laser irradiation was streamlined. Thuli was used for all experiments conducted in this work and, therefore, a separate chapter has been dedicated to its development.

3.1 Thulium Fiber Laser Hardware Description

The Thulium fiber laser that was used in this work was constructed by a predecessor. Details concerning the output characteristics and overall behaviour of this laser can be found in [17]. Here an overall description of the laser's components will be given followed by the contributions to the laser hardware made by the author. Referring to Figure 3.1, the laser features two 793 nm diodes which pump a ~2.8 m linear fiber cavity bounded by a high reflectivity FBG (HRFBG) and an output coupler FBG (OCFBG) producing light at 1942 nm. The 793 nm diode lasers were electrically powered by a DEI Scientific PCX-7420 current supply which allowed for laser output power control. The exact model number of the diode lasers has been lost. The FBG's were inscribed into the core of FUD 4070 passive fiber by a lab technician (Jiun) using an excimer laser and UV masking. Spectroscopic properties of the HRFBG and OCFBG are given in Figure 3.2. The diode lasers are coupled to the cavity via a passive fiber Nuferns FUD 4070. A 3to1 fiber combiner was used to couple both diode lasers and to have an additional port for cavity testing. The gain fiber consists of a piece of Nuferns SM-TDF-10P/130-HE double clad Thulium doped fiber. Cavity output of the laser passes through a cladding mode stripper (CMS) to remove any residual cladding modes. The output was coupled via APC connecter to a THORLABS F028APC-2000 fiber collimation package.
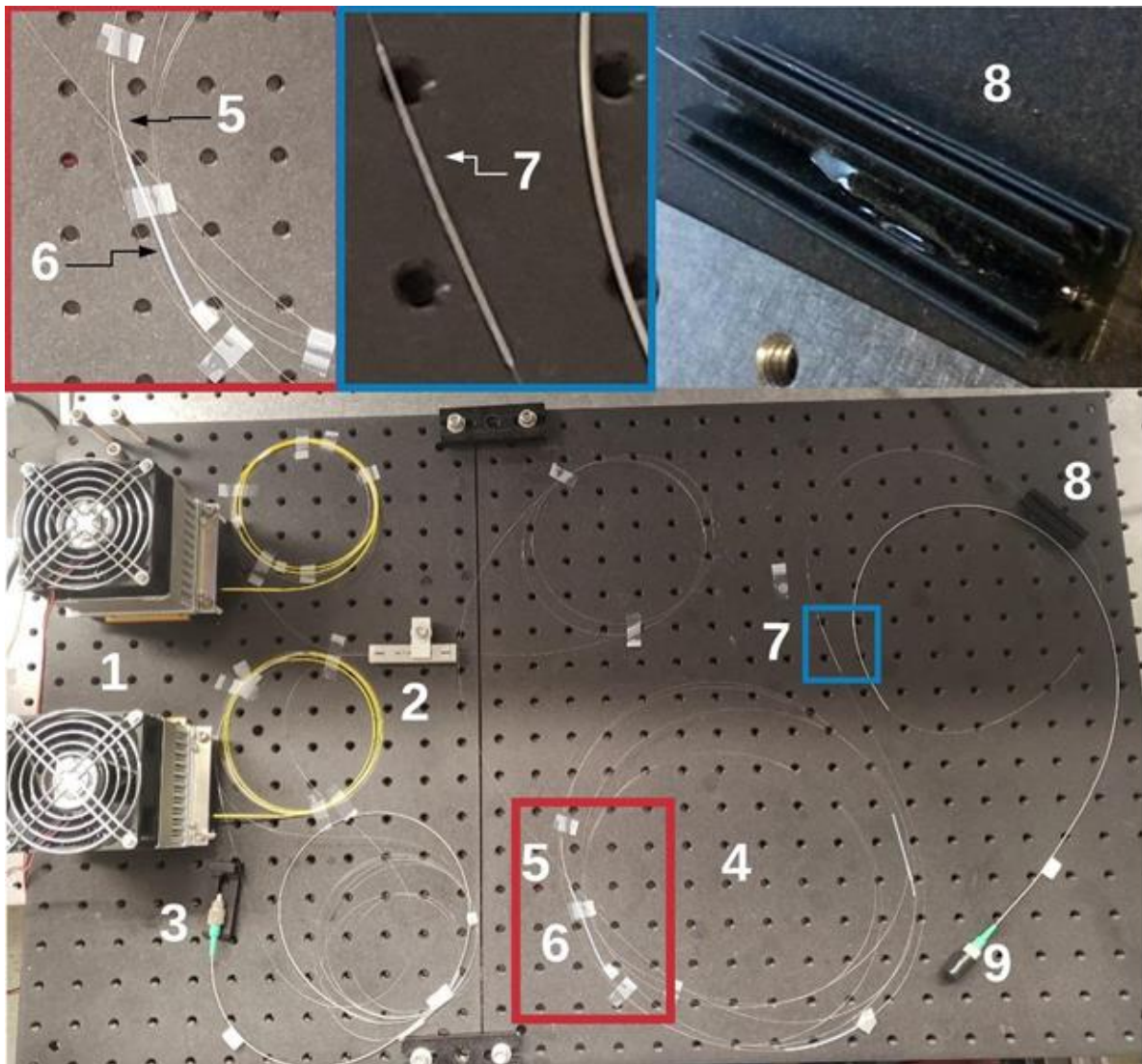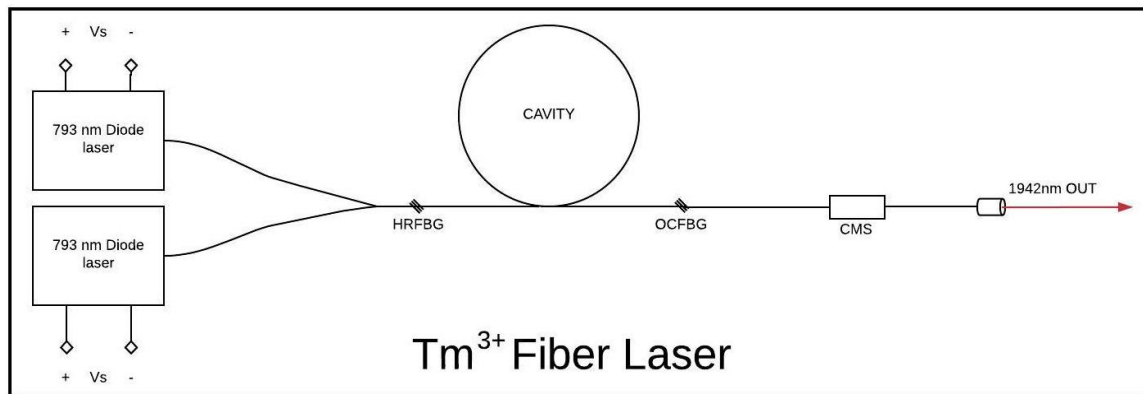
Figure 3.1 Thulium fiber laser layout diagram for clarity (above). Photo of fiber laser (below). 1: 793 nm diode lasers, 2: 3-to-1 coupler, 3: cavity testing port, 4: laser cavity, 5: HRFBG, 6: burning point, 7: OCFBG, 8: CMS, and 9: 1942 nm output.
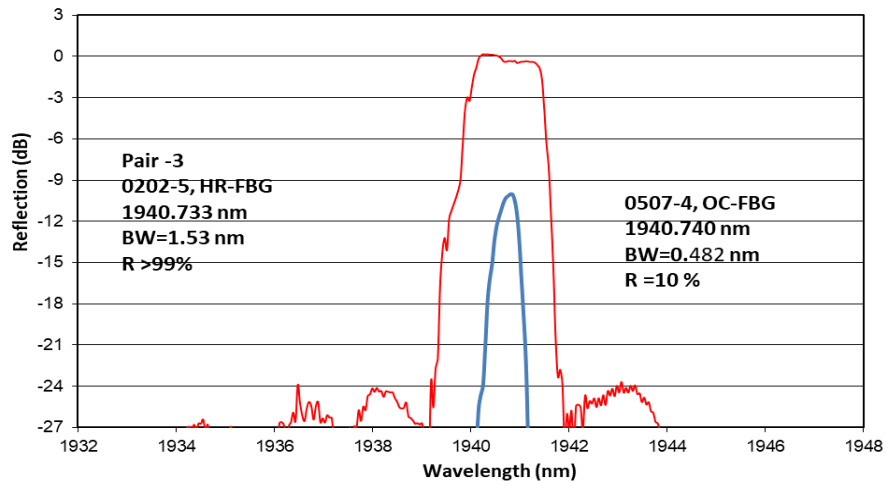
Figure 3.2 HRFBG and OCFBG Spectral Reflectivity.

3.1.1 Laser Hardware Contributions

After prolonged operation, the testing port of the fiber cavity (labeled as "3" inf Figure 3.1) was found to have burned. Since the HRFBG allows only a small fraction of 1942 nm light to exit the cavity towards the diodes (see Figure 3.2), it was suspected that this was a result of residual cladding modes back propagating out of the cavity meaning that the CMS was not performing as expected. Upon inspection it was found that a portion of the optical epoxy used to create the CMS had been singed and thus it was clear that it could not handle the power levels at which the laser was operating. Additionally, the V number calculated for the active fiber of the Tm fiber laser used in this work is slightly higher than the cutoff for single mode operation at 2.42 (see Eq. 2.4). To repair this issue, the CMS had to be replaced and upgraded. To do this, a graded CMS was created and installed. A typical CMS uses a single optical epoxy with refractive index greater than the first cladding to encourage cladding modes to escape. The issue with this being that most of the light tends to escape in the first few millimeters of the CMS causing localized heat accumulation and thus burn. A graded CMS uses several optical epoxies of increasing refractive index to allow for gradual stripping of cladding modes. This ensures that heat accumulation as a result of escaping modes is evenly distributed along the length of the CMS and not focused on a single point [85]. To create the graded CMS the outer cladding of a FUD-4070 fiber was first stripped. The stripped fiber was then set into a heat sink where three different optical epoxies were then laid in segments over the fiber such that the stripped fiber was completely enveloped by the epoxies. The refractive index of the first cladding of FUD-4070 is 1.4537 therefore optical epoxies

38

with refractive indices 1.48, 1.50, and 1.51 were used to facilitate graded cladding mode stripping. A schematic of the graded cladding mode stripper is given in Figure 3.3.
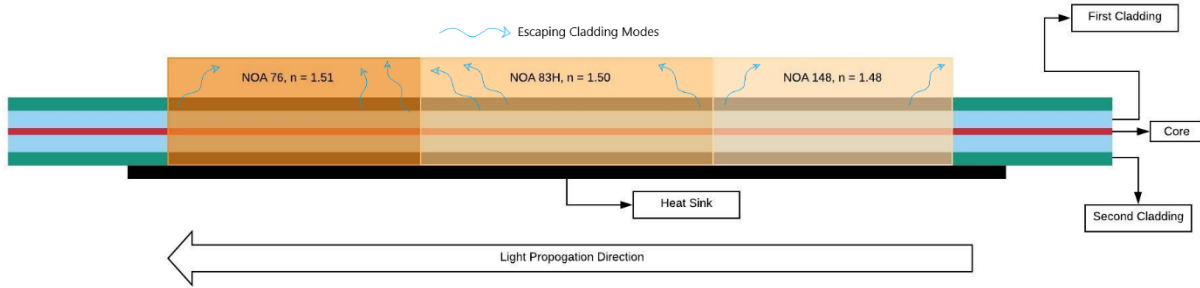
Figure 3.3 Graded CMS. Optical epoxies were laid with increasing refractive index to evenly distribute escaping energy and avoid localized heating. Epoxies used were NOA 148, NOA 83H, and NOA 76.

3.2 OCT System

OCT imaging was accomplished using a spectral-domain OCT system with a supercontinuum (SC) source (SuperK Extreme from NKT Photonics) centered at 1280 nm. In this work the beam was set between 13% and 20% of the SC source depending on the sample being imaged. Output of the SC source is passed through a Gaussian filter (SuperK Gauss by NKT Photonics) to produce the final output spectrum seen in Figure 3.4.
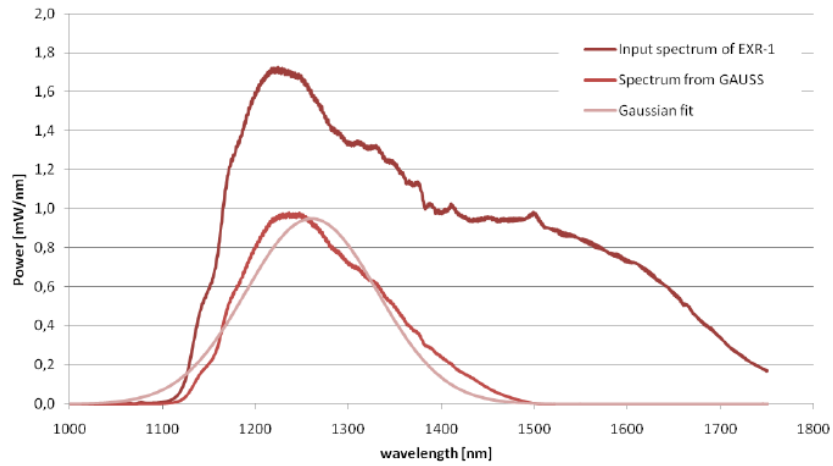
Figure 3.4 Output spectrum of the SC source (EXR-1) and spectrum after passing through gaussian filter (Spectrum from GAUSS). This is the effective spectrum used for OCT imaging in this work.

The fiber-based Michelson interferometer consists of a THORLABS CIR-1310-50-APC circulator and a THORLABS TW1300R5A1 beam-splitter to maintain the wide bandwidth of the SC source. It also includes a 3-paddle polarization controller to facilitate polarization rotation. An iris clamp situated in the reference arm was used to facilitate power balancing between the reference and

39

sample arms. Since each tissue type offers different reflective characteristics, power balancing was performed at the onset of any tissue imaging procedure. Figure 3.5 shows an image of the interferometer.
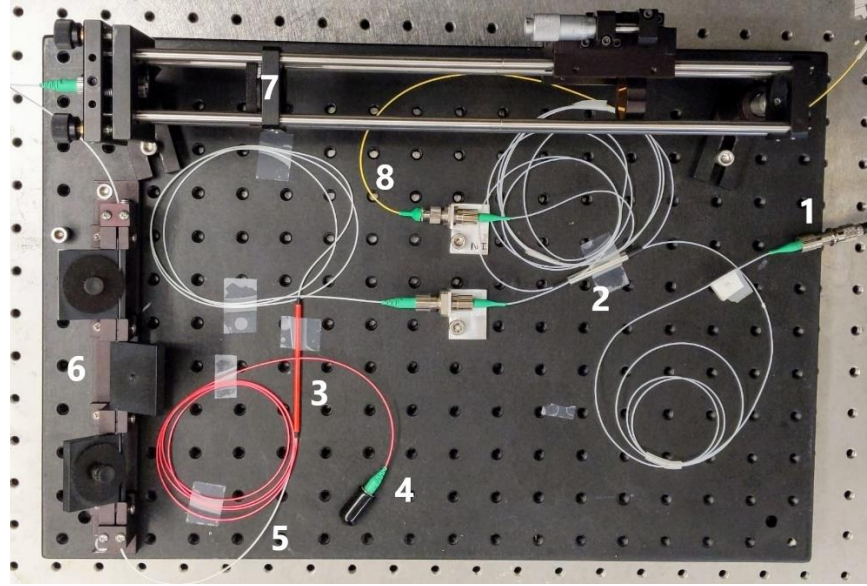
Figure 3.5 Interferometer. 1: SuperK Gauss output/interferometer input, 2: circulator, 3: beam splitter, 4: sample arm, 5: reference arm input, 6: polarization controller, 7: iris clamp, and 8: interferometer output/spectrometer input.

The interference signal was acquired using a custom spectrometer from P&P Optica which has a grating frequency of 892 lines/mm, a spectral resolution of 0.365 nm, and a wavelength range of 1190-1370 nm. The axial resolution of the system was obtained using Eq. 2.20 and was found to be 6 μm in tissue. The camera of the spectrometer (Goodrich LDH2) contains an array of 1024 sensors being sampled at 10813 Hz (A-line rate) although can reach sampling rates of 91911 Hz. The bandwidth of the LDH2 is 0.8-1.7 um making it suitable for the source used in this system. The velocity resolution of the OCT Doppler system was found to be 112 µm/s using Eq. 2.24. This value was calculated using the minimum detectable phase shift corresponding to an SNR of 25. More details are available in [86].

3.3 Integrating Tm^{3+} Fiber Laser and OCT System

The sample arm output of the interferometer is collimated using the THORLABS F260APC-C collimation package before passing through the GVS002 galvonometer system for sweeping. For the rest of this work "galvonometer" will be abbreviated to "galvo". The beam was swept in one dimension over a distance (at the sample) of 6.2 mm. This was done for the purposes of acquiring B-mode images. A short-pass dichroic mirror (THORLABS DMSP1500) is used to couple the

collimated 1942 and 1280 nm beams. The mirror is fixed at exactly 45° relative to the beam using the THORLABS C3P60R to ensure expected performance. After passing through the dichroic mirror, the coupled beam is focused using a CaF$_2$ lens (f = 100 mm). Using a beam profiler, the resulting spot size at focus of the OCT beam was found to be ~70 µm. At 6.2 mm lateral beam sweep and 1024 A-lines per sweep this ensured sufficient overlap for the acquisition of Doppler signals. Profilers in the 2 µm regime are extremely costly thus spot size of the 1942 nm beam was approximated theoretically using Eq. 2.21. The parameter ω_c was taken to be the diameter of the 1942 nm collimated beam which according to the F028APC-2000 data sheet was 1.2 mm while the focal length f was 10 cm. With these parameters the minimum spot size at the sample was approximated to 206 µm.
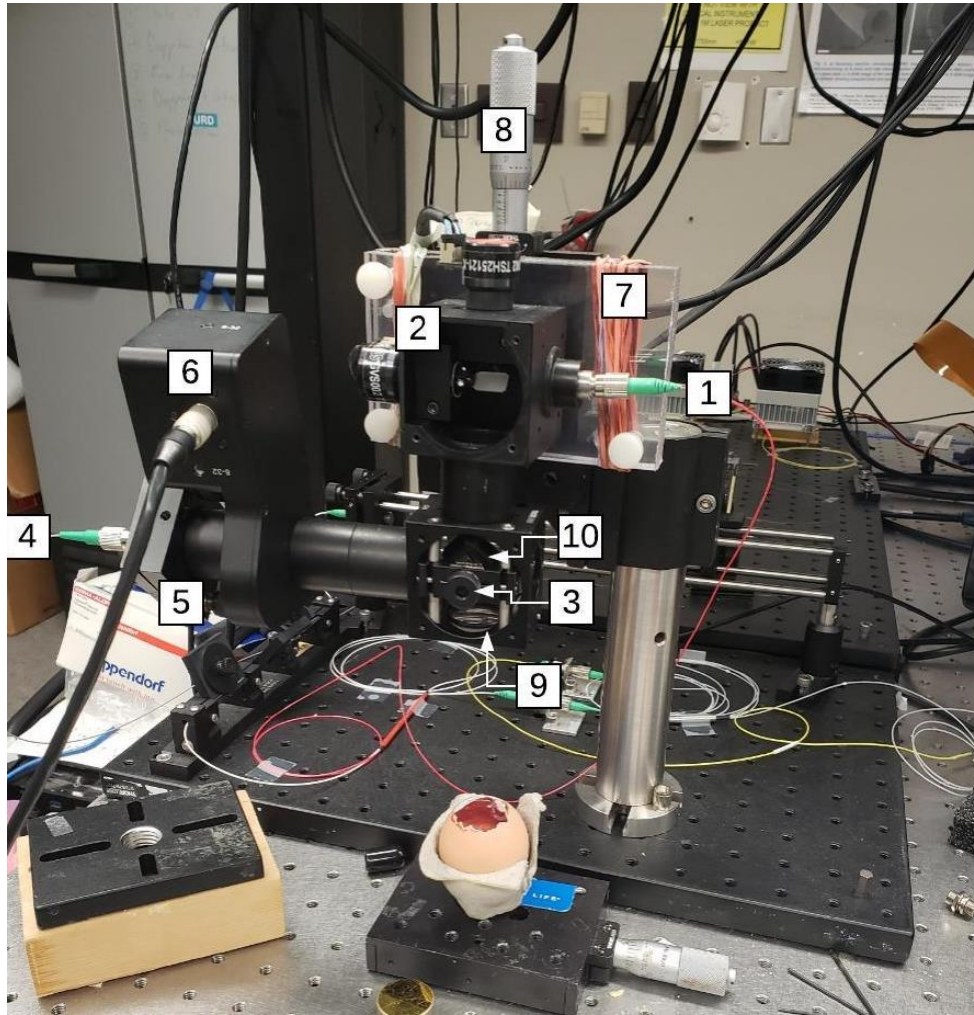
Figure 3.6 Optical payload. **1**: 1280 nm beam input, **2**: Galvonometer, **3**: C3P60R, **4**: 1942 nm beam input, **5**: yaw-pitch stage for 1942 nm beam, **6**: SH1, **7**: Pitch-yaw stage for entire optical payload, **8**: Vertical translation stage, **9**: focusing lens, and **10**: DMSP1500.

The entire optical payload, consisting of both high-power laser optics and OCT optics (Figure 3.6), is mounted onto a linear translation stage and a custom-built pitch and yaw stage, which was necessary due to the high angular sensitivity of the dichroic mirror. Spot size was varied by displacing the beam out of focus along the optical axis by a set distance using the linear stage. The spot size at a given displacement was determined theoretically assuming an M^2 factor of 1. Exposure time was regulated using a THORLABS SC1 shutter controller and an SH1 single blade shutter which was placed between the 1942 nm collimator and the dichroic mirror. The final system diagram is given in Figure
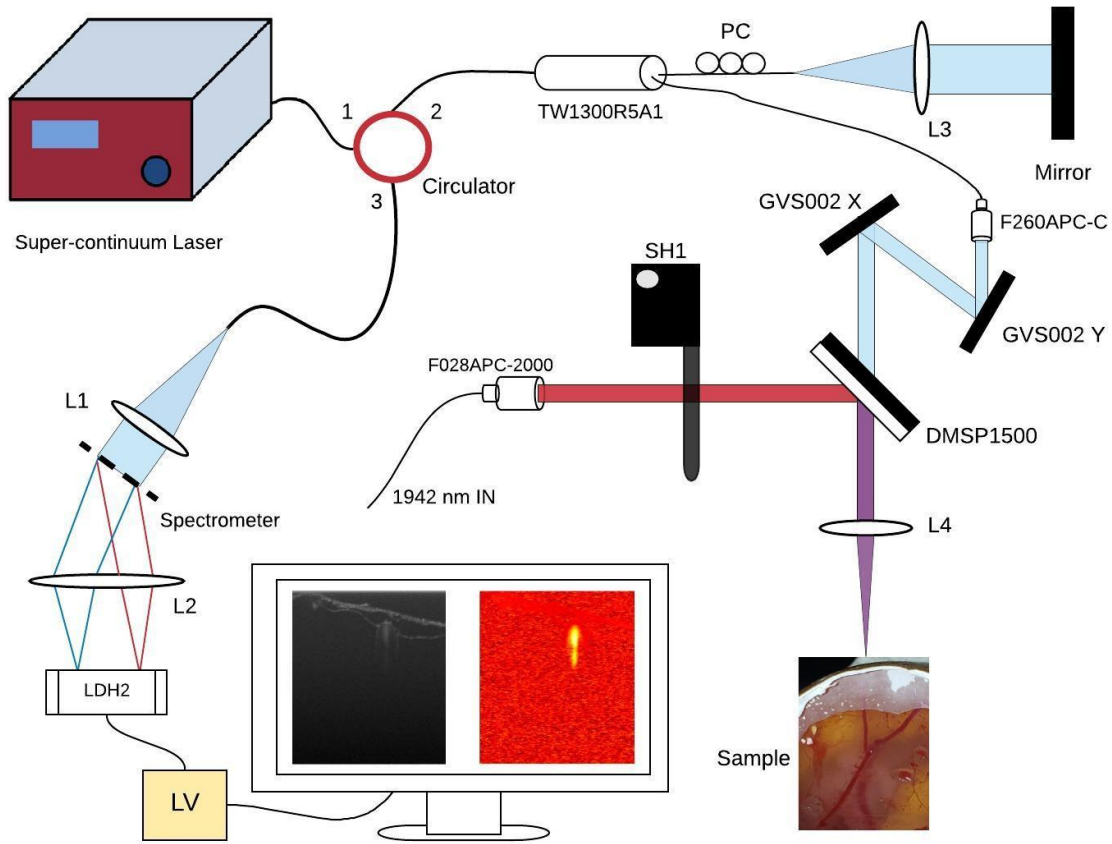
Figure 3.7 Overall system diagram excluding fiber laser components.

3.3.1 System Integration Considerations

Several challenges are presented when integrating a high-powered laser with an imaging laser. The two systems are drastically different in functionality and intended purpose and as such finding compatible optics for the two can be problematic. Referring to Figure 3.6, it can be seen that both

beams are coupled using a dichroic mirror (DCM) labeled "10". Both the size and shape of the DCM had to be considered given that the imaging beam had to be swept and that the mirror had to be integrated into existing optics (for economical purposes). The DMSP1500 was chosen as it was the largest circular dichroic mirror in the required spectrum and, thus, allowed for the greatest range of beam sweeping while being compatible with existing optics. Since the imaging beam passes through the DCM twice (to the sample and back), the DCM had to be extremely efficient in power transmission. According to Figure 3.8 the power loss associated with a single pass through the mirror is approximately 2.5%, meaning that the overall power loss with two passes is 5% which is acceptable given that the power level of the SC source can be increased by that amount to compensate.
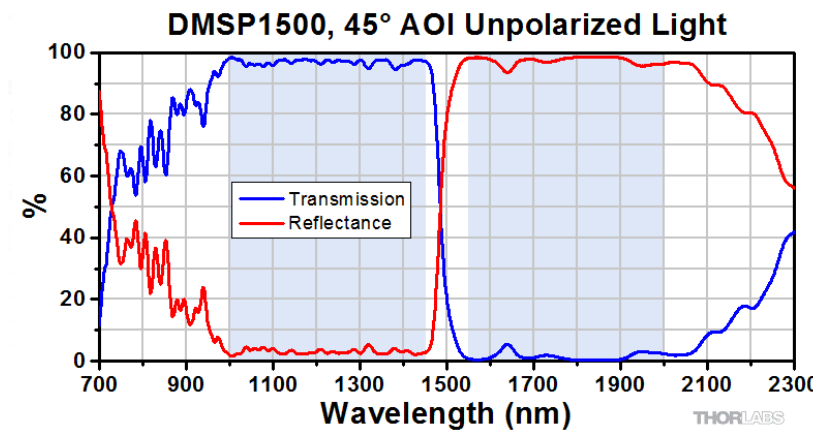
Figure 3.8 Transmission/reflection characteristics of the DMSP1500 by Thorlabs.

The high angular sensitivity of the dichroic mirror posed a problem. While ensuring that the mirror was fixed at exactly 45˚ relative to the beam was simple using the C3P60R (labeled "3" in Figure 3.6), it was difficult to ensure that the entire optical payload was level with the sample surface. This was important as the reflected portion of the beam returning to the mirror would be greatly attenuated if it did not encounter the DCM at the correct angle (Figure 3.9A). The issue of the reflected beam was discovered during a system calibration where a loss in fringe signal amplitude was observed when the DCM was installed. The amplitude loss was too great to be solely attributable to the DCM's inherent transmission attenuation. In order to level the payload with respect to the sample surface, a pitch and yaw stage was necessary. Typical optical pitch and yaw stages are costly, as a result a stage was custom built using three thumbscrews, two acrylic plates, and several elastics (labeled "7" in Figure 3.6). Turning the thumbscrews allowed for micro

adjustment of the pitch and yaw of the payload. Since numerical feedback was not possible with this primitive stage, pitch and yaw were optimized by sweeping each screw from highest extension to lowest extension and determining the point which generated the greatest amplitude in the fringe signal. This optimization methodology is commonly implemented in optics, most notably for polarization matching in 3-paddle polarization controllers.
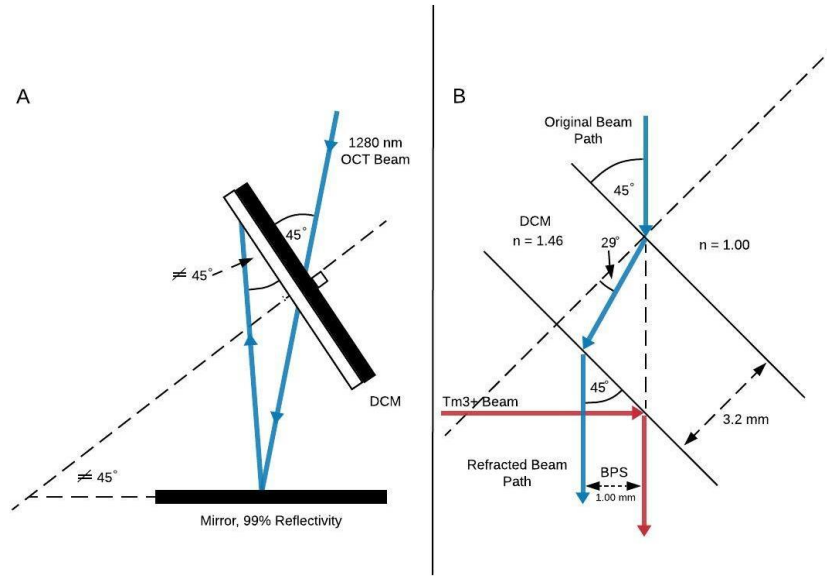
Figure 3.9: The DCM problems. A: The issue of the returning beam. Even with the DCM being fixed at exactly 45° relative to the incident beam, the reflected beam may still encounter the mirror at an angle other than 45° if the entire optical payload is not level with the surface. Note that the degree of payload inclination here is exaggerated for demonstration, in reality the degree of misalignment was less than 5 degrees. B: An illustration of the Beam Path Shift (BPS) experienced by the imaging beam. Note that the imaging beam is refracted while the Thulium beam is not, resulting in the BPS.

Given that the DMSP1500 is a shortpass DCM (i.e. transmits the shorter wavelength and reflects the longer wavelength), the high-powered beam experiences reflection while the imaging beam experiences refraction. The resulting effect is that there is an overall beam path shift experienced by the imaging beam and not by the high-powered beam. This phenomenon is illustrated in Figure 3.9B. The total beam path shift experienced by the imaging beam was 1 mm which is significant in this context given that real-time structural image feedback was used to target arteries as small as 0.1 mm in diameter. To account for the beam path shift experienced by the imaging beam, the collimating lens of the high-powered beam was placed into a pitch and yaw stage (labeled "5" in Figure 3.6). In doing so, it was possible to use adjustment knobs to offset the high-powered beam and align it with the imaging beam.

Referring to Figure 3.6, it can be seen that both the imaging beam and the high-powered beam are focused by the same lens (labeled "9"). This also posed a significant design challenge. On one hand, it is desirable to have a tightly focused beam to maximize lateral resolution of the OCT system. On the other hand, too small of a spot is undesirable in energy sealing given that a spot size much smaller than the diameter of a vessel would result in an uneven thermal energy distribution, potentially resulting in rupture. Additionally, since the system would be used on biological samples and the high-powered laser is strongly absorbed in water, great care had to be taken to ensure that sufficient distance existed between the sample and the focusing lens. This is important because if any splash back or condensation resulted in water accumulation on the focusing lens it could burn, permanently damaging it. Thus, a lens with a 100 mm focal length was chosen ensuring enough distance was kept between focusing lens and sample. With the focal length fixed at 100 mm only the spot size of the collimated beams at the focusing lens could be adjusted to regulate the spot sizes of each of the beams at the sample (Eq. 2.21). Given this, and due to the limited selection of FC-APC collimating packages available in the 2 µm range, the F028-APC collimation package by Thorlabs was selected with a collimated spot size of 1.2 mm. The relatively small spot size of the collimated beam ensured that the beam will not be tightly focused. As for the imaging beam, the F260APC-C collimation package was chosen with a collimated spot size of 2.8 mm. This resulted in the imaging beam being more tightly focused than the high-powered beam achieving improved lateral resolution.

Both the high-powered and imaging beams were invisible, meaning that aligning the two was challenging. Bulk alignment between the beams was achieved by temporarily passing red laser through the optical payload. However, the F028-APC collimating lens does not allow visible light to pass through it, and as a result it had to be swapped out during alignment. While this method served for bulk alignment, it was not suitable for micro alignment which was necessary given the scale on which OCT operates. Additionally, swapping between collimating lenses during bulk alignment jeopardized the positioning of the lens causing further misalignment. Thus, after bulk alignment was achieved a methodology was developed where a crater would be ablated into moistened cardboard (moistening the cardboard ensured that absorption would be maximized). Then, by using structural image feedback it would be possible to determine the position of the high-powered beam relative to the imaging beam based on the position of the crater. The resultant crater would typically be quite sharp allowing for a well-defined marker of high-powered beam

position relative to imaging beam. By using the position of the crater, the pitch and yaw stage of the high-powered beam ("5" in Figure 3.6) could be adjusted appropriately to ensure that the crater would be central with respect to the imaging field, thereby microscopically aligning the beams.

3.4 Control and OCT Processing

Control signals were generated by the NI PCIe-6351 card while image acquisition was facilitated by the NI PCIe-1427 card. For the acquisition of B-mode images the LDH2 acquisition period had to be synchronized to the sweep of the galvo. For this purpose, a hard trigger signal was sent to the LDH2 from the NI PCIe-6351 card. The square wave pulse was synchronized to the galvo control signal such that acquisition occurred on the primary sweep of the galvo and ceased during the return sweep. These signals are depicted in Figure 3.10. The galvo sweep was set according to the expected size of vessels. From preliminary experiments, it was found that vessel diameters would not exceed 3mm and as a result the sweep range at the sample was chosen to be ~6 mm such that the full breadth of any expected vessel could be captured. The galvo sweep range at the sample was controlled by the amplitude of the galvo control signal. By default, the GVS002 system sweeps $0.8°/V$ where 0 V is the galvo 0 position. Thus, by applying simple trigonometry, the galvo control signal amplitude was set to 1.15 volts corresponding to a sweep range of $\pm\,0.93°$. It was crucial to ensure that the full sweep range of the beam at the sample was short enough to allow for sufficient beam overlap such that Doppler signals could be acquired.
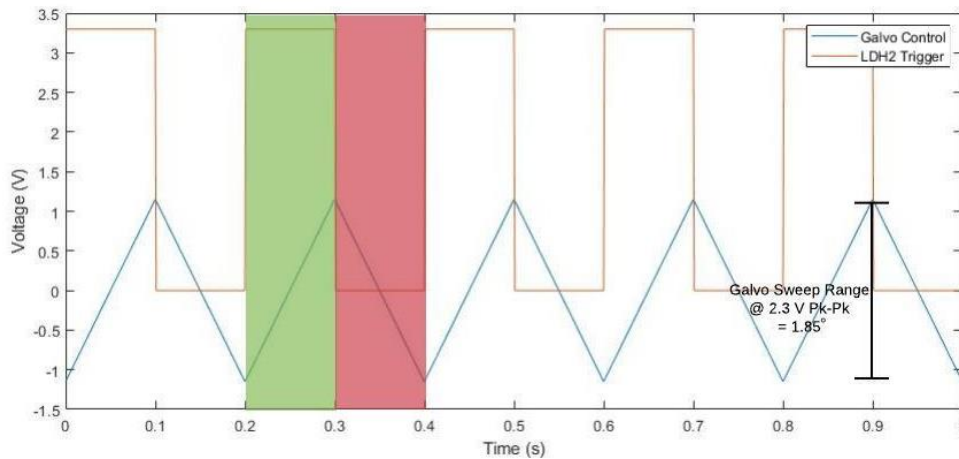
Figure 3.10: Galvo control signal and LDH2 trigger. This figure depicts five acquisition cycles. The green zone represents the primary sweep of the galvo and LDH2 acquisition period. The red zone represents the return sweep of the galvo and LDH2 standby.

Given that 1081 A-lines were acquired in every acquisition cycle (acquisition period = 0.1 s and A-line rate 10813 Hz) and that the imaging beam spot size was 70 µm, no overlap would occur if the sweep range at the sample was 75.67 mm or greater. With the selected sweep range at the sample being ~6 mm the beam overlap ratio is 12.6 meaning that, with the exclusion of the extremes, every point along the sweep path would be imaged by 12.6 A-lines which is more than sufficient for the acquisition of Doppler signals. Note that although 1081 A-lines were acquired in every acquisition period only 1000 were used to generate a B-Scan, the extra A-lines at the extremes were excluded.

For a single data point ~100 B-Scans were acquired. Real time processing and display of B-Scans was necessary in order to facilitate real time vessel targeting. To minimize the processing load only a single B-Scan was displayed at a given time at a frame rate of approximately 1.2 B-Scans/s. LabView was used for real time processing and display of the images. The sampled signal was processed using a LabVIEW VI through the steps of resampling, FFT, dispersion compensation, and log compression for display. The LabVIEW VI was constructed by a colleague and this is not discussed further. Due to the data intensive nature of each data point, final processing was done in MATLAB after each experiment was completed. An entire dataset consisted of 20-55 data points. Data sets were labeled according to the appropriate trial, where the first trial included in this work was eggTrial11. A total of 4 data sets were included in this work including eggTrial11. The MATLAB code used for processing eggTrial11 is given in the Appendix. Specific lines of the code will be referenced in the remainder of this section using parentheses. An entire data set was processed in a single .m file where each iteration processed pre and post images separately and finally grouped them for display. In order to generate both structural and Doppler images, it was necessary to define a set of constants:

1. The function representing wavelength to pixel number termed 'la'. This function is specific to the spectrometer and is given in the operation manual (17).
2. Since the Fourier Transform requires information represented in terms of frequency or wavenumber, la was converted into K-Space generating the function k0 (18). This process results in unevenly spaced wavenumbers. The K-Space representation of la was then linearized to generate evenly spaced query points for interpolation. The final K-Space function is given as 'k' (27-29).

With these two functions defined general OCT processing commenced. Each A-line was processed independently. A-Line processing was conducted according to the following steps:

1. DC Subtraction. The mean intensity of the A-line is subtracted from all pixel intensities (56-57).
2. Liner interpolation. Using the k function as a set of query points, the function representing intensity in terms of wavenumber was linearly interpolated to produce an evenly spaced set of intensities in K-Space (58-61).
3. Fourier Transform (63).

After these initial processing steps, A-lines were vertically concatenated to form B-Scans. B-Scans were then stacked into a single array termed cdata. Note that this array does not represent a true C-Scan since all B-Scans were acquired in the same cross section. The cdata array was first processed to generate the Doppler image according to the following steps:

1. A-line conjugate multiplication (74-75).
2. A-line averaging. Significant overlap of A-lines allowed for the averaging of adjacent A-lines. A moving average was used with width of 20. This was the first step of speckle noise reduction (80).
3. Phase angle extraction according to Eq. 2.23 (83).
4. B-Scan averaging. Approximately 100 B-Scans were averaged into a single image. This is the most efficient method for the reduction of speckle noise. Additionally, this ensured that motion artifacts due to cardiac cycles would be filtered out given that, at 6 B-Scans/s, this represents averaging over a ~17 second period (87). See Section 4.1.2.

Processing of the structural data set was less intensive where only step 4 above was conducted to the absolute value of the Fourier transform result (90 and 92).

3.5 System Calibration and Validation

Many of the systems components were reused from older systems belonging to predecessors meaning that many of these components suffered from wear and tear. The linear stage used to augment spot size did not travel perfectly straight and the galvo of the GVS002 exhibited drift due to a worn rubber compression fitting. Incidentally, system calibration was performed periodically to ensure optimal performance. System calibration was performed in the following steps:

1. The system was placed into M-mode, galvos were zeroed and a mirror was used at the sample. The mirror could not be perfectly perpendicular to the beam as it would saturate the LDH2 and thus was offset by setting it on a piece of card.

2. The DCM was removed from the system.

3. The reference arm of the interferometer was blocked, and the average power level of the fringe signal was noted. This represented the power level of the sample arm. The reference arm was then unblocked, and the sample arm was blocked such that the average power of the reference arm was displayed. The average power of the reference arm was made to match the average power of the sample arm using the iris clamp (labeled "7" in Figure 3.5). This is the initial power balancing step.

4. Assuming that the length of the reference and sample arm had already been roughly matched, the linear translation stage was then jogged until the mirror surface was clearly visible in the real-time structural image feedback. The linear stage was then swept such that the mirror surface was kept within the range of the image to determine the point at which the power of the fringe signal was maximized. Once this point was determined both the length of the reference arm and sample arm were adjusted to bring the focus of the beam just below the surface. This is a strategy used in OCT imaging of tissue.

5. Polarization matching was then facilitated using the three-paddle polarization controller (labeled "6" in Figure 3.5). Each paddle was individually swept between its extremes and held at the point at which the fringe signal amplitude was maximized.

6. The DCM was carefully reinstalled, usually resulting in a loss of fringe signal amplitude (see Section 3.3.1).

7. The knobs of the pitch and yaw stage were adjusted individually. As with the polarization matching step, each knob was swept between its extremes until the fringe signal amplitude was maximized.

8. Beam alignment procedure was carried out as outlined in Section 3.3.1.

9. The mirror was swapped with an actual tissue sample. Step 3 was repeated.

With each of the previous steps properly completed, peak system performance was achieved. A benchmark image was acquired and used to evaluate future system performance. The benchmark image was acquired from an agar phantom. At the onset of any experiment, system performance was evaluated by acquiring a B-mode image of the phantom in the same cross-

section as the benchmark image. Several markers within the image were used to evaluate system performance such as the deepest resolved structure, definition of structures, and structure brightness. The signal to noise ratio was not a valid marker for image quality due to a highly varying speckle noise in the image background. The benchmark image is given in Figure 3.11.
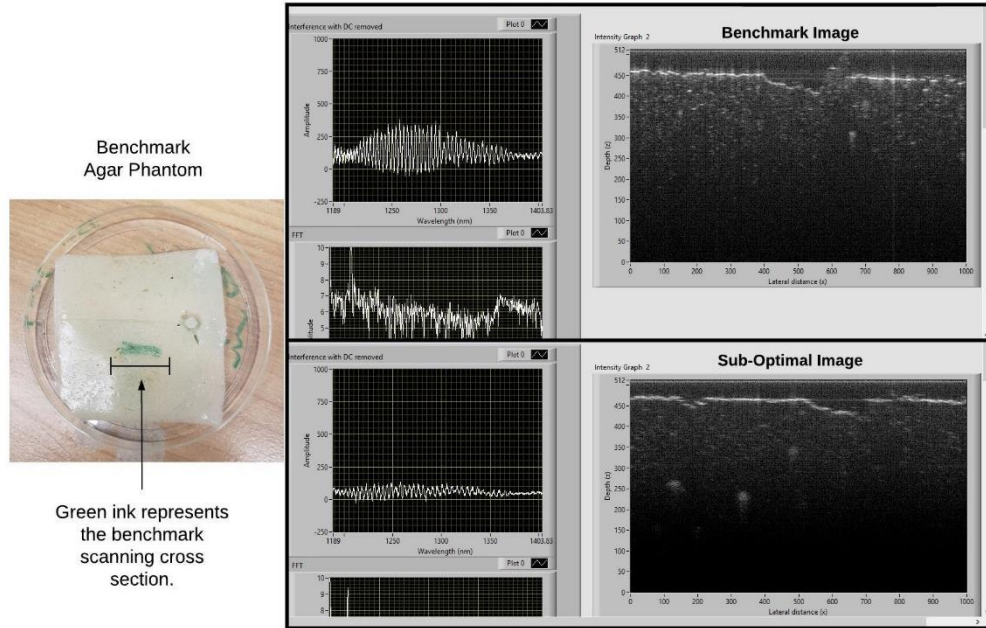
Figure 3.11: System benchmark image and the agar phantom used for acquiring the benchmark image. Observe the differences in fringe signal amplitude between the benchmark image and the sub-optimal image. Also note the definition of structures in the benchmark image versus the sub-optimal image. Note: the x and y axes of the OCT images are incorrectly labeled here, the x-axis should be labeled as "A-line number" and the y-axis should be labeled as "Pixel number".

Doppler functionality of the system was validated by conducting a milk-flow test. Milk of the highest fat content is used as it is the intralipids of the milk which serve as reflecting structures. Using a syringe pump, milk is forced through plastic tubing of 0.5 mm inside diameter at a fixed flow rate. For contrast, the tube was embedded in an agar phantom. Since the agar phantom is stationary no Doppler signal should be associated with it. In this work, the actual velocity of the fluid is irrelevant, the primary concern is the presence or absence of flow. As a result, it was only necessary to prove that Doppler signal existed when there was flow and did not exist when there was no flow. Figure 3.12 shows the results of this process.
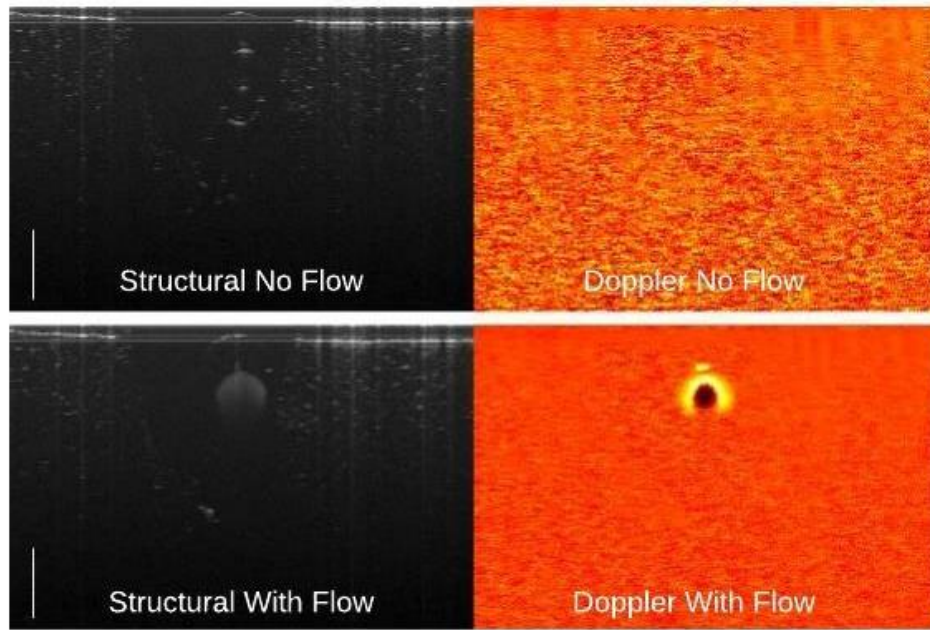
Figure 3.12: Doppler validation results of the milk flow experiment. The inner and outer diameter of the tubing can be seen upon careful examination. Brightness artifacts obscure the upper portion of the tube. Scale bars in the structural image represent 0.5 mm. The Doppler signal is only present when there is flow and thus the system is functioning as expected.

Chapter 4: Developing a Methodology for the Evaluation of Energy Seals Using Optical Coherence Tomography

Laser energy sealing is the process by which a laser is used to occlude a blood vessel. It has numerous applications across multiple surgical sectors including tumour devascularization [87,88], the treatment of various endolaryngeal maladies [89–91], and in the treatment of arteriovenous malformations [92,93]. In all cases, the intent is to mitigate the flow of blood to a body of tissue with minimal collateral damage or simply to achieve hemostasis by ceasing the extravasation of blood. Laser-based systems are an attractive option for the energy sealing of vessels as they offer several advantages over conventional instruments. These include the potential to induce hemostasis in a contactless fashion and the ability to achieve selective tissue interaction with wavelength selection. In the last decade or so, these systems have attracted more attention given the general shift in surgical paradigm towards the use of less invasive surgical instruments and the general ease with which laser light can be conducted through such instruments. Given this, it is paramount to have an objective method with which vessel seals can be evaluated so that the hemostatic capabilities of laser-based systems can be tested. Current methodologies used for this purpose include burst pressure analysis (BPA) [94–96], microscopy [47], and visual examination [97–100]. While BPA yields valuable insight as to the strength of seals, it cannot be performed in situ without invasive measures. Microscopic analysis allows for detailed en face visualization of the irradiation site and is effective in observing the presence of absence of blood flow even in small arteries; however, it relies on an unimpeded view of the vessel which at times is not granted given the development of coagulum and, further, does not yield depth-resolved information. Visual examination is a rapid method and is ideal in non-critical scenarios where complete cessation of blood flow is not necessary. Despite this, it is highly subjective since it is solely based upon what an individual can see with the naked eye making it a poor choice for scientific processes. Additionally, it is impractical for vessels below 1 mm in diameter due to limitations of the human eye.

In this chapter a methodology for the evaluation of laser energy seals will be developed using Doppler Optical Coherence Tomography (DOCT). DOCT imaging features a high sensitivity to flow, typically capable of detecting flows as low as 130 µm/s in tissue [101]. Clinical applications of DOCT include vasoactive drug screening, hemodynamic monitoring following pharmacological

and photodynamic therapy, and mapping cortical hemodynamics [84]. In a study comparing Doppler ultra-sound to CT angiography, the gold standard in vascular flow detection, it was found that Doppler ultrasound correctly detected 50/58 carotid occlusions [102]. Of the 8 false positives (no flow detection when in fact there was flow), 7 were cases of near complete occlusion, and thus, extremely low flow rates, and 1 was a result of an anatomical anomaly where a sharp 90˚ bend of the vessel occurred in the imaging field resulting in failed Doppler signal acquisition. DOCT has two orders greater velocity resolution than Doppler ultrasound [101] and, thus, it is likely to succeed in detecting flows present in near totally occluded vessels. As such, it is reasonable to conclude that DOCT will have a higher sensitivity (i.e. in detecting complete seals) than Doppler ultrasound bringing it closer to the gold standard of CT angiography. The primary limitation of DOCT is its shallow penetration depth which limits the depth at which velocity information can be resolved to a maximum of 3 mm. This means that DOCT, for the purposes of energy seal evaluation, is only viable for small vessels with diameters less than 3 mm. Further, DOCT can only target superficial vessels, vessels that have been surgically exposed, or vessels that have been brought within close proximity of the instrument in laparoscopic/catheter based cases. Despite this, DOCT offers an objective method for evaluating the quality of energy seals, and, given its high velocity resolution is capable of detecting minute flows that are otherwise invisible to the aforementioned methods. Although DOCT does not generate information relating to the strength of energy seals, as with BPA, its potential for rapid in situ assessment of energy seals in small vessels makes it an attractive method for the evaluation of laser sealing systems.

The DOCT methodology will be developed by sealing vessels in avian embryos where the intention is to demonstrate that DOCT can be used objectively to determine whether a vessel has been sealed. To the author's knowledge, there have been no studies which employ DOCT for this purpose. In the literature, several studies exist where a laser's ability to induce complete seals in vessels is evaluated visually [47,73,97]. Therefore, given the nature of this work, it is valuable to compare visual evaluation to DOCT evaluation such that the accuracy of visual methods in evaluating vessel seals can be assessed.

4.1 Methodology

All experiments were carried out according to recommendations provided by the Research Ethics Board of the institution. A total of 80 avian egg embryos were cultivated and appropriately prepared for the experiment which yielded 104 viable vessels. Each vessel was subjected to

Thulium laser irradiation where exposure time, spot size, and average power were varied in order to generate a variety of outcomes. For each vessel, an OCT structural image, OCT Doppler image, and photograph were acquired for both pre and post laser exposure forming a single data point. Pre and post images were examined to evaluate the outcome.

4.1.1 In-Ovo Specimen Cultivation

Avian embryos were used in this study as they offer convenient access to functioning arteries and are a rapid, cost-efficient alternative to other in-vivo models. Eggs were incubated in a custom-built incubator which used temperature feedback control to maintain a constant 38˚C (Figure 4.1). Twenty-four eggs were incubated at a single time and thus sufficient air flow for oxygenation was ensured using a ventilation system which consisted of a fan and tubing. Humidity was maintained by observing the progression of condensation along the length of the ventilation tube. The typical yield was 19/24 eggs.
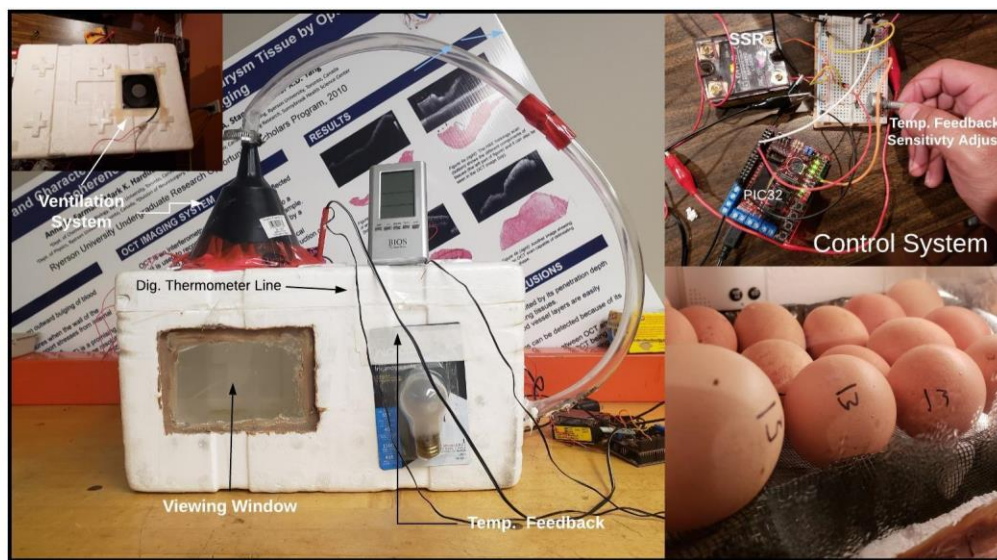
Figure 4.1 Custom built egg incubator. An incandescent light bulb is used to generate heat and is controlled via a PIC32, Solid State Relay (SSR) and a thermistor within the incubator. Temperature is monitored with a digital display. A sealed ventilation system ensures oxygenation.

Access to embryonic arteries was achieved using a method outlined in [98] where the egg shell is breached in the vicinity of the air-pocket as to avoid damaging vital biological structures. Arteries were exposed by delicately peeling away the inner shell membrane from the chorioallantoic membrane (CAM, see Figure 4.2). This process required several trials to master as the slightest mishap could lead to a breach of the CAM typically resulting in profuse bleeding. A strategy was developed where the egg shell was carefully chipped away using tweezers until the

slightest breach in the inner shell membrane was created along the edges of the air-pocket at which time fine-tipped tweezers would be used to make the initial grasp of the inner shell membrane. Once grasped, a second set of tweezers was carefully introduced which allowed for a measured alternating grasp-and-pull technique of the inner shell membrane typically resulting in successful separation. An improvement to this technique suggested in [103] where a small hole is formed in the shell in the vicinity of the air pocket on the third day of development was not found to be useful. Continuous rocking of the eggs was also not necessary.

In several preliminary experiments, avian embryos were allowed to develop to between 5-18 days in order to determine the ideal age for Doppler imaging of CAM vessels. It was found that the optimal age for producing the highest number of viable vessels was between 10-12 days where, vessels were deemed viable if they were visible to the naked eye, embedded in the CAM, and small enough to be mostly within the imaging field of the OCT system. Embryos younger than 7 days were underdeveloped; vessels in the CAM membrane were typically not visible to the eye and air-pockets were not large enough to provide a sufficient working area. While 15-day old embryos produced many viable vessels, at this age embryos were well developed and tended to produce bulk motion artifacts in the Doppler signals. Additionally, it was found that in older embryos (>16 days) the outer shell membrane tended to separate from the shell eliminating the mechanical stability needed when separating the inner shell membrane from the CAM membrane.
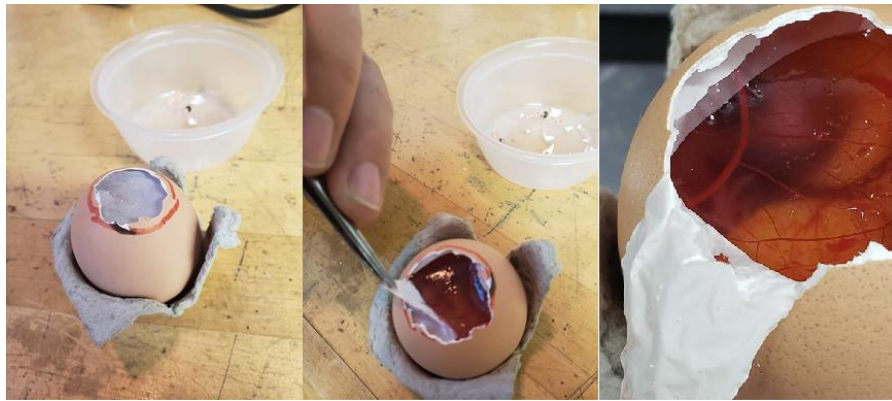
Figure 4.2 Depiction of specimen preperation. Left: egg shell removed in the viscinity of the airpocket exposing inner shell membrane. Middle: Inner shell membrane separation from CAM. Right: Inner shell membrane shown seperated from CAM.

4.1.2 Experimental Procedure

For each data point a vessel was first photographed and scanned via OCT where ~100 B-Scans were acquired at 6 B-Scans/s. B-Scans were appropriately processed to generate both structural

and Doppler images. Given that the heart rate of the avian embryo is between 2-4 Hz [104] averaging was used in the processing of both OCT modalities which ensured that flow variation due to systole and diastole would be filtered. The chosen vessel was targeted using a real-time OCT structural image and was subsequently irradiated with the 2 µm laser. A post irradiation OCT scan was then conducted in an identical manner to the pre irradiation scan and a photograph was acquired. Great care was taken to ensure that both pre and post OCT scans were acquired in the same cross-section. OCT evaluation of outcomes was performed by contrasting pre and post irradiation OCT images (both Doppler and structural) and thus is abbreviated as DS-Eval. Several biological markers were of interest, primarily the presence or absence of flow in the region of interest (ROI) as demarcated by the accompanying OCT structural image in the post DOCT image. The ROI used for DS-Eval was the vessel lumen and the immediate area about the vessel including the layer of the CAM superficial to the vessel. Visual evaluation (V-Eval) was performed by a trained neurovascular surgeon by examining only pre and post irradiation photographs. A vessel was deemed visually sealed when there was no evidence of arterial luminal filling beyond the coagulated region. This also included arterial vessel extravasation. V-Eval was done independently (i.e. the investigator was blinded from the corresponding OCT images).

4.1.3 Statistical Analysis

The Chi-Square statistical test of independence was used to determine if relationships between categorical data exist. The null hypothesis is that no relationship exists between the variables of interest, and that samples are independent. The first specific aim was to determine if coagulation status of the vessel (seal or no seal) after irradiation was related to the method of evaluation (DS or V). The null hypothesis that seal status is independent of the method of evaluation was tested at the 5% level. The second specific aim was to determine if the specificity of V-Eval was related to the non-seal mode determined by DS-Eval. The null hypothesis that V-Eval specificity is independent of the non-seal mode was tested at the 5% level.

4.2 Results and Discussion

Outcomes were classified by DS-Eval into four groups: seal, rupture, partial seal, and unaffected. Each outcome was classified according to the presence of primary and secondary biomarkers. The presence of the primary marker was absolutely necessary to classify a result under the given condition while the presence of secondary markers served to refute or support the conclusions

drawn from the primary marker. Table 1 shows a summary of markers used to classify vessel seals by DS-Eval.

Table 4.1 Summary of Markers Used for DS-Eval		
Classification	**Structural OCT**	**Doppler OCT**
Seal	▪ Evidence of embolism in the post ROI. ▪ Significant change in vessel morphology from pre to post ROI.	▪ No signal present in the post ROI[1].
Partial Seal	▪ Vessel constriction. ▪ Evidence of partial embolism in post image.	▪ Signal area reduced by 15% or more between pre and post ROI[1].
Unaffected	▪ Vessel morphology mostly preserved between pre and post ROI's[1].	▪ Less than 15% change in signal area between pre and post ROI.
Rupture	▪ Vessel disappears in post image (annihilated)[1] OR ▪ Vessel is not intact, evidence of wall disruption[1]. ▪ Significant morphological change.	▪ Doppler signal is present at a vessel cross-section adjacent to the irradiation site. ▪ Diffuse Doppler pattern present.

[1]indicates the primary marker for each classification.

An example of a seal and a rupture are given in Figure 4.3 and an example of a partial seal and an unaffected vessel are given in Figure 4.4.

4.2.1 Detailed Analysis of Bio-Markers Used for DS-Eval

Referring to Table 4.1 the primary marker used for classifying an outcome as a seal was the lack of a Doppler signal in the post ROI. This was the case for nearly all outcomes that were classified as seals. There were some cases where although the Doppler signal had disappeared in the post ROI the outcome was not classified as sealed given that secondary markers strongly indicated otherwise. An unexposed vessel was well characterized by a characteristic lemniscate visible in pre irradiation ROI. Thus, if such was the case where the Doppler signal disappeared, and the lemniscate morphology was retained, then the vessel would not be considered sealed. Completely sealed vessels both lacked a Doppler signal in the post ROI and exhibited a significant change in morphology. A significant change in morphology was considered to have occurred if the characteristic lemniscate disappeared from pre to post structural ROI indicating that
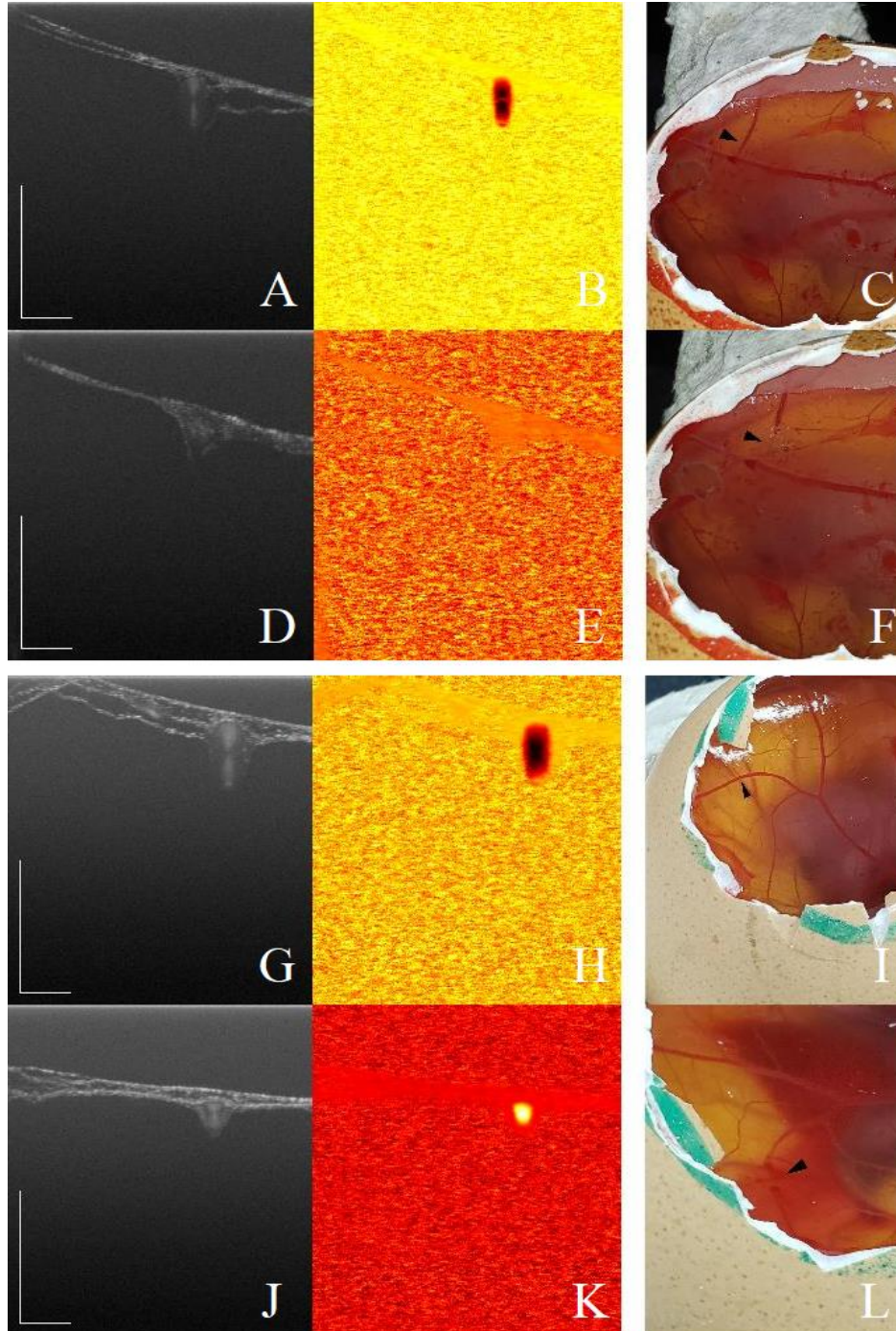
Figure 4.3 Example of a seal (A-F) and a rupture (G-L). Targeted vessels are demarcated by black triangles. Scale bars in each structural image represent 1 mm. Images A, B, and C show pre irradiation OCT structural image, DOCT image, and photograph respectively, while images D, E, and F show the same post irradiation for the seal data point. The Doppler signal present in B disappears in E, thus, this is considered a seal by DS-Eval. This is further supported by the evident denaturing of the vessel structure which can be seen by comparing A and D. Images G, H, and I show pre irradiation OCT structural image, DOCT image, and photograph respectively, while images J, K, and L show the same post irradiation for the rupture data point. Extravasation of blood is clearly visible in L and a strong Doppler signal is clearly still evident in K. Additionally, it should be noted that images J-L were acquired at a location adjacent to the site of irradiation.
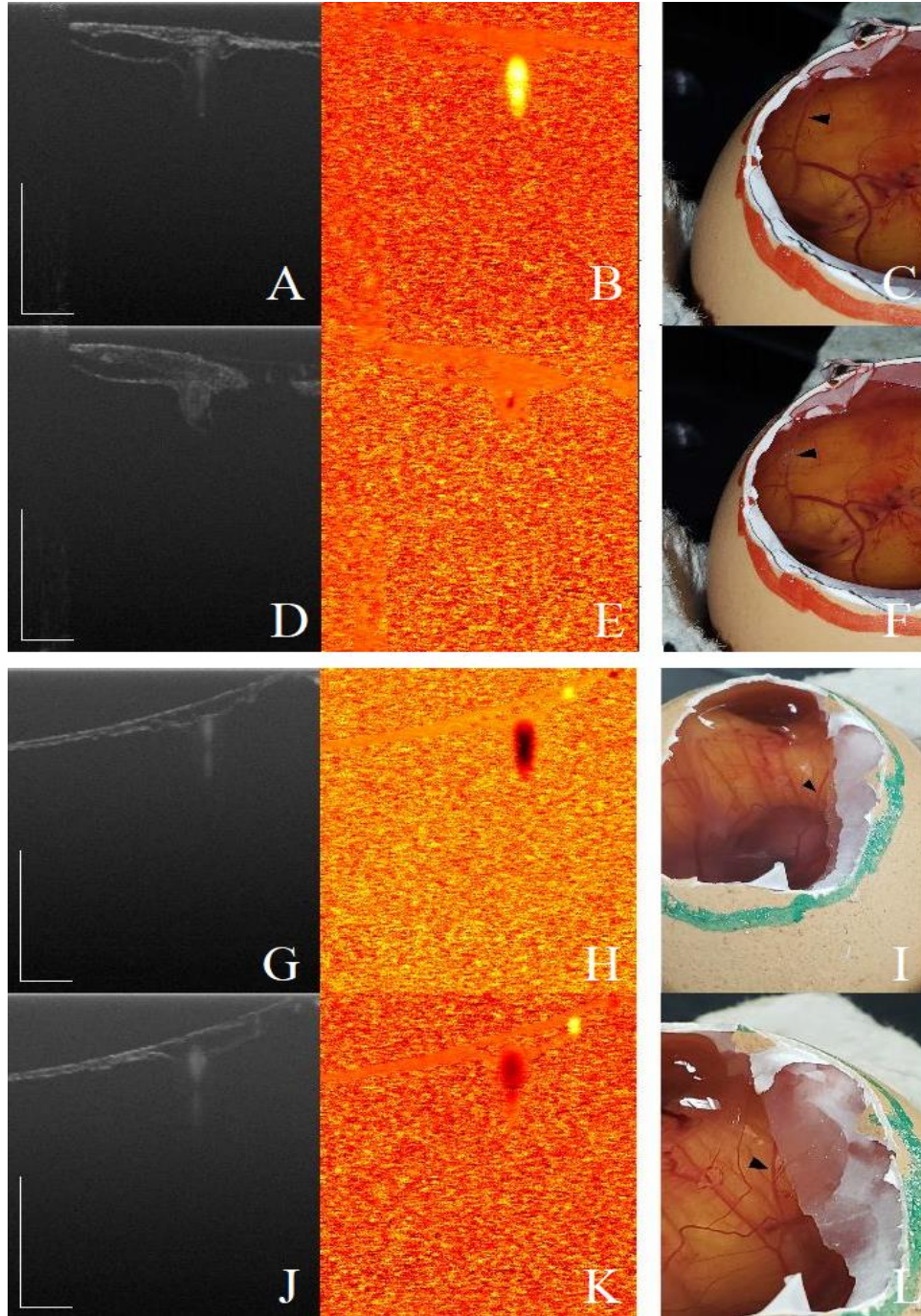
Figure 4.4 Example of a partial seal (A-F) and a vessel that was unaffected (G-L). Targeted vessels are demarcated by black triangles. Scale bars in each structural image represent 1 mm. Images A, B, and C show pre irradiation OCT structural image, DOCT image, and photograph respectively, while images D, E, and F show the same post irradiation for the partial seal data point. Note the small amount of localized flow still present in E despite the vessel appearing to have sealed when comparing C and F. An intact vessel can still be observed in D although it has been severely stenosed. Images G, H, and I show pre irradiation OCT structural image, DOCT image, and photograph respectively, while images J, K, and L show the same post irradiation for the unaffected data point. Little structural change is observable when comparing images I and J although the vessel does appear to have dilated slightly. The Doppler signal observed in H remains present in K although slightly diminished.

sufficient energy was delivered to morph the vessel lumen. The strongest structural marker for a seal was evidence of embolism. Embolism was identified by the recognition of a uniform structural signal apparent in the post ROI, i.e., the characteristic lemniscate morphology was replaced by a homogenous mass in the vessel lumen. The appearance of this structural signal and the accompanying lack of Doppler signal within the post ROI indicates that a static structure has developed within the lumen thereby strongly suggesting embolism. Figure 4.5 gives examples of seal data points which exhibit both evidence of embolism and significant morphological change.
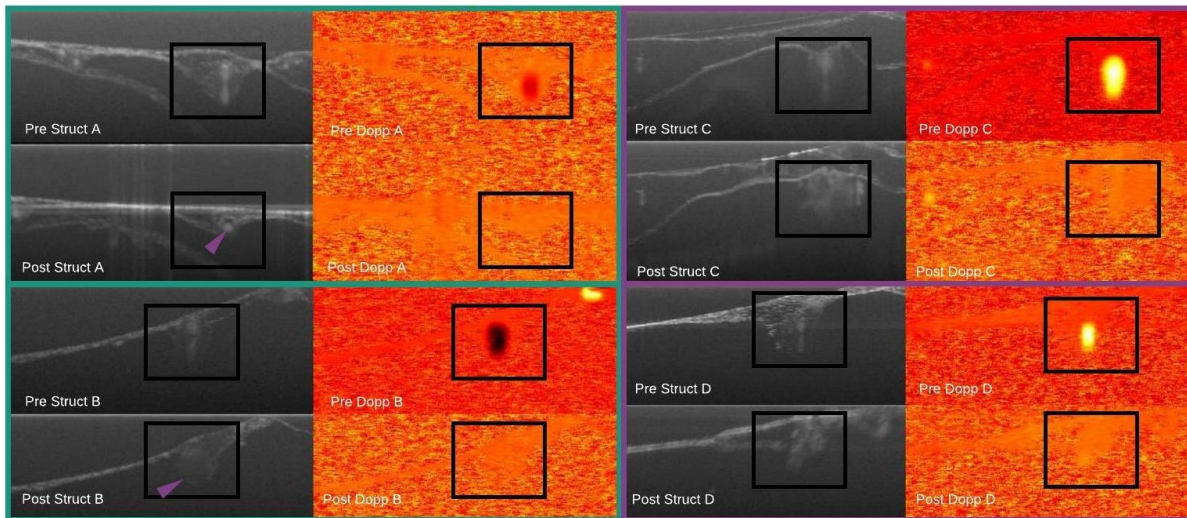
Figure 4.5 Evidence of embolism (green rectangles) and significant morphological change (purple rectangles), secondary markers for seal data points. Black boxes represent ROI's and purple triangles indicate uniform signal within vessel lumen representing embolism. In data points C and D note the disappearance of the lemniscate morphology indicating significant morphological change.

Partial seals were well defined by a decrease in Doppler signal area between pre and post irradiation ROI's. To elucidate, a decrease in Doppler signal area meant that the number of pixels demonstrating Doppler signal in the ROI would decrease from pre to post Doppler images. In order to differentiate from the unaffected classification, at least a 15% decrease in Doppler signal area must be observed for an outcome to be classified as a partial seal. A change in the Doppler signal area directly indicates that some energy reached the lumen and affected blood flow. In some partial seals the decrease in Doppler signal area was a result of vessel constriction (as is evident when comparing Figure 4.4 A and D). Other cases involved partial embolism, where typically blood had coagulated in the most superficial portion of the vessel but not in the deeper portion. Figure 4.6 illustrates both vessel constriction and partial embolism.
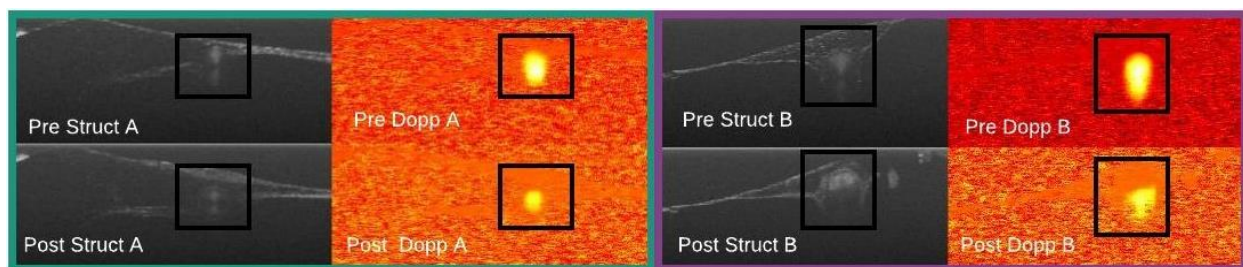
Figure 4.6 Vessel constriction (A, green rectangle) and partial embolism (B, purple rectangle), markers indicating a partial seal. Black boxes indicate the ROI's. In data point A, the Doppler signal area has clearly been reduced by more than 15% while vessel constriction is apparent from the change in vessel diameter from pre to post structural images. In data point B, the Doppler signal area has decreased by more than 15% while from the post structural image, the homogenous signal coming from the superficial portion of the vessel lumen indicates that partial embolism has been achieved.

The unaffected classification is a misnomer as many vessel irradiation outcomes in this category certainly exhibited some response to laser irradiation. A more appropriate title for this classification would have been "no significant hemostatic effect" but, for brevities sake, unaffected was used. A vessel was considered unaffected if vessel morphology was mostly preserved from pre to post irradiation. This was apparent by comparing pre and post structural images. "Mostly preserved" indicates that the vessel diameter remained within 10% of its unexposed state and that the lemniscate morphology was present in the post structural ROI. Additionally, for an outcome to be classified as unaffected, the Doppler signal area would have to remain within 15% of its original size. Both the 10% limitation on diameter change and the 15% limitation on Doppler signal area change were arbitrarily chosen. Here the primary purpose of DS-Eval was to objectively classify outcomes as sealed or not sealed and thus, since both partial seal and unaffected are both non-seal outcomes, it is not crucial to have objective differentiation between the two categories. Figure 4.7 gives two examples of unaffected data points.
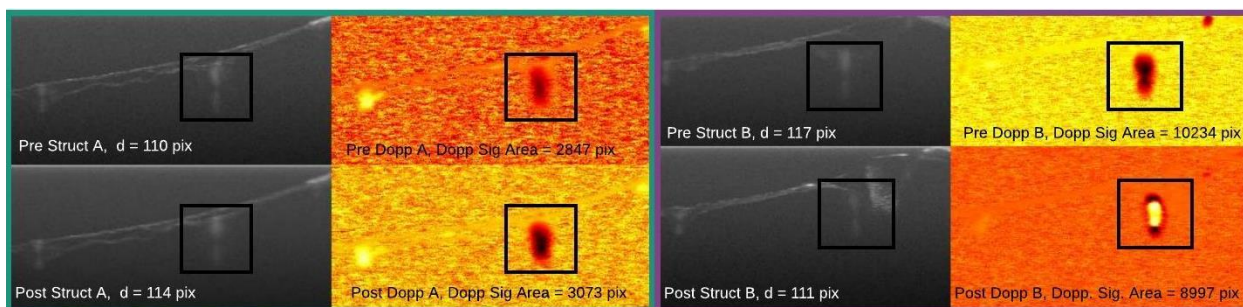
Figure 4.7 Two examples of unaffected data points. Black boxes indicate the ROI's. Both data point A (green rectangle) and B (purple rectangle) exhibit less than 10% change in vessel diameter and less than 15% change in Doppler Signal Area and thus both of these data points were classified as unaffected. Vessel diameters are labeled in each structural image (d) and are reported in pixels. Doppler Signal Area (Dopp Sig Area) is labeled in each Doppler image and is also given in pixels.

Vessel rupture was declared whenever there was evidence of bleeding. Several markers were good indicators of bleeding especially vessel eradication which was evident from structural images when the vessel was no longer within the field of view. Alternatively, bleeding was also evident when the structural images exhibited vessel wall disruption differentiated from complete annihilation as part of the vessel wall remained intact post irradiation. Secondary markers included the adjacent Doppler signal and the diffuse Doppler signal. The adjacent Doppler signal was acquired at an intact cross section of vessel directly beside the irradiation site. If Doppler signal was present here it was assumed that blood flow had not been ceased within the vessel and thus a rupture was probable. The diffuse Doppler signal was recognized when Doppler signal existed outside of the ROI indicating vascular extravasation. It is termed "diffuse" as the Doppler signal would often be spread over the image and not localized to the ROI.
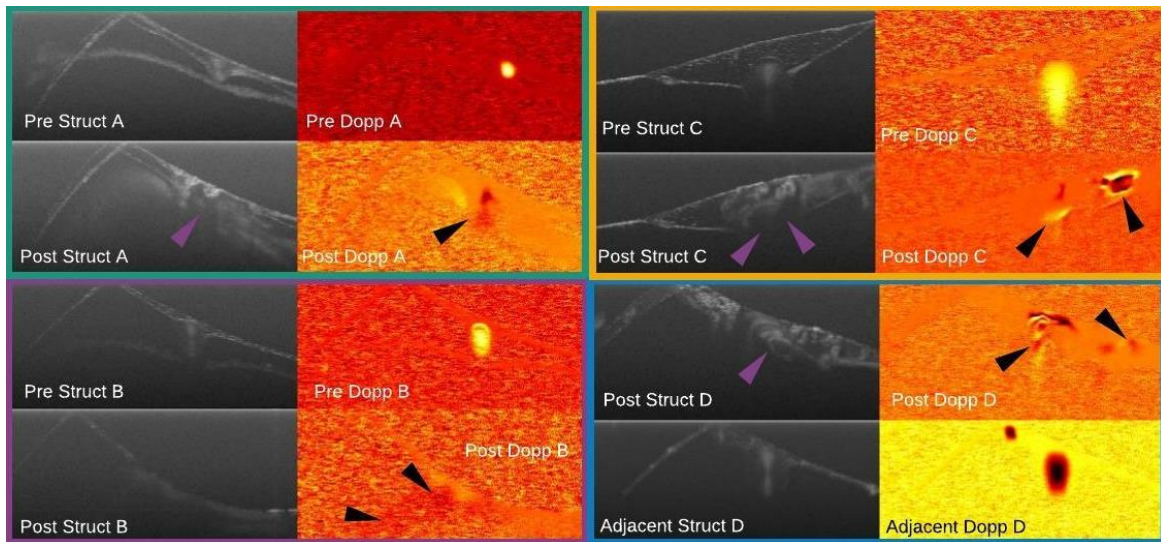
Figure 4.8: Biomarkers used for identifying ruptures with DS-Eval. Data point A (green rectangle) demonstrates a wall breach indicated by the purple arrow which indicates rupture while the presence of the diffuse Doppler pattern (black arrow) supports this classification. In data point B (purple rectangle) complete annihilation of the vessel is evident by comparing pre and post structural images, the diffuse Doppler pattern is also visible here although less obvious. Data point C (yellow rectangle) exhibits wall disruption (purple arrows) and a very strong diffuse Doppler pattern (black arrows). Data point D (blue rectangle) is an example of a rupture where an adjacent image was used to further verify the rupture. Wall breach and diffuse Doppler pattern are evident within the post images while the adjacent scan at a cross section of intact vessel exhibits flow further verifying a rupture has occurred. ROI's are left unlabeled for clarity.

4.2.2 Additional Insights Generated through DS-Eval

DOCT used in this manner has also revealed a variety of biologically related insights into the energy sealing of vessels. Referring to the seal data point in Figure 3, it seems that the sealed vessel has been both constricted and embolized post irradiation which suggests that energy sealing is a two-pronged process. The partial seal data point of Figure 4.4 exhibits vessel constriction but complete embolism is not achieved as is apparent from Figure 4.4D and 4.4E. This could be a result of insufficient energy reaching the lumen of the vessel and failing to fully coagulate blood. While the vessel structure in the unaffected data point remains nearly unchanged, a marked increase in vessel diameter is visible when comparing Figure 4.4G and 4.4J while the flow velocity has decreased (apparent from the diminished Doppler signal in Figure 4.4K). This widening of the vessel is an interesting result and warrants further investigation. Generally, these in situ microscopic observations of vascular biomechanical response to laser irradiation are indispensable as they lend greater insight as to the mechanisms involved in laser sealing. Thus, the methodology presented in this study can be extended beyond seal evaluation to generate understanding as to the microscopic mechanisms responsible for vessel sealing. Future studies will involve dynamic structural and Doppler imaging in order to visualize the sealing process.

4.2.3 Comparing DS-Eval and V-Eval and the Importance of Re-evaluating Visually Evaluated Hemostatic Systems

Of the 104 vessels irradiated in this study 30 were seals, 31 ruptured, 20 were partial seals, and 23 were unaffected by DS-Eval. In order to compare DS-Eval to V-Eval, the four groups generated by DS-Eval were generalized into seal and non-seal groups where the non-seal group included partial seals, ruptures, and unaffected outcomes. In this way DS-Eval reported that 29% of vessels had sealed (30 seals and 74 non-seals) compared to V-Eval which reported that 47% of vessels had sealed (49 seals and 55 non-seals). A true positive (TP) occurred when both DS and V-Eval resulted in a seal, a true negative (TN) occurred when both DS and V-Eval resulted in a non-seal, a false positive (FP) was declared when V-Eval resulted in a seal while DS-Eval resulted in a non-seal, and a false negative (FN) occurred when V-Eval resulted in a non-seal and DS-Eval resulted in a seal. Following this logic, V-Eval generated 27 TP's, 52 TN's, 22 FP's, and 3 FN's resulting in a sensitivity of 90%, specificity of 70%, and an overall accuracy of 76%. It was found that

whether the outcome was classified as sealed or not-sealed was dependent on the classification methodology, DS or V-Eval, and this was statistically significant ($p = 0.01$ using a two-tailed Chi-Squared test with Yates correction). Table 4.2 gives the contingency table from which the Chi-Squared statistic was calculated. Further, it was found that V-Eval specificity was dependent on the type of non-seal classification (partial seal, rupture, or unaffected) and this finding was also significant ($p < 0.0001$, Chi-Squared test). Table 4.3 shows the contingency table from which the Chi-Squared value was calculated.

Table 4.2 The Association Between Seal Evaluation Method and Outcomes

	DS-Eval	V-Eval	Total
Seals	30	49	79
Non-Seals	74	55	129
Total	104	104	208

Table 4.3 The Association between V-Evals and DS-Eval Non-Seal Groups

	V Seals	V Non-Seals	Total
Rupture	4	27	31
Partial Seals	14	6	20
Unaffected	4	19	23
Total	22	52	74

From the data presented in Tables 4.2 and 4.3, it is reasonable to conclude that in laser sealing studies where V-Eval was used to evaluate energy seals, reported seal rates are likely inflated. Further, this inflation is likely a result of an inability to differentiate partial seals from seals by eye given that the greatest amount of FP's generated by V-Eval were partial seals. Meticulous hemostasis is paramount for all surgical procedures, and thus all coagulated vessels should be completely sealed. Partial seals would pose a significant risk, especially if partial seals resulted in slow ooze from the vessel that is not detected visually at the time of surgery. Delayed post-surgical hematomas are not uncommon, and it is reasonable to assume these may be due to incompletely coagulated vessels. Thus, current laser technologies used for the purpose of vessel sealing which were evaluated visually should be reevaluated to ensure that complete vessel seals were achieved.

4.3 Conclusion

The primary objective of this study was to develop an objective energy seal classification methodology employing DOCT. The methodology developed termed DS-Eval uses specific biological markers listed in Table 4.1 to determine whether a vessel had been sealed. Generally,

the presence of these markers is not based on subjective opinion but rather on numerical information or clear imagery. Incidentally, DS-Eval is objective making it suitable for scientific processes and generating reliable results in the evaluation of laser sealing systems. Implementing DS-Eval at times was challenging; the acquisition time of each data point was approximately 15 min because the specimen had to be maneuvered into the imaging field of the OCT beam and a total of ~200 B-scans (including pre and post scans) were acquired at 6 B-Scans/second. In some cases, movement of the embryo caused motion artifacts to appear in the Doppler images while structural images were at times ruined by brightness artifacts. Post structural images were especially susceptible to brightness artifacts given that tissue coagulation increases reflectance (see Section 2.3.2). In both cases a rescan of the vessel was required and acquisition times were as long as 30 minutes. The processing time of each data point was approximately 2.5 minutes. Improvements to DS-Eval workflow could have been realized by parallelizing the Doppler and Structural OCT processing algorithms and upgrading supporting technology, primarily the devices used to maneuver the optical payload into position, as this was the most time-consuming process. Implementing this methodology required a degree of familiarity with OCT tissue imaging given that identifying specific biological markers was required. While this limits usability, the same degree of familiarity is required with most medical imaging modalities.

In this study, it was presumed that DS-Eval had an accuracy of 100%. While this is certainly not absolute, the author believes that the accuracy of DOCT is very near to the gold standard CT angiography given DOCT's high velocity resolution. Of course, there are several possible sources of error that could have potentially decreased the accuracy of DS-Eval such as user error (inability to detect failed scans resulting from motion and brightness artifacts) and inherent DOCT limitations. For example, the flow sensitivity of DOCT is related to the A-line rate and the Doppler angle, thus if there was a case where the vessel was scanned in such a way that the imaging beam was orthogonal to the flow direction DS-Eval would fail. This could be avoided by proper optical payload positioning relative to the vessel. Additionally, it is also possible to encounter residual flows that are slower than the velocity resolution of the DOCT system which would also result in a failed classification. An interesting future study would be the direct comparison of DOCT as implemented in this study to CT angiography such that a measure of DS-Eval accuracy can be obtained.

Many of the outcome classifications depended on the characteristic lemniscate biomarker. This lumen morphology, common among all CAM vessels, is believed to be a result of vessel proliferation. Vascular proliferation occurs rapidly within the first 11 days of embryonic development and thus this is a valid conclusion [105]. Additionally, throughout the course of data gathering cases of nearly completely parted vessels were observed. In order for the DS-Eval methodology to be extended to other species, the lemniscate biomarker would have to be replaced by a more suitable marker representing the natural state of vessels for that species. Further, arterial-venous differentiation occurs in the CAM between days 10 and 12 meaning that a single characteristic morphology is able to represent all vessels in the CAM until day 13. In the case of human vasculature for example, it may be necessary to define natural state biomarkers for both arteries and veins given their vastly different morphologies.

DS-Eval of vessel seals is not limited solely to laser-based systems. It can be extended for use across all energy sealing systems, increasing its utility. Its limitation imposed by a shallow imaging depth is compensated for by its high velocity resolution and valuable structural feedback. Further, DOCT can be used in the seal classification of large vessels if used intravascularly, which is already a commonly used technique for the evaluation of blood clots [106]. Here DS-Eval was presented as a bench top testing method for laser-based energy sealing systems. Clinical translation of this methodology will not be possible without significant improvement to supporting technology.

Chapter 5: Evaluating the Thulium Fiber Laser as a Hemostatic Instrument

LASER is a unique form of energy given that it remains coherent even after propagating through free space. This gives the laser a distinct advantage over other energy based hemostatic systems; selective energy deposition can be achieved at a distance. Thus, lasers can eliminate all contact-induced negative effects associated with other hemostatic systems such as carbonization and tissue adhesion. As can be seen in Figure 5.1, tissue adhesion is a phenomenon that occurs as a result of contact-based hemostasis where, after sealing the vessel, the instrument adheres to the coagulum potentially leading to iatrogenic injury (e.g. vessel rupturing and tissue scaring as the instrument is pulled away from the tissue) [107]. Various factors contribute to tissue adherence such as temperature reached by the tissue, roughness of contact surface, and surface coating [108], all of which can be eliminated by using contactless laser-based coagulation. Several attempts to ameliorate this issue in electrosurgical hemostatic instruments have been carried out by researchers such as thermocontrol [109–111], computerized impedance control [112–114], irrigation [115,116], and augmented tip coatings [108,117,118]. While effective in reducing the occurrence rate of vessel adhesion, augmented tip coatings tend to introduce a limited device lifetime as coatings tend to degrade after multiple sterilizations [119], incurring high costs. A well-known coated bipolar is the Spetzler-Malis disposable bipolar which costs between 40-60 USD per unit (Figure 1.2). Disposable instruments contribute to 84% of all operating room equipment costs thus eliminating the need for a commonly used instrument such as the Spetzler-Malis would be economically beneficial [120]. Thermocontrol has shown to decrease tissue adherence but not completely in thermocouple feedback schemes. Of note, is the IsoCool^{TM} bipolar forceps which control thermal distribution in the tips via an embedded tubule which allows for the diffusion of fluid, and thus thermal energy, within the forceps. It is claimed that the IsoCool^{TM} forceps eliminate tissue adherence even after prolonged periods of coagulation [110,119], however supporting evidence is scant. Impedance control devices prevented tissue adherence to a certain degree, however, they were only effective at lower power levels [114]. Irrigation does suppress tissue adherence by distributing thermal energy, but excessive irrigation can cause hemostatic failure and irrigation with saline solution has shown to increase tissue adherence [108,119]. Even very modern laparoscopic bipolar instruments such as the ENSEAL® X1 and the LigaSure Impact^{TM} exhibited tissue adhesion rates of 15% and 47% respectively when tested in-vivo [121]. None of the above-mentioned device modifications have

been able to eliminate the issue entirely and therefore tissue adhesion is still a prominent problem. Laser-based systems, utilized in a contactless fashion, have the potential to solve this problem.
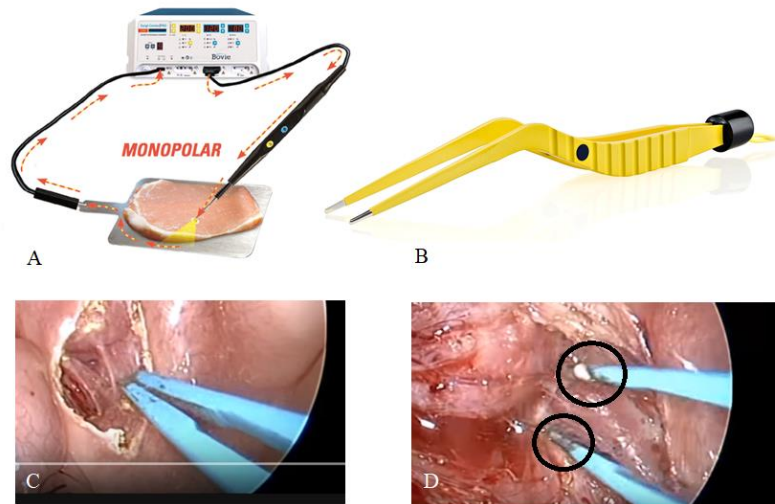
Figure 5.1: Depiction of a monopolar coagulator (A) and a Spetzler-Malis disposable bipolar coagulator (B). Monopolar devices require a grounding electrode such that electrical energy flows through the patient increasing the chance of complications. Disposable bipolars are effective in reducing tissue adhesion however incur higher costs. Unused bipolar forceps at the onset of a tonsillectomy (C), after 2 min of use (D). Tissue adherence is evident as the accumulation of char and coagulum, demarcated by black circles, in the forceps is evident.

The brain presents a unique challenge to surgeons. Brain tissue is very delicate meaning that sutures cannot be used to stem the flow of blood and energy sealing must be employed (which is why Cushing requested Bovie's services in the first place, see Introduction). The brain also contains over 100 billion neurons [122,123], meaning that every volumetric unit of tissue is precious. Conventional advanced bipolar cauterizers incur an average collateral damage radius of 4 mm resulting in countless neurons being unnecessarily destroyed. The uniqueness of the situation presents an opportunity for laser energy sealing. The interaction between laser and tissue is highly tuneable given that many laser parameters contribute the ultimate tissue effect (see Figure 1.1). At 1942 nm, the Thulium fiber laser is especially well suited for neurosurgery given its coincidence with an absorption maxima of water and subsequently its relatively shallow optical penetration depth (refer to Eq. 2.7). As a fiber laser, it has distinct advantages over equivalent bulk optic lasers, such as the Thulium Yttrium Aluminum Garnet laser (Tm:YAG) and the Holmium Yttrium Aluminum Garnet laser (Ho:YAG), simply because of its potentially small footprint in the surgical suite. It is well known that wavelengths longer than 2100 nm cannot be readily transmitted by silica fibers thus, the Thulium fiber laser offers the greatest absorption in

aqueous media while still being easily guidable. Thulium lasers at similar wavelengths have shown great promise in compression-based laser sealing however they have been discredited due to char formation and a poor optical penetration depth in the case of sealing large vessels (>4mm) [94]. Burns et. al evaluated four lasers including the Thulium laser and found that the Thulium laser sealed less than 20% of vessels (n = 5); a result attributed to thermally extreme interactions with tissue triggering vessel rupture [100]. Vessel sealing using non-hydrolytic lasers has also been investigated. N. Fried's group developed a device which incorporated a 1470 nm diode laser into a clamping device in a series of papers [94–96,99]. The diode laser demonstrated superior sealing capabilities when compared to several other lasers given that its optical penetration depth matched with the compressed thickness of the tissue [94]. Seal rates of small vessels (3 mm or less in diameter) were reported to be greater than 90% however tissue adherence, although infrequent, was an issue [99]. Rees et al., exposed arteries in-vivo to gold laser (GoAs) at 980 nm in a contactless manner. Arteries were subjected to continued doses until visibly sealed and it was reported that with this strategy a 100% seal rate was achieved. The mean therapeutic time for vessel sealing was 2.24 s and 3.41 s for straight and angled fibers respectively [97]. Kimel et al., explored the effects of photoangiolytic lasers in two studies [47,73]. In [73] it was shown that the probability of a third-order vessel (average diameter of 112-113 µm) being permanently occluded was ~61% for arteries and ~26% for veins after 3 exposures of 10 ms by an Argon ion dye laser. While photoangiolytic lasers are an attractive tool for hemostatic systems, their high selectivity in tissue interaction results in a limited range of applications. This selectivity has exhibited issues in the sealing of veins given the vastly different absorption coefficient between oxygenated and deoxygenated hemoglobin [47].

If a hydrolytic laser, such as the Thulium laser, can be tuned for the purposes of hemostasis, then both ablation and hemostasis can be achieved across most tissue types with a single instrument. This will eliminate the need for the use of photoangiolytic lasers and disposable instruments potentially reducing the economic impact of surgical hemostasis. Further, by using LASER, this can be achieved in a contactless fashion eliminating tissue adherence entirely. The Thulium fiber laser as a hemostatic instrument lends itself to use in neurosurgery given its high absorbance in water and tuneability. For these reasons, it is worthwhile to investigate whether better hemostatic performance can be achieved with the laser than reported by Burns in [100]. It is believed that poor seal rates reported by Burns are due to a limited exploration of laser

parameters. Thus, in this chapter, the Thulium laser will be evaluated as a hemostatic instrument using DS-Eval methodology developed in Chapter 4. The effects of varying exposure time, average power, and spot size on the seal rate (number of vessels sealed per total vessels irradiated) will be studied with the intent of finding a set of laser parameters which produces the highest seal rate. Biological parameters such as vessel depth and vessel diameter will also be studied in relation to the seal rate. The degree of collateral damage induced by the laser will also be measured.
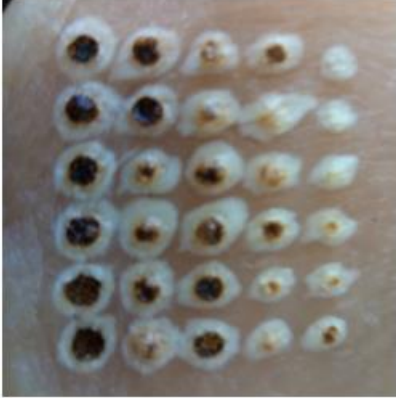
5.1 Methodology

All experiments were carried out according to recommendations provided by the Research Ethics Board of the institution. A total of 94 avian egg embryos were cultivated and appropriately prepared for the experiment which yielded 122 viable vessels. Specimen preparation was carried out identically to methods outlined in Chapter 4. Each vessel was subjected to Thulium laser irradiation where exposure time, spot size, and average power were varied in order to generate a variety of outcomes. For each vessel an OCT structural image, OCT Doppler image, and photograph were acquired for both pre and post laser exposure forming a single data point. Pre and post images were examined to evaluate the outcome.

5.1.1 Determining Baseline Coagulative Parameters

Baseline parameters for coagulation were determined by performing a burn test on chicken breast. A combination of laser parameters was sought where pure coagulation was induced such that a more coordinated approach could be taken in the in-ovo experiments. Burns were formed in a grid pattern on chicken breast at average powers varying between 4.6 W to 14.7 W, corresponding to varying the pump current between 1.8 A to 3.6 A in 0.2 A intervals, at exposure times: 1 s, 2 s, and 3 s (Figure 2). At 1 second exposure time, purely coagulative effects were generated between 4.6 W and 7.5 W. As the power level increased, ablation never occurred but coagulation was accompanied by charring. At 2 s exposure time, and lower power levels, coagulation was achieved but was also accompanied by charring. Power levels over 11.75 W caused ablation. Three seconds of exposure time nearly always triggered ablation, except at 4.6 W. It should be noted that in some samples a charred cap was formed over ablation craters (see n24, n14, n9) which caused the samples to misleadingly appear to be purely coagulative when in fact ablation occurred. Given that the CAM membrane is mechanically weaker than muscle tissue, and, that blood has a higher water content than muscle tissue (Whole blood 80% [40], skeletal muscle 75% [41]), it was

inferred that the effects observed in the chicken breast model will be amplified in the CAM model. Therefore, the baseline laser parameters used in subsequent experiments were selected to be 4.6 W and 1 s exposure time.

n25	n19	n13	n7	n1
9.5	13.8	7.2	11.8	4.6
n26	n20	n14	n8	n2
10.6	14.7	8.4	12.7	6.0
n27	n21	n15	n9	n3
11.8	4.6	9.5	13.8	7.2
n28	n22	n16	n10	n4
12.7	6.0	10.6	14.7	8.4
n29	n23	n17	n11	n5
13.8	7.2	11.8	4.6	9.5
n30	n24	n18	n12	n6
14.7	8.4	12.7	6.0	10.6

Figure 5.2 Results of burn test for determining purely coagulative parameters. Grid of burns induced in chicken breast (left), parameters associated with each burn (right). Green, Yellow, Red is 1s, 2s, 3s exposure time respectively. The power associated with each burn in watts is given in each grid square.

5.1.2 Experimental Procedure

This study was divided into two phases. The first attempted to adhere to existing laser sealing study methodology where each vessel is irradiated under precise laser conditions and an outcome is determined. Using the baseline condition as a starting point exposure time, spot size, and average power were varied to create several laser operating conditions. Each parameter was varied independently to observe its effects on the overall seal rate. Average power was varied between 1.22 W and 4.62 W given that, from the chicken breast burn test, it was inferred that powers greater than 4.62 W would induce ablation in the CAM model. Exposure times were varied between 0.5 s and 1.5 s in order to study exposure times in and around 1 s while spot size was varied between 0.03 mm^2 and 0.06 mm^2 due to limitations of the system. Referring to Chapter 3, exposure time was regulated using a shutter controller, average power was varied by adjusting the laser pump current, and spot size was varied by offsetting the beam axially by a set distance. From the initial variations of the baseline conditions, the two conditions which exhibited the highest seal rate were then individually varied to determine if the seal rate could be improved. A total of 21 distinct laser operating conditions were evaluated and are listed in Table 5.1. Note that in Table 5.1 some conditions are repeated as conditions are grouped according to parameter varied. For each condition no less than 5 data points were acquired with the exception of 2.38 W, 1.00 s, and 0.06 mm^2 where only four points were acquired due to experimental limitations. It was decided to

71

acquire five data points per condition to maintain consistency with work done in the literature such that results can be comparable.

Table 5.1 Laser Operational Conditions Studied and Their Associated Laser Parameters[a]

Parameter Varied	Power (W)	Exposure Time (s)	Spot Size (mm^2)
Average Power (A)	1.22	1.00	0.03
	2.38*	1.00	0.03
	3.01	1.00	0.03
	2	1.00	0.03
Exposure Time (F)	4.62	0.50	0.03
	4.62	0.75	0.03
	4.62	1.00	0.03
	4.62	1.50	0.03
Spot Size (C)	4.62	1.00	0.03
	4.62	1.00	0.04*
	4.62	1.00	0.05
	4.62	1.00	0.06
Optimal Spot Size*: Average Power (B)	1.22	1.00	0.04
	2.38	1.00	0.04
	3.01	1.00	0.04
	4.62	1.00	0.04
Optimal Spot Size*: Exposure Time (E)	4.62	0.50	0.04
	4.62	0.75	0.04
	4.62	1.00	0.04
	4.62	1.50	0.04
Optimal Average Power*: Spot Size (D)	2.38	1.00	0.03
	2.38	1.00	0.04
	2.38	1.00	0.05
	2.38	1.00	0.06
Optimal Average Power*: Exposure Time (G)	2.38	0.50	0.03
	2.38	0.75	0.03
	2.38	1.00	0.03
	2.38	1.50	0.03

[a]Variations of average power, variations of spot size, and variations of exposure time. * indicates optimal conditions discovered from baseline variations. (X) for correspondence to graphs of Figure 5.6.

In the second phase of the study, a realistic surgical scenario was emulated. When presented with a vessel that must be sealed a surgeon will continuously attempt to seal that vessel until it can be reasonably concluded that the vessel has been sealed. Thus, in this phase of the experiment, a dose-until sealed method was adopted where a vessel is subjected to continuous doses of 1942 nm light until sealed. A single laser operational condition was used, and was the condition which exemplified the highest seal rate from phase 1. Eighteen vessels were irradiated with the objective of determining the seal rate given the dose-until-sealed approach. DS-Eval was used intermittently to determine if the vessel has been sealed. In this way only two outcomes were possible. The vessel was either sealed or was an irreparable rupture where, regardless of the total dose administered and the best effort of the researchers, the vessel could not be sealed.

5.1.3 Measurement of Biological Parameters

Vessel diameter and vessel depth were measured to determine if they were related to the seal rate. The extent of collateral thermal damage induced by the Thulium laser was measured to compare to existing values in the literature as well as to collateral thermal damage produced by advanced bipolars. Collateral thermal damage was only measured for seal data points. All parameters were measured using point-picking on OCT structural images. Vessel diameter was measured by choosing two points on the circumference of the vessel, one at the most superficial point of the vessel and another at the deepest point. Vessel depth was measured by choosing a point on the surface of the CAM membrane immediately superficial to the vessel and a second point on the same axial axis on the most superficial point of the vessel. Point-picking for vessel depth and vessel diameter are depicted in Figure 5.3.

Figure 5.3 Depiction of point-picking for measuring vessel diameter and vessel depth. In this case the diameter and depth of the vessel was 80 and 15 pixels respectively. Dots represent pixels for which data is being displayed.

In using the above defined point-picking methods both vessel diameter and depth were obtained in units of pixels. To convert from pixels to µm, OCT structural imaging was used to image a glass slide of known thickness. Then, from the structural image, and again using point-picking, the thickness of the slide was measured in pixels. To obtain the distance per pixel in µm the following equation was used:

$$Distance\ per\ pixel = \frac{2 * OPL}{pixel\ width\ of\ slide} \tag{1}$$

where OPL is the optical path length and equals n_{glass} multiplied by the glass slide thickness. Since light travels through the thickness of the glass twice, once on incidence and once on return, the total OPL is actually 2*OPL. By dividing the total OPL by the pixel width of the slide, the distance per pixel is obtained. Since the pixels in these images are rectangular, the glass slide was imaged twice, once where the glass slide was placed orthogonally to the beam and once where the glass

slide was parallel to the beam. In this way the distance per pixel was obtained both laterally and axially. This methodology is illustrated in Figure 5.4 where structural images of the glass slide are shown. Given that the glass slide thickness was 0.1 mm and that $n_{glass} = 1.5$, the distance per pixel axially was found to be 4.9 µm while the distance per pixel laterally was found to be 6.1 µm.
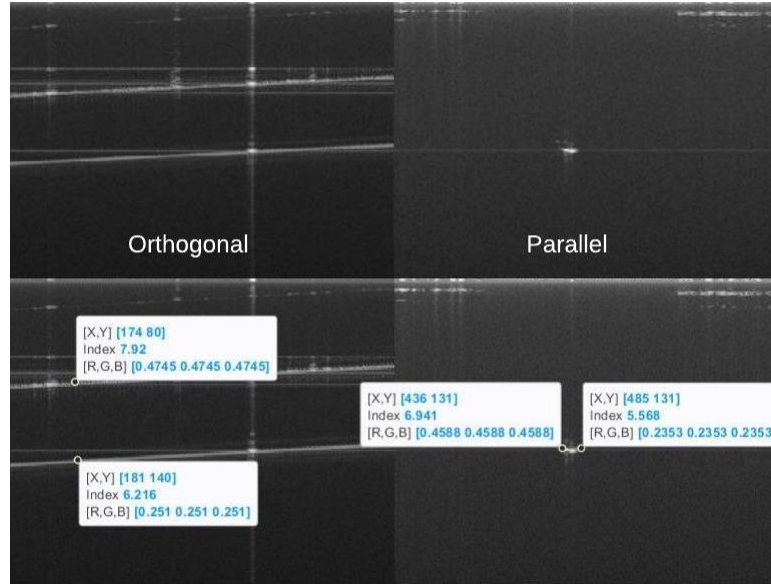
Figure 5.4 Structural images of glass slide used to determine the distance per pixel. Left is the structural image of the glass slide where the slide was placed orthogonally to the beam. Right is the structural image where the glass slide was placed parallel to the beam. Bottom images show the picked points. Dots represent pixels for which data is being displayed.

Strictly speaking, collateral damage was defined as the amount of denatured tissue immediately beyond the extents of the vessel. The region of denatured tissue beyond the natural extents of the vessel was named the Heat Affected Zone (HAZ). This distance was acquired by comparing pre and post photographs where, the natural state of the CAM and extent of the vessel was observed in the pre irradiation photograph, and the post photograph was observed to determine what portion of the CAM had been denatured. Then, the extent of collateral damage was measured by choosing two points at the extremities of the HAZ on an axis perpendicular to the vessel. Since the HAZ was measured by point picking on photographs, HAZ diameters were represented in units of photograph pixels. To convert this measurement into micron, the lateral diameter (natural extent) in micron of the vessel was acquired using point picking on the corresponding OCT structural image. This measurement, along with the lateral distance per pixel calculated above, allowed the conversion of HAZ from structural image pixels to micron and then from photograph pixels to micron. Measurement of the HAZ is depicted in Figure 5.5.

Figure 5.5 Depiction of HAZ point picking. From left to right: a structural OCT image followed by two photographs. The lateral natural extent of the vessel is firstly acquired in structural image pixels. By multiplying by the lateral distance per pixel (6.1 µm) the natural extent of the vessel is then acquired in micrometers. The natural extent of the vessel is then measured in photograph pixels and thus the distance per photograph pixel is known. The denatured extent is then measured in photograph pixels, by multiplying this value by the distance per photograph pixel the denatured extent can be acquired in micron. The HAZ is then calculated by subtracting the natural extent of the vessel from the denatured extent. In this case HAZ = 872 µm. Dots represent pixels for which data is being displayed.

5.2 An Analysis of the Seal Rate in Relation to Laser Operational Parameters

The overall seal rate exhibited by the Thulium laser in this study was 29%. This is across all vessels and irrespective of the laser's operational conditions. The highest seal rate exhibited by any operational condition was 60% while the lowest was 0%. Figure 5.6 exhibits the effect of varying laser operational parameters on seal rate. From baseline variations, three spot sizes exhibited the highest seal rate of 40%: 0.04 mm^2, 0.05 mm^2, and 0.06 mm^2 (Figure 5.6 C). As a result, 0.04 mm^2 was arbitrarily selected to move on to the second phase of parameter varying. Of the average powers studied during baseline variations, 2.383 W exhibited the highest seal rate by far at 60% (Figure 5.6 A). In the second phase of parameter sweeping, two more conditions exhibited the maximum seal rate of 60% and are plotted in Figure 5.6 B and F. In [100] a total of 15 vessels were irradiated with Tm^{3+} laser at 2 W, 4 W, and 10 W (n = 5 for each power level). Each vessel was irradiated with two pulses of 20 ms width each for a total exposure time of 40 ms. Spot size was not reported. Less than 20% of the vessels in this study sealed (by visual examination). While the maximum seal rate of 60% achieved in this study is much higher than that reported by in [100], there was no observable trend between any of the laser parameters varied and the seal rate. As such, it is possible that this observed seal rate was a result of chance. Additionally, the lack of a trend contradicts the concepts developed in Chapter 2 where all three parameters varied in this experiment are expected to have some correlation to the seal rate. There are several possible causes to this lack of an observable trend. Firstly, by bulk examination of the data presented in Figure 5.6 any patterns due to the various non-seal modes may not be apparent. Closer examination may reveal relationships between the laser operational parameters and the resultant non-seal modes. Secondly, biological parameters were not controlled for. Both vessel

75

size and depth variation could have resulted in the lack of correlation between laser parameters and seal rate. In addition to this, tissue dehydration was believed to play a prominent role since the 1942 nm wavelength is strongly absorbed by water. Finally, it is also possible that an insufficient number of data points were acquired to observe an overall trend. Each of these factors will now be discussed in detail.
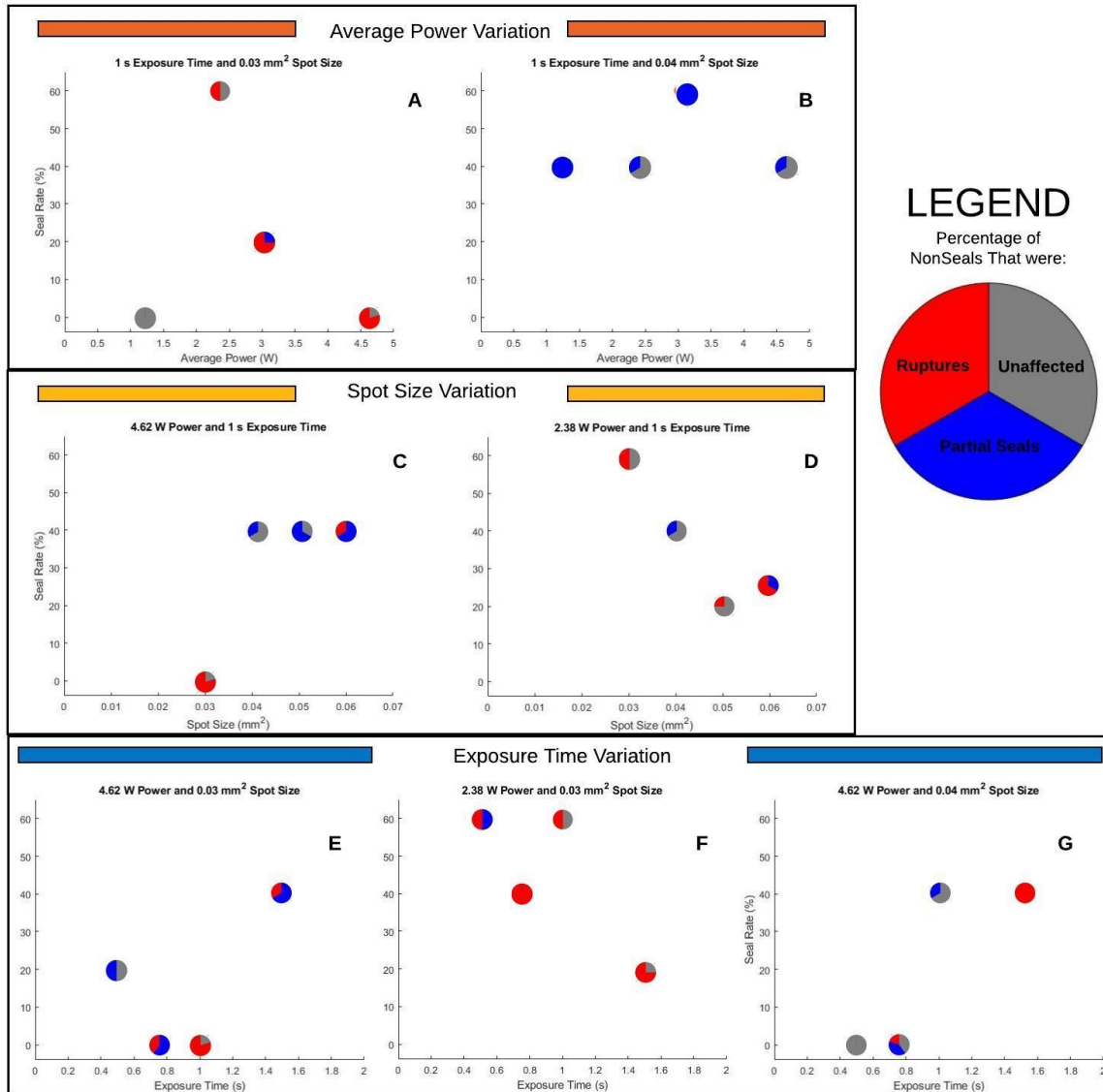
Figure 5.6 Seal rates corresponding to varying average power, spot size and exposure time variation. The sub plot groups are colour coded to match the variations listed in Table 5.1. (A) Baseline condition variation, (B) Optimal spot size condition variation, (C) Baseline condition variation, (D) Optimal average power condition variation, (E) Baseline condition variation, (F) Optimal average power condition variation, and (G) Optimal spot size condition variation. Each marker is a pie chart which represents the non-seal classifications associated with each laser operational condition.

5.2.1 An Examination of Non-Seal Modes and their Relation to the Overall Seal Rate

Figure 5.6A demonstrates a sharp rise in the seal rate when average power is increased from 1.22 W to 2.383 W. Following this the seal rate declines nearly monotonously with increasing average power. At 1.22 W all five vessels were non-seals and all of these non-seal modes were deemed unaffected by DS-Eval. This suggests that at 1.22 W and 0.03 mm^2 the irradiance is insufficient to seal a vessel. That is, there is insufficient energy delivered per unit time per unit area to the tissue to elicit a significant effect. The decrease in seal rate with increasing average power beyond 2.38 W can be attributed to the increasing rupture rate. A rupture occurs when an excess of energy is deposited locally thereby causing extreme mechanical forces resulting in vessel rupture. It follows then that irradiance should be directly proportional to the rupture rate, a conclusion that is bolstered by the findings of [98]. This relationship is expressed in Figure 5.6A where, given that spot size is constant, average powers of 2.83 W, 3.01 W, and 4.6 W resulted in rupture rates of 50%, 75%, and 80%. Thus, it is likely that there was no observable trend between seal rate and average power in Figure 5.6A because the irradiance at 1.22 W was insufficient to elicit an effect in vessels and powers greater than 2.383 W resulted in irradiances which triggered rupture. This trend of a high rupture rate in response to high irradiances is also visible in Figure 5.6C where the single outlier in this plot features the highest irradiance and results in 4/5 non-seal modes being ruptures. Further, by comparing Figure 5.6A and B, the reader will notice that no ruptures occurred in B and that the average seal rate in B is higher than that of A. This is may also attributable to the decrease in irradiance across all power levels from Figure 5.6A to B, since the only difference between plots A and B are a change in spot size from 0.03 mm^2 to 0.04 mm^2 respectively.

Again, referring to Figure 5.6A and B, it is apparent that the irradiance of Figure 5.6B resulted in more partial seals and unaffected non-seal modes. By DS-Eval an unaffected result is declared when there is less than 10% change in vessel diameter and less than 15% change in Doppler signal area. This lack of a change in either biological parameter is an indicator that insufficient energy reached the entire vessel since tissue coagulation is achieved when a unit of tissue reaches the denaturation temperature of 60 C (see Section 2.3.2). Similarly, since partial seals occur when only a portion of the vessel has been denatured, it can be concluded that partial seals are the result of insufficient energy reaching a portion of the vessel (see Figure 4.6). Since there is a decrease in irradiance from Figure 5.6A to B, the lack of ruptures and the increase in unaffected and partial seal outcomes is therefore expected. A similar trend is observed in Figure 5.6D where, as the

irradiance decreases, the percentage of unaffected non-seal modes increases with the exception of the data point at 0.06 mm^2. By comparing Figure 5.6C and D and ignoring the outliers it is evident that there are more unaffected outcomes in D than in C while C features more partial seal outcomes in comparison to D. It is therefore reasonable to conclude that the lack of a consistent trend between spot size and the seal rate in Figure 5.6C and D is due to the change in irradiance between the two plots resulting in different non seal modes.

While non-seal modes offer a partial explanation to the lack of a trend between laser operational parameters and the seal rate they do not account for all observed results. For example, following from the above discussion, increasing irradiance should result in an increase in the rupture rate. This is not observed in Figure 5.6E-F where irradiance remains constant within each plot and rupture rates vary between 0% and 100%. Additionally, the total number of ruptures increases from 7 to 8 when irradiance is decreased from Figure 5.6E to F which also counters the expected outcome. As a result, there must be additional causation to the lack of an observable trend, and it is likely that this is primarily a result of biological factors.

5.2.2 The Effect of Biological Factors on the Seal Rate

Biological factors have a significant effect on seal rate. The mean vessel diameter of all vessels in this study was 0.50 ± 0.16 mm. The mean vessel diameter for all non-seal outcomes was significantly higher than the mean diameter for all seal outcomes (566 µm and 469 µm respectively, $p = 0.0007$, Mann-Whitney U-test). From a heuristic perspective, this is a sound finding as larger vessels would hypothetically require more energy to seal. However, it is believed that this finding is a result of vessel size increasing well beyond the spot size of the laser (206 µm). This would result in a less uniform thermal energy deposition laterally across the vessel and subsequently non-uniform mechanical expansion of the vessel resulting in rupture; analogous to glass shattering in response to localized heating. Laterally this problem could be addressed by sweeping the beam across the vessel or using a collimated beam that is at least as large as the lateral diameter of the vessel. If the absorption coefficient of tissue is approximated to that of water at 1942 nm ($\sim 10^4$ /m), then the optical penetration depth is ~ 100 µm. This leads to a similar conclusion axially, where, vessels whose axial diameters are far greater than the optical penetration depth will also realize non-uniform heating axially potentially resulting in rupture. This theory unveils a potential limitation for contactless vessel sealing using the Tm^{3+} fiber laser where the

size of the vessel that can be sealed is hypothetically limited by the optical penetration depth, an idea that directly relates to the findings of [94].

Vessel depth, the axial distance between the surface of the CAM and the most superficial portion of the vessel wall, should have also influenced the seal rate given the limitation posed by the optical penetration depth. Vessels deeper than 100 µm would receive at most 37% of the incident irradiation. All other heat reaching a deep vessel would predominantly be a result of thermal energy propagation through the tissue. Given this, it stands to reason that the vessel depth should have influenced the seal rate, however no significant correlation was found between mean vessel depth for both seal and non-seal outcomes where the mean vessel depth was 150 µm and 151 µm respectively (p = 0.96, two sample t-test). Recall, that when implementing DS-Eval, for a vessel to be considered viable, the diameter of the vessel must have been small enough to fit mostly within the imaging field (see Section 4.1.1). This directly extends to vessels depths, as, if the vessel was too deep it would also be outside of the OCT imaging field regardless of the diameter. This meaning that it is possible that an insufficient range of depths were included in this study to detect a significant relationship, bolstered by the relatively shallow average depths. It is also worthwhile to note that if the average vessel depth was ~150 µm then most vessels that did seal sealed mostly as a result of thermal energy diffusion and not as a result of optical to thermal energy conversion.

Tissue dehydration tends to be a prominent factor in most laser tissue interaction studies where a hydrolytic laser is used [12,13,124,125]. It was also believed to be a prominent factor here. Acquisition time of each data point was approximately 15 min, the specimen had to be maneuvered into the imaging field of the OCT beam and a total of ~200 B-scans (including pre and post scans) were acquired at 6 B-Scans/second. In some cases, bulk movement of the embryo caused motion artifacts in the acquired Doppler images while structural images were plagued by brightness artifacts, requiring a rescan of the vessel. All of these factors combined attributed to a prolonged exposure of each embryo to open air resulting in dehydration, where, dehydration is clearly visible in the CAM as it progresses from being initially translucent to opaque. Two methods were used to maintain the hydration of the membrane. In phase one of the experiment, the CAM was dabbed with Kim Wipes which had been moistened with saline solution. This however only resulted in temporary hydration. Also, excess saline added to the surface of the membrane, at times, seemed

to have influenced the interaction between the 1942 nm laser and vessels; reactions tended to be explosive as the added saline would absorb incident irradiation quite readily. As a result, in phase two of the experiment (discussed later), a new method was implemented where a thin layer of vegetable oil was used, an idea adapted from [126]. The oil was evenly distributed over the surface of the CAM membrane sealing it from open air. In a preliminary experiment it was ensured that the oil was completely inert to 1942 nm irradiation while the thickness of the oil layer was minimized via OCT structural imaging in order to reduce the effects of scattering. This technique was certainly an improvement over saline dabbing however in the long-term dehydration still occurred. The oil also caused a significant increase in brightness artifacts observed in the OCT images at times making it impossible to acquire a clean image without relocating to a different cross section of the vessel further increasing data point acquisition time. Some may argue that CAM dehydration could have been avoided by conducting laser coagulation in a closed humidity regulated environment. However, this would result in significant attenuation of the beam as it passed through free space given its high absorption in water. Additionally, high humidity would also increase the chances of condensation on any optical lenses severely jeopardizing the system.

Given the evident biasing of results due to varying vessel diameter as well as the apparent contributions of tissue dehydration, it is sound to believe that the lack of observable trends in Figure 5.6 could largely be a result of uncontrolled biological parameters. It should be noted that there was reasoning for not controlling for vessel diameter. In any given neurosurgical scenario, a range of vessel diameters would be encountered. For example, in the case of a craniotomy for the resection of a meningioma, the average vessel size supplying the meningioma varies between 0.5 to 2 mm (according to multiple trained neurovascular surgeons). The depth at which these vessels existed would also vary. Thus, in order to effectively evaluate the hemostatic capability of the Thulium laser, both vessel size and depth were not controlled for.

5.2.3 An Analysis of the Sample Size

For each laser operational condition, a total of 5 vessels were irradiated. This number was chosen firstly such that results could be comparable to results produced by Burns in [100] and also because it is within the range of commonly used sample sizes amongst laser sealing literature [97,98]. A seal was designated as a '1' while a non-seal was designated as a '0'. By taking the mean and multiplying by 100 the seal rate achieved across all five vessels was acquired as a percentage. To

study the effects of varying laser parameters on the seal rate, 4 seal rates were acquired at 4 distinct values of the parameter being varied, where the seal rate is the dependent variable. If a minimum coefficient of determination of $r^2 = 0.2$ is sought between each of parameters varied and seal rate, then the required sample sizes for a statistical power of 80% can be acquired. Using G*Power the sample size was calculated to be 33. Given that 5 vessels are required to generate a single seal rate for a given laser operational condition, the total number of vessels required for a single parameter variation would be 165. Further, given the variability of the data acquired in this study it is believed that the actual r^2 will be much smaller than 0.2. For an r^2 of 0.1 the required number of vessels for a single parameter variation jumps to 355. A study of this magnitude would require the sacrifice of an estimated 1900 egg embryos if the same amount of parameter variations studied here were observed. The study would have to be conducted over the course of several years given that data collection in this study required 8 months. Considering the overall seal rate of 29% observed in this study it is not clear that conducting such a study would be worthwhile. Far better results have been achieved with photoangiolytic lasers [98].

5.3 Collateral Thermal Damage Induced by the Thulium Fiber Laser

Measuring the HAZ was generally straight forward although tedious. During the course of the experiment there were cases where the position of the camera had to be moved for practical reasons. As a result, there were some data points where the zoom of the pre and post photographs significantly differed. This presented an issue given that the HAZ measurement methodology depended on determining the distance per photograph pixel. Common features between the pre and post photographs were used to compensate for the difference in zoom. The post photograph distance per pixel ($d_{PostPix}$) was therefore determined by:

$$d_{PostPix} = d_{PrePix} \frac{Pre\ Feature\ Length}{Post\ Feature\ Length} \tag{2}$$

where d_{PrePix} is the distance per pre photograph pixel. The overall process for HAZ measurement given different pre and post photograph zooms is illustrated in Figure 5.7.
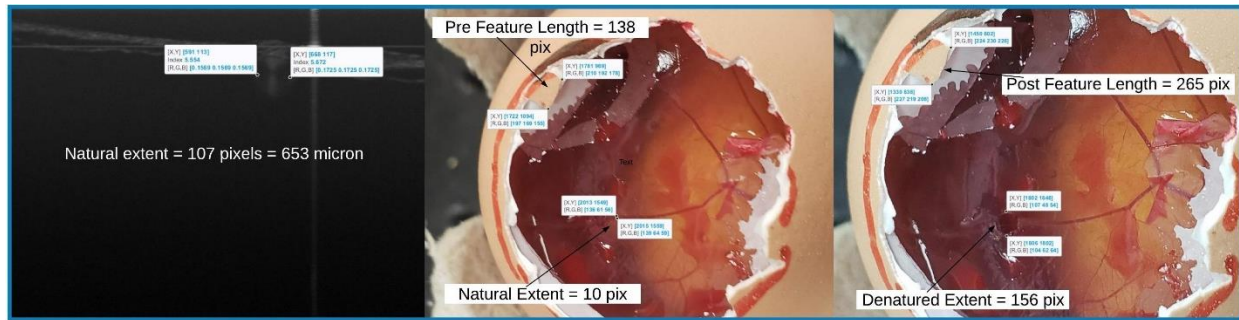
Figure 5.7 Process for measuring HAZ when pre and post images have different zooms. The natural extent of the vessel is obtained in micron from the pre-irradiation OCT structural image and in pixels from the pre-irradiation photograph. $d_{PostPix}$ is then acquired from d_{PrePix} by using the ratio of feature lengths. In this case $d_{PrePix} = 653/10$ µm and $d_{PostPix} = (653/10)*(138/265)$. The denatured extent is therefore 156* $d_{PostPix} = 5491$ µm and therefore the HAZ is $5941 - 653 = 4838$ µm. Dots represent pixels for which data is being displayed.

The average HAZ across all seal data points (n = 30) was 2.2 ± 1.1 mm which is typical of hydrolytic lasers [12,17,19–21]. Most reported HAZ data in the literature concerning the interaction between hydrolytic lasers and tissue has been collected from ablation-based studies. Thus, this result confirms that the HAZ generated by the Thulium laser is consistent regardless of the mode of interaction (within the thermal regime). The average HAZ reported here is much smaller than the 4 mm or greater typically produced by advanced bipolar forceps. This confirms original justifications proposed for using the Thulium laser as a hemostatic instrument, particularly in neurosurgery, on the basis that less collateral damage will be produced, and more neurons will be spared. Burns in [100] reported much smaller HAZ's in using the Thulium laser for vessel sealing where the maximum HAZ was 710 µm. The exact spot size used is not clear since Thulium laser light was delivered from a point source of unknown aperture. Further, this means that diffuse radiation was used rather than focused radiation possibly altering the interaction. Thus, it is difficult to compare results. In comparison to angiolytic lasers, such as those used by Kimel in [47,73], the HAZ here is significantly greater. Although HAZ was not measured directly in those studies it is evident from the various photographs provided that nearly no collateral damage is induced. This, of course, is because angiolytic lasers are only absorbed by blood. While this selective absorption may seem advantageous in terms of reducing HAZ, angiolytic lasers have demonstrated varying effects in the sealing of arteries and veins due to the different absorption coefficients for oxygenated and deoxygenated hemoglobin (see Figure 2.5). Additionally, angiolytic lasers penetrate deeper into tissue since they are not readily absorbed by water possibly jeopardizing deeper tissue structures [127].

There was an observable trend between HAZ and laser operational parameters. Since the HAZ was only acquired for seal data points laser operational parameters were combined into irradiance (average power/spot size) and total energy delivered (average power*exposure time). Figure 5.8 shows the relationship between irradiance and HAZ.
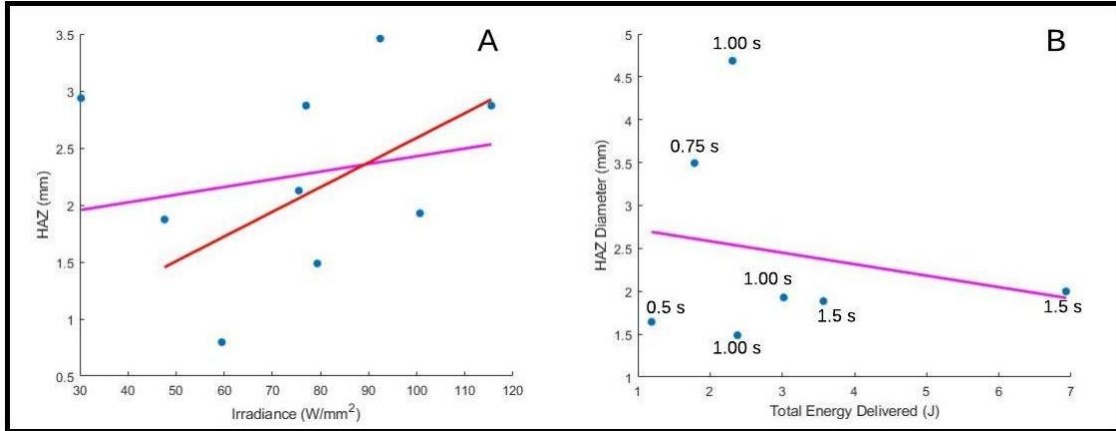
Figure 5.8 Irradiance versus HAZ (A). Total energy delivered versus HAZ (B). Only laser operational conditions where the exposure time was 1 second were included in A. Similarly, only conditions where spot size was 0.03 mm^2 were included in B. This was done to limit the influence of uncontrolled parameters. Each marker represents the average HAZ for the given laser operational condition. Purple lines of best fit include all points where as the red line of best fit excludes the outlier at 30 W/mm^2.

The trends of Figure 5.8 can be attributed to thermal relaxation. The HAZ increases with increasing irradiance because energy is being delivered at an increasingly higher rate within a given tissue area and thus tissue is not allowed to cool (thermally relax). The HAZ decreases as the total energy delivered increases because, although there is more energy delivered, the time span over which this occurs is longer allowing for tissue to cool. For clarity, the exposure time associated with each marker is labeled in Figure 5.8B.

The importance of the HAZ goes beyond measuring collateral thermal damage. The 2.2 ± 1.1 mm average diameter of the HAZ demonstrates that sufficient thermal energy diffused beyond the optical zone (see Section 2.3.1) to coagulate tissue within a ~1 to 3 mm diameter. This proves exactly that the thermal diffusion in tissue at the laser operational parameters used here was sufficient to induce coagulation at the extents of vessels encountered in this study. This is why seals were achieved in this study despite the fact that the optical penetration depth and spot size were 100 µm and 206 µm respectively. This is of course assuming that the lateral thermal energy spread observed at the surface is indicative of the same in the depth dimension, which if we consider tissue to be homogenous at this scale is a valid assumption. Given that all exposure times

83

used here were well above the thermal relaxation time, thermal confinement was certainly not met. However, this only proves that energy will not be contained within the optical zone. Thus, the HAZ serves as an indicator of the extents to which coagulation can be achieved using the Thulium laser and subsequently the maximum vessel size that can theoretically be sealed.

5.4 Determining the Seal rate Under a Dose-Until-Sealed Treatment

In phase two of the study, a more realistic surgical scenario was emulated wherein a surgeon encounters a vessel that needs to be sealed. In this case the surgeon would continuously attempt to seal the vessel until it can be reasonably concluded that the vessel has been sealed. Thus, in this case vessels were subjected to continuous doses of 1942 nm irradiation until declared sealed by DS-Eval. In this way 9 ± 3 doses were required to seal each vessel where a single dose is a 1 second exposure at 2.38 W and 0.03 mm^2. This laser operational condition was selected as it was one of three conditions which demonstrated the highest seal rate of 60% in phase 1. Of the 18 vessels irradiated in this experiment 17 sealed. The single vessel that did not seal was an irreparable rupture. While the overall seal rate in this case was 94.4% the average therapeutic time for sealing a vessel was 9 ± 3 s much longer than the time reported by Rees et al in [97]. However, outcomes in this study were subjected to far more stringent testing given that visual examination was used in [97]. Typically, the first dose resulted in vessel rupture (as was expected given the results of phase 1) and thus subsequent doses were required to repair the rupture and ultimately stem the flow of blood. Additionally, after tissue had been partially coagulated the laser became less effective and this is believed to be a result of dynamic changes in the absorption coefficient (see Section 2.3.2). It is believed that these two factors were the primary contributors to the extended therapeutic time. There were some cases here where the vessel appeared to have sealed, yet DS-Eval revealed residual flow meaning that further doses were required to completely seal the vessel (Figure 5.9). This process is very similar to actions taken by surgeons in intracerebral surgical procedures where a vessel is "sealed" and then the seal is verified via CT angiography. The influence of biological factors was incredibly evident. At times, embryonic fluid would pool over the CAM in the vicinity of the targeted vessel requiring additional doses to achieve a seal. Additionally, movement of the embryo would occasionally cause the vessel to shift out of the focal point of the Tm^{3+} laser requiring repositioning. This gives valuable foresight as to a potential issue in the implementation of hydrolytic lasers in a contactless fashion. In realistic surgical scenarios

the profusion of saline over tissue (or any excess surface moisture) may inhibit the lasers therapeutic effect.
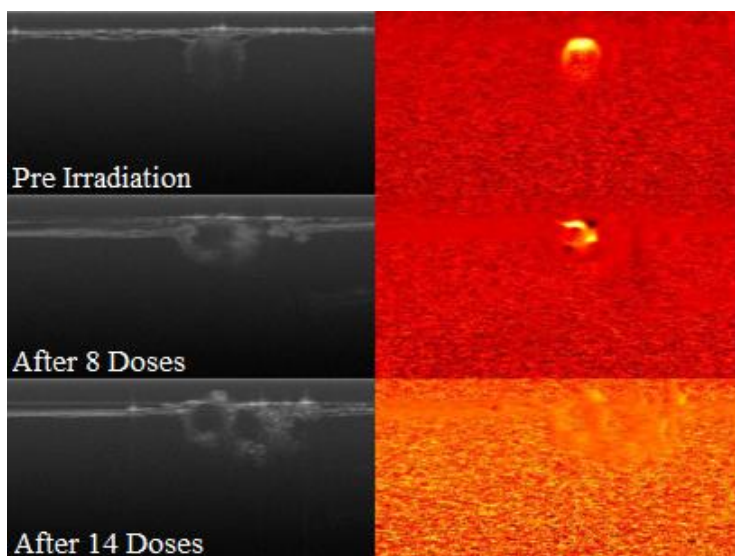
Figure 5.9. Doppler imaging as part of DS-Eval reveals residual flow despite the vessel being significantly denatured. To the naked eye this vessel appeared to have sealed after 8 doses. Top most images are pre-irradiation, middle after 8 doses, and bottom after 14 doses.

5.5 Final Remarks Concerning the Hemostatic Potential of the Thulium Laser

Despite the many theoretical benefits of using the Thulium laser as a hemostatic instrument, results in this study suggest that it may not be suitable for this purpose. Given the overall seal rate, and the prevalence of the rupture outcome, the overly violent interactions between Thulium laser light and vascular tissue reported by [94,100] are well founded. Further, the lack of a trend between the seal rate and laser operational parameters observed here supports the generally unpredictable nature associated with many laser-tissue interactions. While this does paint a bleak picture for the future of the Thulium laser in hemostatic applications, it is believed that the lack of predictability of laser with tissue is common across many laser-tissue pairings [128]. For example, Broadhurst in [98] conducted a study which observed the effects of 532 nm KTP laser (which is angiolytic) on vascular tissue. Of 18 laser operational conditions studied where spot size, laser energy, and pulse width were varied, only the results (rupture rates) of 8 laser operational conditions were reported. Each of the conditions reported demonstrated clear trends between rupture rate and laser operational conditions. This leads one to believe that the remaining conditions were excluded because they did not demonstrate the expected relationships. When a dose-until-seal methodology was adopted the overall seal rate was 94.4%. While this is promising the average therapeutic time

was 9 ± 3 s which is highly impractical for surgical implementation. All things considered, given the observations of this study, the Thulium laser is not recommended for use in hemostatic applications under the conditions observed here.

The CAM membrane may have been unsuitable model for this study. While the model does offer cponvenient and rapid access to functioning arteries the overall lack of mechanical stability may have resulted in increased rupture rates. There is evidence that suggests that the ablation threshold is related to tissue UTS [129]. Since ablation is ultimately what triggers rupture, the mechanical strength of tissue should have a direct effect on the seal rate. Human vasculature is anchored to the tissue bulk via the tunica adventitia (see Section 2.2.2) thus it is possible that human vessels would be more resistant to rupture. The lack of mechanical stability of the CAM model is an issue that has been raised in [100].

Chapter 6: Conclusions and Future Work

The DS-Eval methodology developed in Chapter 4 has the potential to be an indispensable tool for the evaluation of laser-based surgical systems. Given this, its use can be extended beyond the evaluation of laser surgical systems. For example, the micron level resolution structural feedback afforded by this methodology could be used to observe laser-tissue coagulation or ablation dynamically. This would help in understanding the exact biological responses that facilitate both ablation and coagulation. Doppler feedback from DS-Eval could be used in the study of dynamic nature of energy seals. While there is extensive literature studying a laser's ability to induce an energy seal, the author of this work has not found any literature which studies these seals over extended periods of time. It would be interesting to study these seals over extended periods of time to determine if the hemostatic results achieved initially hold over time. This work would be especially crucial in the study of contactless energy seals where compression is not implemented.

While the results reported in Chapter 5 generally indicate that the Thulium Laser is not suitable for hemostasis, the fact that a seal rate of 95% was achieved under a dose until sealed approach warrants further investigation. Additionally, it should be noted that the average seal rate of 29% was achieved while searching for an ideal combination of laser parameters. As a result, it is likely that the average seal rate was lessened by laser operational conditions which were unsuitable for hemostasis. If only conditions where the maximum seal rate of 60% are considered, then the overall performance of the laser seems considerably better, although still significantly below what has been achieved by photoangiolytic lasers [73,98]. It should be noted that there are several factors which were not considered in this work that could potentially improve on performance. In laser material processing, particularly in laser welding, there are two desired effects: cutting and welding. If we consider these two effects to be somewhat analogous to ablation and coagulation, then some comparisons can be made. In laser machining, whether the laser welds or cuts is partially regulated by dynamically modulating the power delivery [130]. This is an approach that was not studied here. For example, the Thulium laser tended to induce rupture upon initial interaction, this suggests that initial power levels were too high. If power delivery was modulated such that it steadily increased over the designated exposure time then it is possible that some improvements to the seal rate could have been realized.

If the overall rupture rate of 30% is attributed to high thermal energy gradients produced by the laser, then it is possible that rupture rates can be reduced by using a collimated beam with a larger spot size. This would require a slight change in the layout of the optical payload specifically requiring that the OCT beam is focused before passing through the DCM such that the Tm^{3+} beam is not focused. For the purposes of hemostasis, it seems that this would be ideal, however, this would limit the functionality of the overall system since an unfocused beam would most likely lack the irradiance to induce ablation. This would have counteracted one of the original premises for evaluating the hemostatic potential of the Thulium laser: "if a single laser can be tuned for the purposes of ablation and hemostasis, then a single instrument could be used across all tissue types". An alternative technological solution would be to add a second set of scanning galvos to the high-powered beam arm of the payload. By rapidly scanning the beam across the lateral extents of the vessel, a more uniform lateral thermal energy deposition could be achieved. Since the galvo system could easily be controlled to either produce a stationary beam or sweeping beam, then theoretically both hemostasis and ablation could be achieved. Modifying the mode of beam delivery, either by using an unfocused collimated beam or by beam sweeping, could potentially alleviate high lateral thermal energy gradients but would not provide a solution axially. Thus, overall, the seal rate could potentially be improved but would still be limited due to the shallow OPD of the laser.

In terms of energy sealing, the best results to-date have been demonstrated by angiolytic lasers however, in most of these cases, the hemostatic capabilities of these lasers were evaluated visually. A useful future study would be to evaluate the hemostatic potential of these lasers via DS-Eval. If results were found to be consistent with current reports in the literature, then it would be interesting to develop a dual wavelength surgical instrument. By incorporating both a hydrolytic laser (such as the Thulium laser) and an angiolytic laser (such as the KTP laser), then both ablation and hemostasis could potentially be achieved across several tissue types.

Appendix

MATLAB code for post-processing (eggTrial11 Data Process). The same code was used for each data acquisition trial and therefore it is unnecessary to include the scripts for each.

```matlab
%%%%Post Processing Egg Trial 11

%Array of file names corresponding to each of the data points in eggTrial11.
% FORMAT DATAPOINT_PRE|POST|UP, where ups were acquired in cases where
% ruptures could not be completely verified
vesselName = ["A_pre.bin", "A_post.bin", "B_pre.bin", "B_post.bin", "C_pre.bin", "C_post.bin", "D_pre.bin", "D_post.bin", "E_pre.bin", "E_post.bin", "F_pre.bin", "F_post.
"J_pre.bin", "J_post.bin", "K_pre.bin", "K_post.bin", "L_pre.bin", "L_post.bin", "M_pre.bin", "M_post.bin", "N_pre.bin", "N_post.bin", "O_pre.bin", "O
"S_pre.bin", "S_up.bin", "T_pre.bin", "T_up.bin", "U_pre.bin", "U_up.bin", "V_pre.bin", "V_up.bin", "W_pre.bin", "W_up.bin", "X_pre.bin", "X_post
"l_pre.bin", "l_post.bin"];

h = gobjects(27, 4); %%there are 27 data points in eggTrial11 A-Z + 1

vesselFigName = ["egg11_A", "egg11_B", "egg11_C", "egg11_D", "egg11_E", "egg11_F", "egg11_G", "egg11_H", "egg11_I", "egg11_J", "egg11_K", "egg11_L", "egg11_M", "egg11_N"
vesselFigNum = 1;
%%BASIC OCT PROCESSING Universal Definitions
x=1:1024;
la = 1180.89+0.2268*x-8.2e-6*x.^2-6.99e-9*x.^3; %function representing wavelength in terms of vertical pixel position
k0=2*pi/la; %%Corresponding function in K-Space
k1=2*pi/min(la); %%%maximum and minimum wavenumbers for linearizing pixel to K-Space
k2=2*pi/max(la);

%%Pre Allocation for speed
y = zeros(1024, 1000);
k = zeros(1, 1024);

%%linearize k0 and generate evenly spaced query points for interpolation
for n=1:1024
    k(n)=k2+(n-1)*(k1-k2)/1023;
end

%%Main processing loop, groups pre and post data sets consisting of ~100 B-Scans each, hence iteration by 2
for VN = 1:2:size(vesselName, 2)-1
    [h(VN, :), pos] = tight_subplot(2,2,[0 0],[0 0],[0 0]); %initialize tight subplot object

    fid = fopen(vesselName(VN)); %extract data from .bin
    ys = fread(fid,'int16');
    fclose all;

    %B-Scans were 1000*1024, where each A-line was 1024 values in length, only half of the A-line content is used.
    %floor() is necessary since in some cases a non-integer number of
    %Bscans were acquired
    numberBs = floor(length(ys)/1024000);

    cDATA = zeros(512, 1000, numberBs); %pre allocate for speed. Although cDATA is used this is not a true c-scan given that all 100 B's
                                        %are acquired in the same
                                        %cross-section.
```

```matlab
        %are acquired in the same
        %cross-section.


%%%Pre Image OCT processing loop, every iteration of the loop processes one B-Scan
for jam = 0:(numberBs -1)
    bscan=ys((1+jam*1024000):(jam*1024000+1024000));
    %Organize data from string of values into frame 1024x1000 (row x column)
    IO = reshape(bscan, [1024,1000]);
    %DC Subtraction
    DC=mean(IO,2);
    M = IO-DC;
    %Interpolation
    for i=1:1000
        y(:,i)=interp1(KO,M(:,i),k,'linear');
    end
    %%Fourier Trnsform
    c = fft(y);
    I1 = c(1:512,:);
    %Collect B-Scans into C-Scans
    cDATA(:,:,jam+1) = I1;
end

%Data for doppler Processing includes both real and imaginary parts
dopDATA = cDATA;

%%%Doppler processing
%Generate matrix of complex conjugate multiplication, find phase shifts
conjMat = zeros(512, 999, numberBs);
conjMat(:, 1:end, :) = dopDATA(:, 1:end-1, :).*conj(dopDATA(:, 2:end, :));
%Window Sum. Since significant A-line overlap was used here, A-line
%averaging can be implemented to reduce the influence of speckle
%noise.
sumMat = movsum(conjMat, 3), 20, 2);

%Extract imaginary component, the phase shift
dopler = angle(sumMat);
%For additional speckle reduction the final Doppler image is the average
% of approximately 100 B-scans
dopFINAL = mean(dopler(:,1:end),3);

%StructuralInformation is the real part.
structDATA = log(abs(cDATA));
%Again all B-Scans are averaged
structural = mean(structDATA(:,:,1:end), 3);
```

```matlab
%%Again all B-Scans are averaged
structural = mean(structDATA(:,:,1:end), 3);

%Create Structural image and add scale bar manually
structural(375:493, 50:52) = max(max(structural));
structural(493, 50:150) = max(max(structural));

%Generate pre structural and Doppler Images
axes(h(VN, 1));
imagesc(structural);
set(gca,'visible','off')
set(gca,'Yticklabel',[])
set(gca,'Xticklabel',[])
colormap(h(VN, 1), gray);

axes(h(VN, 2));
imagesc(dopFINAL);
set(gca,'visible','off')
set(gca,'Yticklabel',[])
set(gca,'Xticklabel',[])
colormap(h(VN, 2), hot);

%%%%%%%%%%  Repeated section for the processing of POST images %%%%%

fid = fopen(vesselName(VN+1));
ys = fread(fid,'int16');
numberBs = length(ys)/1024000;

cDATA = zeros(512, 1000, numberBs);

for jam = 0:(numberBs -1)

dopDATA = cDATA;

%%%Find Dopler
%Generate matrix of complex conjugate multiplication
conjMat = zeros(512, 999, numberBs);
conjMat(:, 1:end, :) = dopDATA(:, 1:end-1, :).*conj(dopDATA(:, 2:end, :));

%%Window Sum
sumMat = movsum(conjMat, 3), 20, 2);

%%Dopler
dopler = angle(sumMat);
dopFINAL = mean(dopler(:,:,1:end),3);

%Create Structural image and add scale bar manually
structDATA = log(abs(cDATA));
```

Special Figure References for figures not obtained from peer-reviewed sources

Figure 5.1

- Tissue adherence tonsillectomy https://www.youtube.com/watch?v=lQs6i8Gy_74
- Monopolars http://www.boviemedical.com/2016/10/03/bipolar-electrosurgery-vs-monopolar-electrosurgery/
- Bipolars https://neurosurgical.stryker.com/products/spetzler-malis-disposable-bipolar-forceps/

Figure 2.4-2.5

- *A special thanks to Scott Prahl for accumulating absorption spectra for various biological tissues and making this data publicly available.*

References

1.   J. L. O'Connor and D. A. Bloom, "William T. Bovie and electrosurgery.," Surgery **119**, 390–396 (1996).

2.   J. Voorhees, A. A. Cohen-Gadol, E. R. Laws, and D. Spencer, "Historical vignette Battling blood loss in neurosurgery : Harvey Cushing ' s embrace of electrosurgery," J. Neurosurg. 745–752 (2005).

3.   A. Shabbir and D. Dargan, "Advancement and benefit of energy sealing in minimally invasive surgery," Asian J. Endosc. Surg. **7**, 95–101 (2014).

4.   N. N. Massarweh, N. Cosgriff, and D. P. Slakey, "Electrosurgery: History, Principles, and Current and Future Uses," J. Am. Coll. Surg. **202**, 520–530 (2006).

5.   M. Siddaiah-Subramanya, K. W. Tiang, and M. Nyandowe, "Complications, Implications, and Prevention of Electrosurgical Injuries: Corner Stone of Diathermy Use for Junior Surgical Trainees," Surg. J. **03**, e148–e153 (2017).

6.   A. J. Choudhry, N. N. Haddad, M. A. Khasawneh, D. C. Cullinane, and M. D. Zielinski, "Surgical Fires and Operative Burns: Lessons Learned From a 33-Year Review of Medical Litigation," Am. J. Surg. **213**, 558–564 (2017).

7.   D. J. Humes, I. Ahmed, and D. N. Lobo, "The Pedicle Effect and Direct Coupling," Arch. Surg. **145**, 96–98 (2010).

8.   K. Wang and A. P. Advincula, ""Current thoughts" in electrosurgery," Int. J. Gynecol. Obstet. **97**, 245–250 (2007).

9.   P. N. Montero, T. N. Robinson, J. S. Weaver, and G. V. Stiegmann, "Insulation failure in laparoscopic instruments," Surg. Endosc. **24**, 462–465 (2010).

10.   S. Huusmann, M. Wolters, M. W. Kramer, T. Bach, H. O. Teichmann, A. Eing, S. Bardosi, and T. R. W. Herrmann, "Tissue damage by laser radiation: an in vitro comparison between Tm:YAG and Ho:YAG laser on a porcine kidney model," Springerplus **5**, 1–9 (2016).

11.   B. Tunc and M. Gulsoy, "Tm:Fiber laser ablation with real-time temperature monitoring

for minimizing collateral thermal damage: Ex vivo dosimetry for ovine brain," Lasers Surg. Med. **45**, 48–56 (2013).

12. T. Bilici, S. Mutlu, H. Kalaycioglu, A. Kurt, A. Sennaroglu, and M. Gulsoy, "Development of a thulium (Tm:YAP) laser system for brain tissue ablation," Lasers Med. Sci. **26**, 699–706 (2011).

13. B. Ozgurun and M. Gülsoy, "Photothermal effect of infrared lasers on ex vivo lamb brain tissues," **1049209**, 9 (2018).

14. G. W. Hruby, F. C. Marruffo, E. Durak, S. M. Collins, P. Pierorazio, P. A. Humphrey, M. M. Mansukhani, and J. Landman, "Evaluation of Surgical Energy Devices for Vessel Sealing and Peripheral Energy Spread in a Porcine Model," J. Urol. **178**, 2689–2693 (2007).

15. G. A. Vilos and C. Rajakumar, "Electrosurgical Generators and Monopolar and Bipolar Electrosurgery," J. Minim. Invasive Gynecol. **20**, 279–287 (2013).

16. W. L. Newcomb, W. W. Hope, T. M. Schmelzer, J. J. Heath, H. J. Norton, A. E. Lincourt, B. T. Heniford, and D. A. Iannitti, "Comparison of blood vessel sealing among new electrosurgical and ultrasonic devices," Surg. Endosc. Other Interv. Tech. **23**, 90–96 (2009).

17. Y. Huang, J. Jivraj, J. Zhou, J. Ramjist, R. Wong, X. Gu, and V. X. D. Yang, "Pulsed and CW adjustable 1942 nm single-mode all-fiber Tm-doped fiber laser system for surgical laser soft tissue ablation applications," Opt. Express **24**, 16674 (2016).

18. M. Gu, "Er : YAG Laser Ablation of Cerebellar and Cerebral Tissue," 40–43 (2001).

19. J. T. Walsh., T. J. Flotte, R. R. Anderson, and T. F. Deutsch, "Pulsed CO2 laser tissue ablation: Effect of tissue type and pulse duration on thermal damage," Lasers Surg. Med. **8**, 108–118 (1988).

20. V. Venugopalan, N. S. Nishioka, and B. B. Mikić, "The Effect of CO2 Laser Pulse Repetition Rate on Tissue Ablation Rate and Thermal Damage," IEEE Trans. Biomed. Eng. **38**, 1049–1052 (1991).

21.   B. Majaron, S. M. Srinivas, H. E. L. Huang, and J. S. Nelson, "Deep coagulation of dermal collagen with repetitive Er:YAG laser irradiation," Lasers Surg. Med. **26**, 215–222 (2000).

22.   M. M. Zaret, G. M. Breinin, H. Schmidt, H. Ripps, I. M. Siegel, and L. R. Solon, "Ocular lesions produced by an optical maser (laser)," Science (80-.). **134**, 1525–1526 (1961).

23.   K. M. Earle, S. Carpenter, U. Rosemann, M. A. Ross, J. R. Hayes, and E. Zeitler, "Central Nervous System Effects of Laser Radiation," Fed. Proc. **24**, SUPPL 14:129+ (1965).

24.   S. Fine and E. Klein, "Biological Effects of Laser Radiation," Adv. Biol. Med. Phys. **10**, 149–226 (1965).

25.   H. L. Rosomoff and F. Carroll, "Reaction of neoplasm and brain to laser.," Arch. Neurol. **14**, 143–8 (1966).

26.   S. Krishnamurthy and S. K. Powers, "Lasers in neurosurgery," Lasers Surg. Med. **15**, 126–167 (1994).

27.   P. W. Ascher and F. Heppner, *Der CO2-Laser in Der Neurochirurgie*, 1. Aufl. (Molden, 1977).

28.   O. J. Beck and F. Frank, "The use of the Nd-YAG laser in neurosurgery," Lasers Surg. Med. **5**, 345–356 (1985).

29.   J. P. Ingimarsson and A. E. Krambeck, "History and development of lasers in the treatment of BPH," in *The History of Technologic Advancements in Urology* (Springer International Publishing, 2017), pp. 97–107.

30.   E. Snitzer, "Optical Maser Action of Nd In A Barium Crown Glass," Phys. Rev. Lett. **7**, 444–446 (1961).

31.   E. Snitzer, "Proposed fiber cavities for optical masers," J. Appl. Phys. **32**, 36–39 (1961).

32.   S. Stokowski, R. Saroyan, and M. Weber, *Nd-Doped Laser Glass Spectroscopic and Physical Properties* (1978).

33.   J. Dong, M. Bass, and C. Walters, "Temperature-dependent stimulated-emission cross

section and concentration quenching in Nd^3+-doped phosphate glasses," J. Opt. Soc. Am. B **21**, 454 (2004).

34.   V. Ter-Mikirtychev, *Springer Series in Optical Sciences: Fundamentals of Fiber Lasers and Fiber Amplifiers* (2014).

35.   H. Tran and D. E. Chung, "Thulium Laser Prostatectomy," in *A Comprehensive Guide to the Prostate* (Elsevier, 2018), pp. 81–97.

36.   N. M. Fried and K. E. Murray, "New technologies in endourology: High-power thulium fiber laser ablation of urinary tissues at 1.94 μm," J. Endourol. **19**, 25–31 (2005).

37.   S. D. Jackson, "The spectroscopic and energy transfer characteristics of the rare earth ions used for silicate glass fibre lasers operating in the shortwave infrared," Laser Photonics Rev. **3**, 466–482 (2009).

38.   P. F. Moulton, G. A. Rines, E. V. Slobodtchikov, K. F. Wall, G. Frith, B. Samson, and A. L. G. Carter, "Tm-doped fiber lasers: Fundamentals and power scaling," IEEE J. Sel. Top. Quantum Electron. **15**, 85–92 (2009).

39.   S. D. Jackson, "Cross relaxation and energy transfer upconversion processes relevant to the functioning of 2 μm Tm3+-doped silica fibre lasers," Opt. Commun. **230**, 197–203 (2004).

40.   M. Tao, Q. Huang, T. Yu, P. Yang, W. Chen, and X. Ye, "Cross relaxation in Tm-doped fiber lasers," 2nd Int. Symp. Laser Interact. with Matter (LIMIS 2012) **8796**, 87961W (2013).

41.   S. O. Kasap, "Optoelectronics & Photonics:Principles & Practices: International Edition (Photocopy)," 544 (2013).

42.   C. Vanputte, R. Seeley, T. Stephens, and P. Tate, *Seeley's Anatomy & Physiology.* (McGraw-Hill College, 2016).

43.   A. Jabs, "Determination of Secondary Structure in Proteins by FTIR Spectroscopy - JenaLib," http://jenalib.leibniz-fli.de/ImgLibDoc/ftir/IMAGE_FTIR.html.

44.   A. Vogel and V. Venugopalan, "Mechanisms of Pulsed Laser Ablation of Biological

Tissues," Chem. Rev. **103**, 577–644 (2003).

45.   I. V. Yannas, "Collagen and Gelatin in the Solid State," J. Macromol. Sci. Part C **7**, 49–106 (1972).

46.   J. L. R. Arrondo, A. Muga, J. Castresana, and F. M. Goñi, "Quantitative studies of the structure of proteins in solution by fourier-transform infrared spectroscopy," Prog. Biophys. Mol. Biol. **59**, 23–56 (1993).

47.   S. Kimel, L. O. Svaasand, D. Cao, M. J. Hammer-Wilson, and J. Stuart Nelson, "Vascular response to laser photothermolysis as a function of pulse duration, vessel type, and diameter: Implications for port wine stain laser therapy," Lasers Surg. Med. **30**, 160–169 (2002).

48.   S. Prahl, "Optical Absorption of Hemoglobin," https://omlc.org/spectra/hemoglobin/.

49.   F. E. Davis, K. Kenyon, and J. Kirk, "A Rapid Titrimetric Method for Determining the Water Content of Human Blood Author (s): F . E . Davis , Keith Kenyon , Jack Kirk Published by : American Association for the Advancement of Science Stable URL : http://www.jstor.org/stable/1680527 A Rapid," Adv. Sci. **118**, 276–277 (1953).

50.   G. M. Hale and M. R. Querry, "Optical Constants of Water in the 200 nm to 200 um Wavelength Region," Appl. Opt. **12**, 555–563 (1973).

51.   T. Matsumoto, S. Sugita, and T. Yaguchi, "Biomechanics of Blood Vessels: Structure, Mechanics, and Adaptation," in (Springer, Berlin, Heidelberg, 2015), pp. 71–98.

52.   G. A. Holzapfel, "BIOMECH PREPRINT SERIES Biomechanics of Soft Tissue," Handb. Mater. Behav. **Paper No.**, (2000).

53.   M. A. Meyers, P. Y. Chen, A. Y. M. Lin, and Y. Seki, "Biological materials: Structure and mechanical properties," Prog. Mater. Sci. **53**, 1–206 (2008).

54.   A. J. Schriefl, G. Zeindlinger, D. M. Pierce, P. Regitnig, and G. A. Holzapfel, "Determination of the layer-specific distributed collagen fibre orientations in human thoracic and abdominal aortas and common iliac arteries," J. R. Soc. Interface **9**, 1275–1286 (2012).

55. J. E. Mark, *Polymer Data Handbook* (1999).

56. T. Matsumoto and K. Nagayama, "Tensile properties of vascular smooth muscle cells: Bridging vascular and cellular biomechanics," J. Biomech. **45**, 745–755 (2012).

57. K. NAGAYAMA and T. MATSUMOTO, "Mechanical Anisotropy of Rat Aortic Smooth Muscle Cells Decreases with Their Contraction (Possible Effect of Actin Filament Orientation)," JSME Int. J. Ser. C **47**, 985–991 (2005).

58. S. Deguchi, T. Ohashi, and M. Sato, "Tensile properties of single stress fibers isolated from cultured vascular smooth muscle cells," J. Biomech. **39**, 2603–2610 (2006).

59. M. H. Niemz, "Introduction," in *Laser-Tissue Interactions* (Springer Berlin Heidelberg, 2002), pp. 1–7.

60. A. Mehta, "Ultraviolet-Visible (UV-Vis) Spectroscopy – Limitations and Deviations of Beer-Lambert's Law | Analytical Chemistry | PharmaXChange.info," https://pharmaxchange.info/2012/05/ultraviolet-visible-uv-vis-spectroscopy-–-limitations-and-deviations-of-beer-lambert-law/.

61. A. J. Welch and M. J. C. van Gemert, *Optical Thermal Response of Laser Irradiated Tissue*, 2nd ed. (Springer International Publishing, 2010).

62. S. L. Jacques, "Role of tissue optics and pulse duration on tissue effects during high-power laser irradiation," Appl. Opt. **32**, 2447 (1993).

63. R. R. Anderson and J. A. Parrish, "Selective Photothermolysis : Precise Microsurgery by Selective Absorption of Pulsed Radiation Published by : American Association for the Advancement of Science Stable URL : http://www.jstor.org/stable/1690495 Selective Photothermolysis : Precise Microsur," Adv. Sci. **220**, 524–527 (1983).

64. K. R. Holmes, "Thermal Properties," Unpublished (n.d.).

65. D. Jansen, T. G. Van Leeuwen, M. Motamedi, C. Borst, and A. J. Welch, "Temperature dependence of the absorption coefficient of water for midinfrared laser radiation," Lasers Surg. Med. **14**, 258–268 (1994).

66. L. M. Jiji, *Jiji, Heat Conduction*, 3rd ed. (Springer International Publishing, 2009).

67.   A. R. Moritz and F. C. Henriques, "Studies of Thermal Injury Part I: The conduction of heat to and through skin and the temperatures attained therein. A theoretical and an experimental investigation," Am. J. Pathol. 531–549 (1946).

68.   A. L. Mckenzie, C. T. W. Lahaye, M. J. C. Van Gemert, M. J. C. Van Gemert, W. J. A. De Kleijn, J. P. H. Henning, A. L. Mckenzie, C. Sturesson, J. W. Pickering, P. H. Butler, A. L. Mckenzie, A. Kienle, and R. Hibst, "Physics of thermal processes in laser-tissue interaction," (n.d.).

69.   J. W. Pickering, "Optical property changes as a result of protein denature in albumen and yolk," **16**, 101–111 (1992).

70.   K. T. Schomacker, Y. Domankevitz, T. J. Flotte, and T. F. Deutsch, "Co:MgF2 laser ablation of tissue: Effect of wavelength on ablation threshold and thermal damage," Lasers Surg. Med. **11**, 141–151 (1991).

71.   B. I. Lange, T. Brendel, and G. Hüttmann, "Temperature dependence of light absorption in water at holmium and thulium laser wavelengths," Appl. Opt. **41**, 5797 (2002).

72.   I. F. Cilesiz and A. J. Welch, "Light dosimetry : effects of dehydration and thermal damage on the optical properties of the human aorta," **32**, (1993).

73.   S. Kimel, T. E. Milner, J. S. Nelson, M. W. Berns, M. Hammer-Wilson, L. O. Svaasand, and M. J. Schell, "Differential Vascular Response to Laser Photothermolysis," J. Invest. Dermatol. **103**, 693–700 (1994).

74.   I. Apitz and A. Vogel, "Material ejection in nanosecond Er : YAG laser ablation of water , liver , and skin," **338**, 329–338 (2005).

75.   G. J. Derbyshire, D. K. Bogen, and M. Unger, "Thermally induced optical property changes in myocardium at 1.06 μm," Lasers Surg. Med. **10**, 28–34 (1990).

76.   A. J. Welch, J. H. Torres, and W. Cheong, "Laser Physics and Laser-Tissue Interaction," Texas Institue J. **16**, 141–149 (1989).

77.   B. C. Wilson and S. L. Jacques, "Optical Reflectance and Transmittance of Tissues : Principles and Applications," **26**, (1990).

78.   W. Lin, M. Motamedi, and A. J. Welch, "Dynamics of tissue optics during laser heating of turbid media," **35**, 3413–3420 (1996).

79.   N. Nishioka and Y. Domankevitz, "Reflectance During Pulsed Holmium Laser Irradiation," **381**, (1989).

80.   F. Chambettaz, F. Marquis, and R. P. Salathe, "Temperature dependence of reflectance and transmittance of the artery exposed to airduring laser irradiation," **40**, 105–107 (1993).

81.   J. K. Barton, "Dynamic Changes in Optical Properties," in *Optical-Thermal Response of Laser-Irradiated Tissue* (Springer Netherlands, 2010), pp. 321–349.

82.   P. H. Tomlins and R. K. Wang, "Theory, developments and applications of optical coherence tomography," J. Phys. D. Appl. Phys. **38**, 2519–2535 (2005).

83.   J. M. Schmitt, "Optical Coherence Tomography (OCT): a review," IEEE J. Sel. Top. Quantum Electron. **5**, 1205–1215 (1999).

84.   W. Drexler and J. G. Fujimoto, *Optical Coherence Tomography: Technology and Applications, Second Edition* (Springer International Publishing, 2015).

85.   A. Wetter, M. Faucher, and B. Sévigny, "High power cladding light strippers," in *Fiber Lasers V: Technology, Systems, and Applications* (SPIE, 2008), Vol. 6873, p. 687327.

86.   C. Chen, W. Shi, R. Reyes, and V. X. D. Yang, "Buffer-averaging super-continuum source based spectral domain optical coherence tomography for high speed imaging," Biomed. Opt. Express **9**, 6529 (2018).

87.   S. R. Chandra, "Intraocular Tumors: A Text and Atlas," Arch. Ophthalmol. **112**, 169 (1994).

88.   J. A. Shields, C. L. Shields, and P. De Potter, "Photocoagulation of retinoblastoma.," Int. Ophthalmol. Clin. **33**, 95–9 (1993).

89.   J. A. Burns, S. M. Zeitels, L. M. Akst, M. S. Broadhurst, R. E. Hillman, and R. Anderson, "532 nm Pulsed Potassium-Titanyl-Phosphate Laser Treatment of Laryngeal Papillomatosis under General Anesthesia," Laryngoscope **117**, 1500–1504 (2007).

90.   S. M. Zeitels, L. M. Akst, J. A. Burns, R. E. Hillman, M. S. Broadhurst, and R. R.

Anderson, "Office-Based 532-nm Pulsed KTP Laser Treatment of Glottal Papillomatosis and Dysplasia," Ann. Otol. Rhinol. Laryngol. **115**, 679–685 (2006).

91. S. M. Zeitels, L. M. Akst, J. A. Burns, R. E. Hillman, M. S. Broadhurst, and R. R. Anderson, "Pulsed Angiolytic Laser Treatment of Ectasias and Varices in Singers," Ann. Otol. Rhinol. Laryngol. **115**, 571–580 (2006).

92. J. A. Werner, A.-A. Dunne, B. J. Folz, R. Rochels, S. Bien, A. Ramaswamy, and B. M. Lippert, "Current concepts in the classification, diagnosis and treatment of hemangiomas and vascular malformations of the head and neck," Eur. Arch. Oto-Rhino-Laryngology **258**, 141–149 (2001).

93. J. A. Werner, B. M. Lippert, S. Gottschlich, B. J. Folz, B. Fleiner, S. Hoeft, and H. Rudert, "Ultrasound-guided interstitial Nd: YAG laser treatment of voluminous hemangiomas and vascular malformations in 92 patients.," Laryngoscope **108**, 463–70 (1998).

94. C. M. Cilip, S. B. Rosenbury, N. Giglio, T. C. Hutchens, G. R. Schweinsberger, D. Kerr, C. Latimer, W. H. Nau, and N. M. Fried, " Infrared laser thermal fusion of blood vessels: preliminary ex vivo tissue studies ," J. Biomed. Opt. **18**, 058001 (2013).

95. N. C. Giglio, T. C. Hutchens, W. C. Perkins, C. Latimer, A. Ward, W. H. Nau, and N. M. Fried, " Rapid sealing and cutting of porcine blood vessels, ex vivo , using a high-power, 1470-nm diode laser ," J. Biomed. Opt. **19**, 038002 (2014).

96. L. A. Hardy, T. C. Hutchens, E. R. Larson, D. A. Gonzalez, C.-H. Chang, W. H. Nau, and N. M. Fried, " Rapid sealing of porcine renal blood vessels, ex vivo , using a high power, 1470-nm laser, and laparoscopic prototype ," J. Biomed. Opt. **22**, 058002 (2017).

97. C. J. Rees, J. Allen, G. N. Postma, and P. C. Belafsky, "Effects of gold laser on the avian chorioallantoic membrane," Ann. Otol. Rhinol. Laryngol. **119**, 50–53 (2010).

98. M. S. Broadhurst, L. M. Akst, J. A. Burns, J. B. Kobler, J. T. Heaton, R. R. Anderson, and S. M. Zeitels, "Effects of 532 nm pulsed-KTP laser parameters on vessel ablation in the avian chorioallantoic membrane: Implications for vocal fold mucosa," Laryngoscope **117**, 220–225 (2007).

99.   C. M. Cilip, D. Kerr, C. A. Latimer, S. B. Rosenbury, N. C. Giglio, T. C. Hutchens, W. H. Nau, and N. M. Fried, "Infrared laser sealing of porcine vascular tissues using a 1,470 nm diode laser: Preliminary in vivo studies," Lasers Surg. Med. **49**, 366–371 (2017).

100.   J. A. Burns, J. B. Kobler, J. T. Heaton, R. R. Anderson, and S. M. Zeitels, "Predicting clinical efficacy of photoangiolytic and cutting/ablating lasers using the chick chorioallantoic membrane model: Implications for endoscopic voice surgery," Laryngoscope **118**, 1109–1124 (2008).

101.   A. Major, S. Kimel, S. Mee, T. E. Milner, D. J. Smithies, S. M. Srinivas, Z. Chen, and J. S. Nelson, "Microvascular photodynamic effects determined in vivo using Optical Doppler tomography," IEEE J. Sel. Top. Quantum Electron. **5**, 1168–1175 (1999).

102.   S. L. Bridgers, W. Haven, and L. Success, "Clinical correlates of doppler/ultrasound errors in the detection of internal carotid artery occlusion," Stroke **20**, 612–615 (1989).

103.   P. Nowak-Sliwinska, T. Segura, and M. L. Iruela-Arispe, "The chicken chorioallantoic membrane model in biology, medicine and bioengineering.," Angiogenesis **17**, 779–804 (2014).

104.   R. Akiyama, A. Matsuhisa, J. T. Pearson, and H. Tazawa, "Long-term measurement of heart rate in chicken eggs.," Comp. Biochem. Physiol. A. Mol. Integr. Physiol. **124**, 483–90 (1999).

105.   D. Ribatti, "The chick embryo chorioallantoic membrane (CAM). A multifaceted experimental model," Mech. Dev. **141**, 70–77 (2016).

106.   M. J. Gounis, G. J. Ughi, M. Marosfoi, D. K. Lopes, D. Fiorella, H. G. Bezerra, C. W. Liang, and A. S. Puri, "Intravascular Optical Coherence Tomography for Neurointerventional Surgery," Stroke **50**, 218–223 (2019).

107.   C. Song, B. Tang, P. A. Campbell, and A. Cuschieri, "Thermal spread and heat absorbance differences between open and laparoscopic surgeries during energized dissections by electrosurgical instruments.," Surg. Endosc. **23**, 2480–2487 (2009).

108.   T. Mikami, A. Takahashi, K. Hashi, S. Gasa, and K. Houkin, "Performance of bipolar forceps during coagulation and its dependence on the tip material: a quantitative

experimental assay," J. Neurosurg. **100**, 133–138 (2004).

109. A. Casotto, C. Castrioto, and P. Orvieto, "An advanced system for electrocoagulation in neurosurgery.," J. Neurosurg. Sci. **32**, 61–3 (1988).

110. Y. Arakawa and N. Hashimoto, "Application of the bipolar forceps with heat pipe technology (IsoCool^{TM}) in neurosurgery," Japanese J. Neurosurg. **14**, 698–705 (2005).

111. K. Sugita and R. Tsugane, "Bipolar coagulator with automatic thermocontrol," J. Neurosurg. **41**, 777–784 (2009).

112. B. Vällfors and B. Bergdahl, "Automatically controlled bipolar electrocoagulation - "COA-COMP,"" Neurosurg. Rev. **7**, 185–189 (1984).

113. B. Bergdahl and B. Vällfors, "Studies on coagulation and the development of an automatic computerized bipolar coagulator," J. Neurosurg. **75**, 148–151 (1991).

114. R. G. and M. M. Manuel Dujovny, Nadav Dujovny, "Bipolar Coagulation in Neurosurgery," Surg. Neurol. (1998).

115.   and P. J. Manuel Dujovny, Ran Vas, Carroll P. Osgood, Joseph C. Maroon, "Technical Note," J. Neurosurg. **43**, 502–505 (1975).

116. K. Sakatani, M. Ohtaki, S. Morimoto, and K. Hashi, "Isotonic mannitol and the prevention of local heat generation and tissue adherence to bipolar diathermy forceps tips during electrical coagulation," J. Neurosurg. **82**, 669–671 (1995).

117. A. Samii and M. Dujovny, "Kirwan® "non-stick" bipolar forceps," Surg. Neurol. **45**, 297–298 (1996).

118. N. Çeviker, S. Keskil, and K. Baykaner, "A new coated bipolar coagulator: Technical note," Acta Neurochir. (Wien). **140**, 619–620 (1998).

119. A. K. Vellimana, D. M. Sciubba, J. C. Noggle, and G. I. Jallo, "Current Technological Advances of Bipolar Coagulation," Oper. Neurosurg. **64**, ons11–ons19 (2009).

120. J. Siu, A. G. Hill, and A. D. MacCormick, "Systematic review of reusable versus disposable laparoscopic instruments: costs and safety," ANZ J. Surg. **87**, 28–33 (2017).

121. M. Mootoo, J. F Cummings, G. Paulin-Curlee, G. A Trees, S. Harris, J. W Clymer, and J. F Amaral, "A Novel Advanced Bipolar Tissue Sealer Provides Improved Hemostasis and Less Thermal Damage," Glob. Surg. **3**, 1–5 (2018).

122. S. C. Noctor, V. Martínez-Cerdeño, and A. R. Kriegstein, "Contribution of intermediate progenitor cells to cortical histogenesis," Arch. Neurol. **64**, 639–642 (2007).

123. N. J. Allen and B. A. Barres, "Neuroscience: Glia - more than just brain glue.," Nature **457**, 675–7 (2009).

124. A. Olmes, H. G. Franke, E. Bänsch, H. Lubatschowski, M. Raible, G. Dziuk, and W. Ertmer, "Modeling of infrared soft-tissue photoablation process," Appl. Phys. B Lasers Opt. **65**, 659–666 (1997).

125. M. R. Johnson, P. J. Codd, W. M. Hill, and T. Boettcher, "Ablation of porcine ligamentum flavum with Ho:YAG, q-switched Ho:YAG, and quadrupled Nd:YAG lasers," Lasers Surg. Med. **47**, 839–851 (2015).

126. S. J. Lee and H. J. Ha, "In vivo measurement of blood flow in a micro-scale stenosis model generated by laser photothermal blood coagulation," IET Syst. Biol. **7**, 50–55 (2013).

127. J. Eichler and O. Gonçalves, "A review of different lasers in endonasal surgery: Ar-, KTP-, dye-, diode-, Nd-, Ho- and CO2-laser," Med. Laser Appl. **17**, 190–200 (2002).

128. E. Belykh, K. Yagmurlu, N. L. Martirosyan, T. Lei, M. Izadyyazdanabadi, K. M. Malik, V. A. Byvaltsev, P. Nakaji, and M. C. Preul, "Laser application in neurosurgery.," Surg. Neurol. Int. **8**, 274 (2017).

129. J. T. Walsh, T. F. Deutsch, and J. T. Walsh, "Pulsed CO2 Laser Ablation of Tissue: Effect of Mechanical Properties," IEEE Trans. Biomed. Eng. **36**, 1195–1201 (1989).

130. A. Bharti, *Laser Welding* (1988), Vol. 1.

"If I have seen further than others, it is by standing on the shoulders of Giants"

-Sir Isaac Newton